

# ZPEC -The Zodiacal Dust Polarization Evaluation Code

MSc thesis

Etteke Roebroeks



# ZPEC

## The Zodiacal Dust Polarization Evaluation Code

by

Etteke Roebroeks

to obtain the degree of Master of Science  
at the Delft University of Technology,  
to be defended publicly on Friday April 8, 2016

Student number: 4024915  
Project duration: August 3, 2015 – April 8, 2015  
Thesis committee: Dr. D. M. Stam, TU Delft, supervisor  
Prof. Dr. ir. P. N. A. M. Visser TU Delft  
Dr. A. Menicucci TU Delft

An electronic version of this thesis is available at <http://repository.tudelft.nl/>.



*"Look deep into nature and then you will understand everything better"*  
-Albert Einstein

Front image retrieved from <http://insider.si.edu/wordpress/wp-content/uploads/2012/06/alien-earths.jpg>



# Acknowledgements

*Etteke Roebroeks  
Delft, March 2016*

So here I am, at the end of my educational career and presenting this thesis. My study at TuDelft felt like it was an ever accelerating rollercoaster going up and down. As a bachelor student I felt confidence after passing my exams within the nominal study duration, especially if my hard work was rewarded with a good grade. However it was during my master education that I learned how to really enjoy studying and I developed a passion for the complexity of space based systems and I got motivated by the idea that I was educated to contribute to the expansion of our space frontiers. I learned that an ambition and a personality cannot be expressed by the grades and dates in the OSIRIS grading system. Although I am very happy to present this thesis work, I am also a bit sad as it implies my student life comes to an end.

Nine months ago I knew nothing about dust in space. Still I consider myself as a newbie in this field of research but I enjoyed myself getting lost in papers about the subject. I gathered enough knowledge to build a code that is able to determine properties of light that is scattered by dust located in between planets. I wanted a creative thesis topic and although writing a code doesn't sound creative at all, I teased my brain with finding solutions for the problems I encountered. A major advantage of this thesis topic is the ability to visualize my work resulting in interesting images of dust disks. Even my fellow graduation students at the ninth floor said "Etteke, I have no idea whats on your screen but it looks pretty awesome".

I would like to express my gratitude to my direct thesis supervisor, Dr. D. M. Stam. She has helped me with this thesis and has been shaping the work in a very pleasant way. She supported and directed me when necessary while at the same time giving me freedom and responsibility. Thanks to this I could stay motivated for the full project duration and I experienced the past nine months as a very pleasant and exciting time.

Special thanks goes to my parents that have always been supportive to me and stimulated me to grow, in any direction. Especially now that I am envisioning life after graduation I realize how much you have shaped me. It is thanks to you that I enjoy the engineering things like programming and solving complex equations as much as my creative hobbies and being outside in nature.

I cherish my friends and our shared memories. Without them my life in Delft wouldn't have been so enjoyable. Thanks for your happiness, inspiration, endless energy, our crazy moments together and your support, especially during the last month. I'm certain that our graduations and different plans for the future will not imply the end of our friendship.



# Summary

## The importance of analyzing dust in planetary systems

The habitability of exoplanets is determined by their surface properties and atmospheres. Spectropolarimetry is a powerful tool to characterize these exoplanets and retrieve atmospheric and surface properties. The observed brightness of an exoplanet and its polarimetric signal as a function of these properties can be simulated using different numerical models. To validate these models the results need to be compared with observations. The best test-case for this validation is the Earth itself, as the atmospheric and surface properties are known and hence the signal can be computed to a high degree of accuracy. The Lunar Observatory for Unresolved Polarimetry of Earth (LOUPE) shall be taking measurements of the unresolved Earth. The sole pixel that contains the Earth signal shall be compared with computations.

When directly observing exoplanets, dust in planetary systems acts as a noise source and a source of confusion. The dust signal adds up to the planetary signal and in addition planets can be confused with dust clumps. For LOUPE, the dust in the solar system (zodiacal dust) only acts as a noise source. In order for LOUPE to be successful, this noise level needs to be estimated. In addition, for future exoplanet characterization missions it is important to determine whether a clump of dust (exozodiacal dust) can be distinguished from a planet. The aim of the performed thesis work was to develop a computational tool that enables both.

## Necessary inputs to analyze dust

The tool that is developed computes in what way starlight is scattered by dust particles. In order to do so, it is necessary to know the optical density of the dust cloud. Therefore two models are constructed of dust clouds. The first model contains the optical thickness of the zodiacal dust cloud, the dust cloud in the Solar System. This cloud has three main contributors: the smooth cloud, asteroidal dust bands and an Earth circumsolar dust band. The optical density models for these components are adopted from Kelsall et al., (1998) but slight adaptations were made to make the model suitable for the LOUPE mission. The second model contains the optical thickness of the dust cloud orbiting star  $\beta$  Pictoris. This star is of scientific interest as it can be observed well and it has an orbiting planet, the effects of the planet on the dust disk are often topic of study. The optical density model for the  $\beta$  Pic dust disk is derived from a NASA collisional model, that predicts at what locations dust has been generated (Nesvold & Kuchner, 2015). As a reference also a smooth fan model was used to the example of Millar-Blanchaer et al., (2015).

In addition to the optical thickness models it is necessary to know how light is directed by dust particles upon scattering. The properties of the photons change upon scattering, these need to be computed as well in order to determine the polarization properties of the scattered light. The aforementioned is expressed by scattering functions, that give the changing properties of light as a function of scattering angle. The scattering functions of dust are not completely known, therefore the scattering functions of small fosterite particles are used as a baseline. These functions are slightly adapted to match the maximum polarization degree of 21% at 500nm for a scattering angle of  $90^\circ$  (Levasseur-Regourd, 1998). As the functions of fosterite particles were not available for the full scattering angle regime, the forward scattering behavior of the particles is approximated using a Mie scattering code.

## The Zodiacal Dust Polarization Evaluation Code

The computational tool that is presented in this thesis is called the Zodiacal Dust Polarization Evaluation Code, or in short ZPEC. It has been built up from scratch during the thesis project. Throughout its development major improvements were made considering computation time and efficiency, for which creative solutions had to be found in order to work with huge amounts of data. ZPEC is based on Monte-Carlo and follows the paths of the individual photons. Therefore it allows to analyze multiple scattering events, whereas classically it is assumed that dust disks are optically thin enough to neglect

these events. In a multiple scattering case, ZPEC takes the full polarized state of the photon into account to determine the scattering direction, which is often found neglected in other research.

The Adding-Doubling code (de Haan et al., 1987) is used to verify ZPEC. It is found that for large scattering angles the amount of scattered photons decreases, which causes a difference with the results of the Adding-Doubling Code. At smaller angles a maximum deviation of 0.19% in computed linear polarization degree was found (this is an absolute difference). This seems a large deviation, but it was shown that a difference of 0.21% can be expected due to binning of the photon properties to obtain an average. At larger angles the observed difference was at maximum 0.55%. This difference is caused by the fact that ZPEC is based on Monte-Carlo (MC), as in these regions few photons were found scattered. The error of the datapoints is on the same order of magnitude as the found difference. Therefore it can be concluded that the found differences are an effect of the MC simulation and data averaging across bins.

### Using ZPEC to analyze zodiacal and exozodiacal dust

ZPEC is used to analyze the view of the zodiacal cloud as observed from the Moon. In the detector views the Earth is included using a very simple planetary model (black reflecting surface and a thick homogeneous atmosphere that only contains gas molecules). Analysis of the observed brightness shows that the brightness of the background dust with respect to the brightness of the Earth is between  $4 \cdot 10^{-4} - 0.14\%$ , hence the Earth can be resolved very well from the background dust using the detected brightness. When the polarization degree of the dust and Earth are compared however, the Earth is not always distinguishable. For 17 of the 120 simulated days the polarization signal of the Earth was (about) the same as the background dust.

The relatively optically thick dust disk orbiting star  $\beta$  Pictoris provides an interesting case to check whether dust disks are indeed optically thin enough to neglect multiple scattering. This was analyzed using both the SMACK derived optical density model and a smooth fan model. The use of both models has shown that multiple scattering increases the maximum polarization degree that is observed, the effect increases towards the edges of the dust disk. Using SMACK, ZPEC predicts the absolute effect (increase in polarization degree) is up to 1.8%, using the smooth fan model the effect was predicted to increase up to 0.78%. The  $1\sigma$  uncertainty in these numbers is 0.07%, which is caused by the variation of the datapoints around the average (as a result of the code being based on Monte-Carlo).

ZPEC was also used to analyze whether such a trend is visible when the polarization state of the photon is not taken into account in order to compute the scattering direction, compared to a case where it is taken in account. The difference found is on the same order of magnitude as the uncertainty in this difference, thus it must be concluded that the effect is not large enough to be detected by ZPEC.

A hypothetical planetary polarization signal is included in the detector views of the  $\beta$  Pictoris dust disk, which is compared with the background polarization signal of the zodiacal dust. The polarization signal of the planet differs significantly from the local polarization degree of the surrounding dust and hence it is expected a planet can be well distinguished when observed over longer periods of time. However as the maximum polarization degree of the planet is incidentally equal to the maximum polarization degree of one of the pixels in the detector, it shall be hard to distinguish the planet if it is studied only at one time instance.

In order to find out if a planet can be distinguished from a dust clump, ZPEC was used to analyze the effect of a high optical density region in the  $\beta$  Pictoris dust cloud. To do this, the optical thickness was artificially raised at a location in the smooth dust disk. The dust clump created a shadow effect under certain viewing angles, a phenomenon that was not observed for the planet as the planetary signal was included *after* the photon database was generated. Although the simulated dust clump was relatively large compared to the dust cloud it did not lead to a higher/lower polarization signal at the expected location of the clump in the detector views. It is therefore concluded that a dust clump shows the same polarization behavior as a function of scattering angle as the surrounding dust.

As a planet could be distinguished from its smooth surroundings based on the observed linear polarization degree as a function of wavelength and the dust clump couldn't, it is concluded that a clump can be distinguished from a planet based on this difference in behavior. However as the simulated dust clumps were relatively large it is recommended to simulate the effect of smaller dust clumps as these better represent the cases in which scientists confuse a clump with a planet.

# Contents

<b>1</b>	<b>Introduction</b>	<b>1</b>
1.1	LOUPE as a benchmark for future exoplanet characterization missions	1
1.2	Dust as a noise source and source of confusion	2
1.3	Analyzing light scattered by zodiacal dust.	2
1.4	ZODIPIC	3
1.5	Monte-Carlo as a modelling technique for dust structures	4
1.6	Research objective and tasks	4
1.7	Contents and structure	5
<b>2</b>	<b>Modelling dust clouds</b>	<b>7</b>
2.1	Solar System dust cloud model	7
2.1.1	Optical thickness model of the COBE/DIRBE mission	8
2.1.2	Transformation of the optical thickness model to VIS domain	12
2.1.3	Adapting the model for the Earth circumsolar ring	13
2.2	Model of $\beta$ Pictoris' dust disk	15
2.2.1	SMACK collisional model	15
2.2.2	Transformation of SMACK model into an optical thickness model	16
<b>3</b>	<b>Single scattering by zodiacal dust particles</b>	<b>21</b>
3.1	Introduction to single light scattering	21
3.1.1	Polarization degree of light.	21
3.1.2	Describing scattering behavior using scattering functions	23
3.1.3	Scattering regimes	24
3.2	Properties of dust particles in the Solar System	25
3.2.1	The shape, structure and material of IDPs	25
3.2.2	Typical flux and polarization features	26
3.2.3	Reconstruction of the zodiacal dust scattering functions	27
3.2.4	Reconstruction of $\beta$ Pictoris dust scattering functions	29
<b>4</b>	<b>Multiple scattering: the zodiacal dust polarization evaluation code</b>	<b>31</b>
4.1	ZPEC main simulator structure	31
4.2	ZPEC algorithm.	32
4.2.1	Initialization	33
4.2.2	Group Selection	34
4.2.3	Launch of photon entry coordinates	35
4.2.4	Scattering of the photon	36
4.2.5	Moving the photon	38
4.2.6	Living photons	40
4.2.7	Outputs: database	40
4.3	Verification using the Adding-Doubling code	41
4.3.1	Reference case	41
4.3.2	Results and Discussion	42
4.3.3	Quantification of the Monte-Carlo effect.	44
4.3.4	Testing with other albedo	47
4.3.5	Testing with other phase functions	47
4.3.6	The effect of taking the polarization state into account	48
<b>5</b>	<b>Results</b>	<b>51</b>
5.1	Results for the dust disk in the Solar System	51
5.1.1	Creating an Internal observer view	52
5.1.2	Including Earth in the internal observer view	53

5.1.3	LOUPE view without the Earth simulated . . . . .	55
5.1.4	LOUPE view with Earth simulated . . . . .	58
5.1.5	Comparison with and without Earth trailing high density region . . . . .	60
5.1.6	Skyplots of the zodiacal dust intensity and brightness . . . . .	61
5.2	Results for the dust disk surrounding $\beta$ Pictoris. . . . .	64
5.2.1	Creating an external observer view . . . . .	64
5.2.2	Including a planet for an external observer . . . . .	66
5.2.3	Image using SMACK density model . . . . .	67
5.2.4	The importance of multiple scattering in the $\beta$ Pictoris dust disk. . . . .	68
5.2.5	Effect of taking polarization into account to determine scattering direction . . . . .	72
5.2.6	Distinguishing a planet from a dust clump. . . . .	75
<b>6</b>	<b>Conclusion and Recommendations</b>	<b>83</b>
6.1	Conclusion . . . . .	83
6.2	Recommendations for future work. . . . .	85
	<b>Appendices</b>	<b>87</b>
<b>A</b>	<b>Calculation of rotation angle <math>\beta</math></b>	<b>89</b>
<b>B</b>	<b>Moving the photon: governing equations</b>	<b>91</b>
B.1	Spherical to Cartesian coordinates . . . . .	91
B.2	Cartesian to Spherical coordinates . . . . .	91
B.3	Single scattering - scattering location coordinates . . . . .	91
B.4	Grid cell boundary- leaving planes. . . . .	91
<b>C</b>	<b>Including planetary signals</b>	<b>93</b>
C.1	Figures . . . . .	93
C.2	Equations . . . . .	93
C.3	Orbital properties . . . . .	94
<b>D</b>	<b>Loupe views of Earth and background dust</b>	<b>95</b>

# List of Abbreviations

3D	threedimensional
AD	Adding-Doubling
AU	Astronomical Unit
BOE	Brightness Opposition Effect
COBE	Cosmic Background Explorer
DIRBE	Diffuse Infrared Background Experiment
IDP	Interplanetary Dust Particle
IR	Infrared
LOUPE	Lunar Observatory for Unresolved Polarimetry of Earth
NPB	Negative Polarization Branch
PCA	Particle Cluster Aggregation
Pic	Pictoris
POE	Polarization Opposition Effect
SMACK	Superparticle-Method Algorithm for Collisions in Kuiper belts
VIS	Visual
ZPEC	Zodiacal Dust Polarisation Evaluation Cde



# List of Symbols

Symbol	Description	Unit
$a$	azimuth (in photon reference frame), direction of movement of photon	[rad]
$a$	amplitude of magnetic field vector $\mathbf{E}$	-
$az$	azimuth (heliocentric)	[rad]
$A$	Surface area	[AU <sup>2</sup> ]
$e$	elevation (in photon reference frame), direction of movement of photon	[rad]
$el$	elevation (heliocentric)	[rad]
$F$	Flux	photons
$F$	scattering matrix	-
$F_{\dots}$	scattering functions, often indicated by $F_{xx}(\theta)$	photons
$g$	modelling parameter for the smooth zodiacal cloud	-
$H$	hemisphere function	-
$i$	index	-
$i$	imaginary number, $i = \sqrt{-1}$	-
$i$	inclination	[rad]
$I$	total light beam intensity	photons
$k$	light wave number	-
$L$	Stokes vector rotation matrix	-
$n$	optical density as indicated by (Kelsall et al., 1998)	[AU <sup>-1</sup> ]
$N_{u,e}$	number of undisturbed photons entering a grid cell	-
$N_{u,t}$	number of undisturbed photons transmitted through a grid cell	-
$p$	randomly drawn number between 0-1 with uniform distribution	-
$p_{\dots}$	shape parameter, asteroidal dust bands	-
$P$	probability	-
$P$	degree of polarization	[%]
$P_{rand}$	randomly drawn number between 0-1 with uniform distribution	-
$Q$	linearly polarized intensity, $I(0^\circ) - I(90^\circ)$	photons
$R$	particle radius	[m]
$R$	Heliocentric radius	AU
$R_C$	heliocentric distance to the center of the smooth zodiacal cloud	[AU]
$t$	time	[s]
$U$	linearly polarized intensity $I(45^\circ) - I(135^\circ)$	photons
$v$	shape parameter, asteroidal dust bands	-
$V$	circularly polarized intensity	photons
$x$	dimensionless particle size	-
$x$	x-coordinate	-
$X$	heliocentric x-coordinate	[AU]
$y$	y-coordinate	-
$Y$	heliocentric y-coordinate	[AU]
$z$	z-coordinate	-
$Z$	heliocentric z-coordinate	[AU]

---

<b>E</b>	Electric field vector of light wave
<b>I</b>	flux or Stokes vector
<b>l</b>	unit vector perpendicular to light propagation direction $\mathbf{z}$
<b>r</b>	unit vector perpendicular to light propagation directions <b>l</b> and $\mathbf{z}$ , completing the right handed system
<b>z</b>	direction of propagation of light waves

Symbol	Description	Unit
$\alpha$	radial power law exponent, modelling parameter smooth zodiacal cloud	-
$\beta$	vertical shape parameter, modelling parameter smooth zodiacal cloud	-
$\beta$	rotation angle from scattering plane to local meridian through second scattering direction	[rad]
$\delta_{\zeta}$	shape parameter, asteroidal dust bands	[rad]
$\delta_R$	radial cut-off	[AU]
$\Delta x$	layer thickness	
$\Delta x$	photon path length	
$\Delta X_S$	undisturbed photon path from scattering location to grid cell exit location	
$\epsilon$	delay factor of $\mathbf{E}$	[rad]
$\epsilon_l$	phase of $E_r$	[rad]
$\epsilon_r$	phase of $E_l$	[rad]
$\gamma$	vertical power law exponent, modelling parameter for smooth zodiacal cloud	-
$\gamma$	rotation angle from local meridian through initial scattering direction to scattering plane	[rad]
$\lambda$	wavelength of light	[m]
$\mu$	widening parameter, modelling parameter smooth zodiacal cloud	-
$\omega$	circular frequency of light waves	[rad]
$\Omega$	right ascension of ascending node	[rad]
$\Phi$	Flux	photons
$\psi$	angle of $\mathbf{E}$ with respect to $\mathbf{I}$	[rad]
$\Psi$	azimuthal angle	[rad]
$\sigma$	dispersion coefficient	[AU]
$\tau$	optical thickness	[AU <sup>-1</sup> ]
$\theta$	scattering angle	[rad]
$\theta$	longitude	[rad]
$\zeta$	modelling parameter for the smooth zodiacal cloud	-

Subscript	Description
0	initial
$\theta$	longitude
B1-B3	dust bands 1-3
cp	circular polarization
C	to the center of the smooth zodiacal cloud
D	undisturbed
ext	external
lp	linear polarization
$\mathbf{I}$	in the direction of vector $\mathbf{I}$
LB	Leading blob
NB	negative density region (or blob)
pol	polarized
r	radial
$\mathbf{r}$	in the direction of vector $\mathbf{r}$
s,S	scattering
SR	solar ring
TB	trailing blob
unpol	unpolarized
z	in vertical or z-direction

# Introduction

In the search for extraterrestrial life exoplanets play a keyrole. The properties of their atmospheres and surfaces reveal if life can arise and survive and therefore their characterization is of importance. This can be done using polarimetry, which increases the contrast between the planet and the hosting star hence making the planet directly detectable. When polarimetry is used to study exoplanets, the dust in these exoplanetary systems acts as a source of confusion when the polarimetric signal of a dust clump is confused with a planetary signal. The study to dust in planetary systems is subject of this thesis.

## 1.1. LOUPE as a benchmark for future exoplanet characterization missions

The habitability of a planet is determined by its atmospheric properties and surface features. For example it is believed that the presence of liquid water is a strong indicator that life could arise and an atmosphere is believed to be necessary to protect early life-forms from harmful stellar radiation. It means that solely the detection of exoplanets is not enough in the search for extraterrestrial life: characterization of the exoplanet is necessary in order to determine the properties of its surface and atmosphere. Transit spectroscopy and Doppler spectroscopy can be used to study atmospheres of gaseous planets that are in tight orbits around their star. These planets are large and massive enough to influence the radial velocity of the star and cause a significant decrease in measured star luminosity if in transit. Unfortunately rocky exoplanets are harder to characterize with indirect methods and hence direct observations are believed to be more promising (Karaldi et al., 2012).

Polarimetry is a measurement technique whereby the vibrational direction of light can be determined. Starlight is generally unpolarized which means that the light waves vibrates in a random direction. Scattering by atmospheric particles or reflection by a surface changes the preferred direction of vibration and light becomes polarized which can be measured and modelled using scattering theory. Therefore such measurements of exoplanets can be used to gain knowledge about the composition of their atmosphere and surface. Furthermore polarimetry is convenient to use for exoplanet detection, as it allows to distinguish between the very bright unpolarized starlight and the faint and usually polarized light from a planet. It was reported by (Keller et al., 2010) that polarimetry typically increases the contrast between star and planet with about 3-5 orders of magnitude. Polarimetry directly shows the nature of the planet by the degree of polarization and the polarization direction, as these quantities are very sensitive to the composition and structure of the atmosphere and surface (Seager et al., 2000; Stam, 2008). An example is the determination of the size and composition of the droplets in Venus' upper cloud decks by using Earth-based polarimetry (Hansen & Hovenier, 1974). In addition Stam et al., (2006) and Karalidi, Stam & Hovenier (2012) show that polarimetry can be used to identify the existence of liquid water clouds on exoplanets.

When exoplanets are observed directly, they are spatially unresolved i.e. appear as a single pixel or a fraction thereof. This sole pixel contains valuable information about the atmosphere, clouds and surface of the planet. There are several numerical models available that simulate exoplanet signals and using these models the characteristics of the exoplanet can be derived. The best case to test these models is the Earth itself, as the atmospheric composition of the Earth is known as well as surface and cloud properties. Therefore data from observations of the Earth as an exoplanet enable us to check numerical models and retrieval algorithms (Karaldi et al., 2012).

An instrument called LOUPE (Lunar Observatory for Unresolved Polarimetry of Earth) is a spectropolarimeter currently under development which shall observe the Earth as an exoplanet (Karaldi et al., 2012). It is being designed to function as a standalone instrument to be located in a piggyback configuration on a lunar lander. It shall make unresolved observations of the flux and polarization of the Earth in the visual spectrum, covering all diurnal rotations, seasons and phase angles. Through comparison of the models and observations, the models can be calibrated for their purpose of exoplanet characterization. It is therefore expected that LOUPE will prove that spectropolarimetry is a successful and valuable method for exoplanet characterization.

## 1.2. Dust as a noise source and source of confusion

Large planetary bodies like exoplanets are not the only bodies orbiting stars: also smaller debris and dust is present. Dust is located everywhere in planetary systems: it can be found in disk-like shapes closer to stars, it forms shells in outer regions of planetary systems and it is found in clumps in between the planets. Dust that is located in between the planets is generally referred to as (exo)zodiacal dust or the (exo)zodiacal cloud. The term *zodiacal dust* refers to dust in between the planets in the Solar System, while *exozodiacal dust* is found in exosystems: planetary systems other than our own.

In the Solar System there are three families of dust that make up the majority of the zodiacal cloud: a smooth disk, the asteroidal dust bands and the Earth circumsolar ring which co-rotates with the Earth in its orbit around the Sun (Kelsall et al., 1998). In addition, a small fraction of the dust mass is of cometary origin and can be observed as debris trails. This dust together is referred to as zodiacal dust. As the Earth moves along its orbit it travels through the zodiacal cloud, as seen from the Moon the amount of dust in between the Earth and Moon and the dust in the background is ever-changing. This dust potentially contributes to the polarization signal that LOUPE will observe if the amount of dust is large enough. As LOUPE observes the Earth, it will inevitably also observe the signal of the dust. Therefore dust is a potential noise source for the LOUPE mission and the topic of analysis of this thesis work.

Dust does not only act as a noise source, but in the case of exoplanets exozodiacal dust (dust in exosystems) acts as a source of confusion as well. Thick dust disks in younger planetary systems can form clumps or structures that look like clumps under certain viewing angles and can be confused with a planetary signal, causing false exoplanet detection. Therefore background flux of dust in planetary systems is thought to be one of the largest sources of astrophysical noise in direct observations of terrestrial planets in habitable zones. For spectropolarimetry to be a successful method it is necessary to determine if a dust clump can be distinguished from an exoplanet.

One of the extrasolar dust disks that is often studied is the dust disk surrounding young star  $\beta$  Pictoris. The dust disk is relatively thick and shows resonant features as a result of orbiting planet  $\beta$  Pic b and maybe other yet undiscovered planets.

## 1.3. Analyzing light scattered by zodiacal dust

At this moment it may be clear to the reader that dust is topic of this MSc thesis and specifically how light is scattered by zodiacal dust. Before further discussing the research topic and objective it is of interest to know what dust properties affect light scattering by zodiacal dust particles and what are the related phenomena.

The first property of interest is the density or the thickness of the studied dust structure. In relation to light studies this density is expressed as the optical thickness, which is a measure for the average distance travelled by the individual photon before it encounters a dust particle. Within a dust structure the optical

thickness may vary. In planetary systems the optical thickness is usually higher at distances closer to the central star and lower at the edges of the structure. The structure itself is usually a disk with some higher and lower density regions as an effect of planetary and cometary interaction. Exozodiacal dust disks can theoretically be observed at all inclinations with respect to the line of sight: from an edge-on configuration to a face-on configuration. Now the question whether an individual photon encounters a dust particle becomes a matter of statistics for which the condition holds that the average path traversed equals the optical thickness of the cloud.

Secondly the dust particles themselves are of interest and more specifically the interaction between the dust particles and the photons, which determines how the photons are scattered by the dust particles. This relation is not easily summarized in one property, as there are multiple properties influencing light scattering. Such properties are the size of the dust particle, the porosity, the structure and its material. These properties influence the state of the photon upon an encounter: in what direction the photon is propagated and the vibrational state of the photon. How exactly these properties influence the state of the photon is not a topic for this thesis, but the change of photon state upon scattering is necessary input. The change of the photon state upon encounter can be empirically derived using measurements of light being scattered by dust samples. Sometimes it is also possible to approximate the change of properties using a computational algorithm. As zodiacal dust particles are complex such approximations do not very well predict the actual properties and it is preferred to use empirical relationships. It is however hard to do measurements on actual dust samples and from this, make a conclusion about the complete cloud. Dust sample return missions have taken place in the past, but it is uncertain whether the found dust particles represent the whole cloud structure, as they were taken only from distances close to Earth. Empirical relationships can be established for dust samples taken on Earth that are believed to be similar to zodiacal dust particles. However as the properties of zodiacal dust are unknown this remains a topic of study. Hence the change of particle properties upon scattering, expressed by a set of equations and graphs, is uncertain. This uncertainty shall be addressed when appropriate.

Light scattering theory is based on analysis of a complete beam of light consisting of multiple photons. It is often assumed that the individual photons in this beam of light are scattered only once. It means that photons leaving the central star have encountered a dust particle only once before the photons are detected. This assumption is valid when the optical thickness is low and the chances of the photons hitting another dust particle negligible. The properties of light that is singly scattered are often indicated by 'first order'. It is however also possible that photons are scattered multiple times before they are detected and hence they have met multiple dust particles along their travelled path, this is indicated by 'total order'. In this case the properties of the photon have changed multiple times. Whether a photon is scattered multiple times depends on statistics.

## 1.4. ZODIPIC

Milan-Gabet et al., (2011) describes the use of ZODIPIC <sup>1</sup> to model the brightness of exozodiacal clouds, which is the only publicly available code that allows to study the shapes and densities of (exo)zodiacal clouds. This model is based on the dust disk model of Kelsall et al., (1998) that was constructed using COBE/DIRBE measurements in the infrared spectrum. The basic model that ZODIPIC uses is a Solar System zodiacal twin disk (only the smooth component of the cloud is modelled) with the same radial density profile as in the Solar System, with the same optical depth as the zodiacal cloud at 1AU. The radial temperature profile within the disk is scaled with stellar luminosity.

A critical note has to be placed when it comes to the use of ZODIPIC to study exozodiacal dust as a function of time. Our current understanding of dust is based on the zodiacal dust in our own Solar System, in which evolutionary processes take place on a timescale that is relatively short with respect to the lifetime of the Solar System. It is therefore hard to predict the evolution of the disk over longer periods of time. Other planetary systems that might harbor exoplanets might be in a different stage of their lifetime compared to our own Solar System. It is therefore that the inability to predict long-term behavior of zodiacal dust complicates the study to exozodiacal dust (Levasseur-Regourd, 1998;

---

<sup>1</sup>No papers are available about ZODIPIC, but the computational package is provided via the website of Marc Kuchner, see <http://asd.gsfc.nasa.gov/Marc.Kuchner/home.html>

Roberge et al., 2012). However, as the LOUPE mission is short in comparison to the lifetime of the Solar System, this should not be a problem to study zodiacal dust.

Another potential disadvantage of the use of ZODIPIC is the assumption that the zodiacal cloud is optically thin, hence multiple scattering is neglected. Although this assumption is valid for dust in the Solar System and most other systems, the effect is not studied for clouds that are optically thicker or for clouds in which dust clumps are present. Furthermore ZODIPIC computes the signal of a dust disk as measured by a distant observer, but in the case of LOUPE one would like to analyze the dust at a location inside the disk. In addition ZODIPIC does not allow polarization calculations, therefore its use would be disadvantageous for this thesis work.

## 1.5. Monte-Carlo as a modelling technique for dust structures

It is clear that the shortcomings of ZODIPIC have to be overcome and that a model of (exo)zodiacal clouds should comprise at least the following:

- It should be able to compute spectropolarimetric properties of dust clouds.
- It should be able to use different shape models of zodiacal clouds, with their own typical structure and optical thickness.
- It should be able to analyze photons that have been scattered multiple times by dust particles

It is possible to evaluate the dust disk using a combination of existing codes and evaluation packages, however it was found that this would bring along great challenges. The use of an Adding-Doubling code for example (de Haan et al., 1987), is limited to dust layers that are infinite in two dimensions and have finite thickness. A dust layer with varying optical thickness can be approximated using the results for multiple layers, but for the zodiacal cloud such a solution would be complex and potentially leads to large errors at the edges.

Instead it is thought that a Monte-Carlo approach to simulate dust properties is a better approach, if the paths of enough photons are tracked to generate a statistical average. Ramella-Roman, Prahel & Jacques (2005) describe the necessary basics of a code that can analyze light transportation through a scattering medium. A computational code based on Monte-Carlo fulfills all the above stated requirements.

## 1.6. Research objective and tasks

For the LOUPE mission it is important to know how zodiacal dust between the Earth and Moon as well as the background dust influences the measured polarization signal of the unresolved Earth. For future exoplanet characterization missions it is not only important to know how dust acts as a noise source, but also how signals of planets and dust can be distinguished. The only available code that allows to study (exo)zodiacal dust disks is ZODIPIC, but this code does not allow to analyze the polarization signal of the dust and does not allow the observer to be located inside the disk. Therefore, the analysis of the polarization signal of (exo)zodiacal dust is topic of this thesis and the research objective that is to be met by means of this thesis is defined as follows:

*To develop a computational tool based on Monte-Carlo statistics that can be used to analyze polarization properties of (exo)zodiacal dust disks.*

From this research objective a set of tasks was derived;

1. Develop the computational tool in MATLAB.
2. Verify the code works correctly with the Adding-Doubling code
3. Use the tool to predict the background signal as sensed by LOUPE
4. Use the tool to analyze whether a dust clump can be distinguished from a planet using the planetary system  $\beta$  Pictoris as a reference case.

This report shows in what way the research tasks were performed and gives the results of the research.

## 1.7. Contents and structure

Chapter 2 of this report is dedicated to the dust clouds that are of interest for this thesis. The reader shall be introduced to the shape of the dust cloud in the Solar System and the dust cloud in the planetary system of star  $\beta$  Pictoris. For both disks an optical density model is derived that shall be used later on to compute how photons are scattered within these disks.

Chapter 3 gives an overview of single scattering by zodiacal dust particles. First the reader shall be familiarized with the necessary background information on single scattering theory. After this an overview is given of our current knowledge of the properties of zodiacal dust particles.

Multiple scattering is discussed in Chapter 4, that is dedicated to the code that has been developed to analyze scattering in dust disks. The simulator structure is discussed in detail, followed by a section dedicated completely to the verification of the code.

In Chapter 5 the results of the analyses on the dust disks in the Solar System and in the system of  $\beta$  Pictoris are given. This thesis work ends with a conclusion and recommendations, presented in Chapter 6.



# 2

## Modelling dust clouds

As was already discussed in Section 1.3, the optical thickness of the zodiacal cloud is of importance when the light scattered by this dust is to be analyzed. Two dust clouds are to be analyzed: both the cloud in the Solar System (referred to in research task 3) and the cloud in the planetary system of  $\beta$  Pictoris (referred to in research task 4). Optical thickness models were hence constructed for the two target dust clouds, which shall be discussed in this chapter. First it shall be discussed how the optical thickness model was constructed for the Solar System. An existing model was used but needed adaptation for the purpose of LOUPE. Then it shall be discussed how the optical thickness model was constructed for the dust disk surrounding  $\beta$  Pictoris, which was derived from a NASA collisional model.

In this thesis work the optical thickness or density is understood as the average path of a photon until it is scattered. Using the example of (Kelsall et al., 1998) the optical thickness is given per AU, hence the unit of the optical thickness is  $[AU^{-1}]$ . Through the use of this unit one should be careful not to confuse the term 'optical thickness' with 'opacity' or 'extinction'.

### 2.1. Solar System dust cloud model

As was mentioned in Section 1.2, the dust cloud in the Solar System has three main components: the largest component is a smooth cloud extending from the Sun to the outer Solar System, smaller are the Earth's circumsolar ring and the asteroidal bands. None of the models found in literature describes these components perfectly. Classically the smooth cloud is described by a fan model in which the spatial dust density is given as a function of Solar distance and ecliptic latitude (Hahn et al., 2002). The classical fan model is widely used and provides a fit of better than 10% in observed brightness at low latitudes (Leinert et al., 1980; Giese & Kneissel, 1989). At high latitudes however, this model overestimates the dust brightness with 31%. To fit the dust cloud better at these latitudes a modified fan model can be used as proposed by Lumme & Bowell (1985) and several cosine models by Giese, Kneissel & Rittich (1986). There are also different models available for the asteroidal bands (Reach, Franz & Weiland, 1997).

The optical thickness model that is used in this work is a result of the COBE (Cosmic Background Explorer) DIRBE (Diffuse Infrared Experiment) mission that aimed to measure the cosmic background radiation (e.g. Weiland et al, 1994). To retrieve the background signal from the measurements, the contribution of the dust had to be subtracted. Therefore a zodiacal dust model had to be constructed and it is based on a widened fan model. The model is described in more detail in the coming section.

### 2.1.1. Optical thickness model of the COBE/DIRBE mission

The COBE optical thickness model is based on fitting of all-sky infrared observations ( $1.25 - 240\mu m$ ) of DIRBE with a parameterized physical model (Kelsall et al., 1998). It includes the smooth cloud, three asteroidal bands and the Earth's circumsolar ring. The optical thickness of the cloud is described as a function of heliocentric ecliptic coordinates  $(X, Y, Z)$ . The optical thickness model is therefore a model of the optical thickness of the zodiacal dust cloud with the Sun at the center. All the equations and parameters presented in this section are retrieved from Kelsall et al., (1998).

#### The smooth cloud

The smooth cloud is allowed to have an offset  $(X_0, Y_0, Z_0)$  with respect to the heliocentric center. The coordinates used to calculate the optical thickness of the smooth cloud are described as follows in which  $R_c$  is the distance to the center of the cloud;

$$\begin{aligned} X' &= X - X_0 \\ Y' &= Y - Y_0 \\ Z' &= Z - Z_0 \\ R_c &= \sqrt{X'^2 + Y'^2 + Z'^2} \end{aligned} \quad (2.1)$$

As the cloud is slightly tilted with respect to the heliocentric equator, the height above the tilted midplane is calculated using the inclination  $i$  of the cloud and the ascending node  $\Omega$ ;

$$Z_c = X' \sin \Omega \sin i - Y' \cos \Omega \sin i Z' + \cos i \quad (2.2)$$

As for the classical fan models, it is assumed that the density function can be separated in a radial and vertical term. The vertical term  $f(\zeta)$  is expressed as follows;

$$f(\zeta) = e^{(-\beta g \gamma)} \quad (2.3)$$

$$g = \begin{cases} \zeta/2\mu & \text{for } \zeta < \mu \\ \zeta - \mu/2 & \text{for } \zeta \geq \mu \end{cases}$$

In this equation  $\beta$ ,  $\gamma$  and  $\mu$  are shaping parameters and  $\zeta = |Z_c/R_c|$ . Now the optical thickness of the cloud as a function of the heliocentric coordinates can be calculated as;

$$n_c(X, Y, Z) = n_0 R_c^{-\alpha} f(\zeta) \quad (2.4)$$

The values for the parameters used in Eq. 2.1-2.4 are given in Table 2.1.

Table 2.1: Smooth cloud parameters (Kelsall et al., 1998)

cloud component	parameter	Description	COBE fitted mean value
Smooth Cloud (Widened fan model)	$n_0$	density at 1AU	$1.13 \times 10^{-7} \text{ AU}^{-1}$
	$\alpha$	radial power law exponent	1.34
	$\beta$	vertical shape parameter	4.14
	$\gamma$	vertical power law exponent	0.942
	$\mu$	widening parameter	0.189
	$i$	disk inclination	$2.03^\circ$
	$\Omega$	ascending node	$77^\circ$
	$X_0$	x offset from Sun	0.0119 AU
	$Y_0$	y offset from Sun	0.00548 AU
	$Z_0$	z offset from Sun	-0.00215 AU

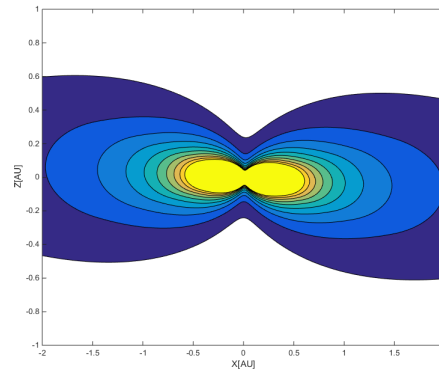


Figure 2.1: Isodensity contours of the smooth cloud contribution in the helioecliptic cross-sectional plane XZ . The contours are shown at densities of  $[0.2, 0.4, 0.6, 0.8, 1.0, 1.2, 1.4, 1.6, 1.8, 2.0]n_0$  with  $n_0$  the density at 1AU.

### Asteroidal dust bands

The asteroidal dust bands were discovered using the IRAS satellite after removal of the brightness contribution of the smooth cloud (Dermott et al., 1984; Sykes & Greenberg, 1986). Dust particles and debris are being generated by mutual collisions of asteroids. Depending on the size of the particles/debris the orbits of the particles evolve differently. Right after the creation, the particles are all in the same orbit with the same orbital velocity, in an orbit with the same inclination as their asteroid family. Right after their formation, the dust particles start to spiral towards the Sun (while very small particles are being rejected out of the Solar System). There is a reasonable chance that the particles collide with other particles, which causes a latitudinal spread that increases with decreasing distance to the Sun starting at about 2AU. Depending on the velocity of the particles that collide they are either shattered or they accrete. Some particles/aggregates continue their journey towards the Sun, others impact planets or moons. It is estimated that the lifetime of an asteroidal particle that is eventually burned by the Sun is  $10^5 - 10^6$  years. (e.g Fixsen & Dwerk 2002; Dermott et al., 1994)

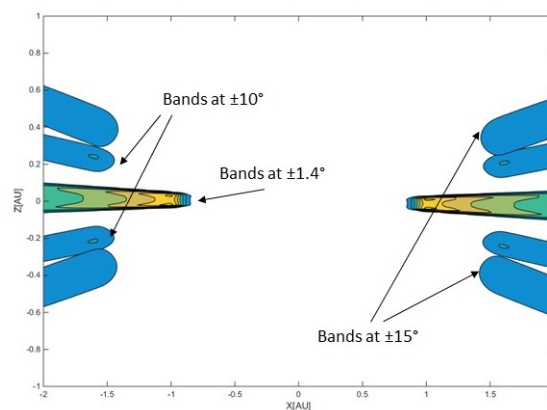


Figure 2.2: Isodensity contours of the asteroidal dust bands in the helioecliptic cross-sectional plane XZ.  $[0.2, 0.4, 0.6, 0.8, 1.0, 1.2, 1.4, 1.6, 1.8, 2.0]n_{band}$  with  $n_{band}$  the band density at 3AU. For clarity the asteroidal band pairs are indicated in the figure using their inclination. The band pair at  $1.4^\circ$  is virtually not a pair as the bands are so close to each other.

It is calculated by Dermott et al., (1994) that Jovian resonance causes asteroidal dust to longitudinally spread and form asteroidal belts on a timescale of  $10^6 - 10^7$  years. Dust smaller than 100 microns spirals into the Sun before Jovian perturbations can precess its orbit sufficiently to form a complete dust band, so these dust families forms arcs/clumps (Reach, 1992). The bands appear in pairs, one at each side of the ecliptic (one with positive, one with negative geocentric latitude). Sykes & Greenberg (1986) suggest that a band pair forms naturally in a timescale of  $10^5$  to  $10^6$  years after asteroids within

a family collide. The brightest band pair is the  $\alpha$ -band pair, which is believed to have originated from the Themis and Koronis asteroidal dust family.

The dust density model presented by Kelsall et al., (1998) is an adapted version of the migrating band model of Reach (1992) that allows for a cut-off of the rings at a minimum radius. The density for a single band is expressed by Eq. 2.5, the contributions of the three bands are added up. The parameters used in this equation are given in Table 2.2.

$$n_{B_i}(X, Y, Z) = \frac{3n_{3B_i}}{R} \exp \left[ - \left( \frac{\zeta_{B_i}}{\delta_{\zeta_{B_i}}} \right)^6 \right] \left[ v_{B_i} + \left( \frac{\zeta_{B_i}}{\delta_{\zeta_{B_i}}} \right)^{p_{B_i}} \right] \left[ 1 - \exp \left[ - \left( \frac{R}{\delta_{RB_i}} \right)^{20} \right] \right] \quad (2.5)$$

Table 2.2: Asteroidal band parameters

cloud component	parameter	Description	COBE fitted mean value
Dust Band 1	$n_{B1}$	density at 3AU	$5.59 \times 10^{-10} \text{ AU}^{-1}$
	$\delta_{\zeta_{B1}}$	shape parameter	$8.78^\circ$
	$v_{B1}$	shape parameter	0.10
	$p_{B1}$	shape parameter	4
	$i_{B1}$	inclination	$0.56^\circ$
	$\Omega_{B1}$	ascending node	$80.0^\circ$
	$\delta_{RB1}$	inner radial cutoff	1.5 AU
Dust Band 2	$n_{B2}$	density at 3AU	$1.99 \times 10^{-9} \text{ AU}^{-1}$
	$\delta_{\zeta_{B2}}$	shape parameter	$1.99^\circ$
	$v_{B2}$	shape parameter	0.90
	$p_{B2}$	shape parameter	4
	$i_{B2}$	inclination	$1.2^\circ$
	$\Omega_{B2}$	ascending node	$30.3^\circ$
	$\delta_{RB2}$	inner radial cutoff	0.94 AU
Dust Band 3	$n_{B3}$	density at 3AU	$1.44 \times 10^{-10} \text{ AU}^{-1}$
	$\delta_{\zeta_{B3}}$	shape parameter	$15.0^\circ$
	$v_{B3}$	shape parameter	0.05
	$p_{B3}$	shape parameter	4
	$i_{B3}$	inclination	$0.8^\circ$
	$\Omega_{B3}$	ascending node	$80.0^\circ$
	$\delta_{RB3}$	inner radial cutoff	1.5 AU

### Circumsolar ring

While the asteroid bands are caused by Jovian resonances, resonance features are also present for other planets. IRAS and Spitzer observed that dust particles in resonance with the Earth's orbit form a circumsolar ring of dust as the same heliocentric distance as the Earth (Jackson & Zook, 1989). The ring itself is not smooth, but seems to have some higher and lower density regions. The most prominent features in the disk are the Earth trailing and leading dust clumps that show yearly variations in brightness (Dermott et al., 1994). Once particles enter an Earth-resonance orbit they remain trapped for  $500 - 10^4$  years. Although yearly variations are present, the ring is often modelled as being stable over time.

The model used for the COBE mission is also a stable model that does not show the variations in thickness as a function of time (Kelsall et al., 1998). It consists of a circular toroid model that represents a smooth contribution to the ring. Furthermore an Earth trailing high density region is present that is fixed in orientation with respect to the Earth. It is assumed that the orbit of this high density region is circular. The optical thickness is expressed as shown in Eq. 2.6, the parameters are given in Table 2.3.

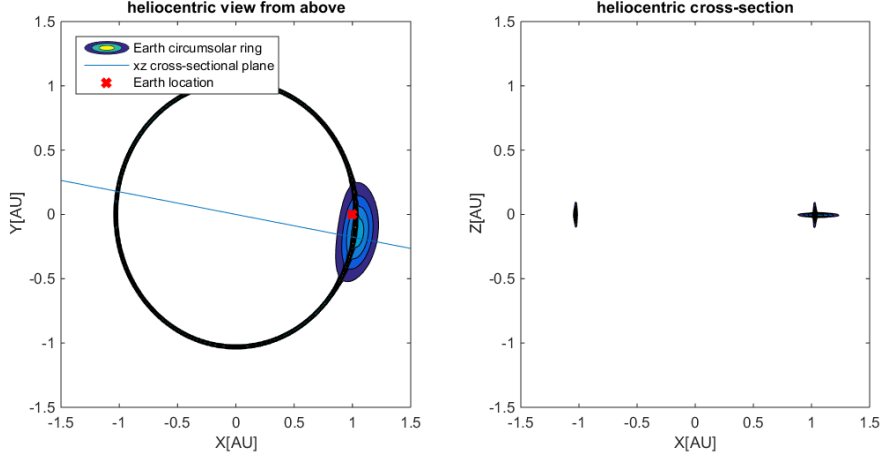


Figure 2.3: Isodensity contours of the Earth circumsolar ring and trailing blob. Left: view in the heliocentric plane XZ, indicating the line for the cross-section at the right. Right: cross-section in XZ of the Earth circumsolar ring at the line indicated at the left image. Isodensity contours are shown for  $[0.2, 0.4, 0.6, 0.8, 1.0, 1.2, 1.4, 1.6, 1.8, 2.0]n_{SR}$  with  $n_{SR}$  the density of the solar ring at 1AU

$$n_R(X, Y, Z) = n_{SR} \exp \left[ -\frac{(R-R_{SR})^2}{2\sigma_{rSR}^2} - \frac{|Z_R|}{\sigma_{zSR}} \right] + n_{TB} \exp \left[ -\frac{(R-R_{TB})^2}{2\sigma_{rTB}^2} - \frac{|Z_R|}{\sigma_{zTB}} - \frac{(\theta-\theta_{TB})^2}{2\sigma_{\theta TB}^2} \right] \quad (2.6)$$

Table 2.3: Earth circumsolar ring parameters

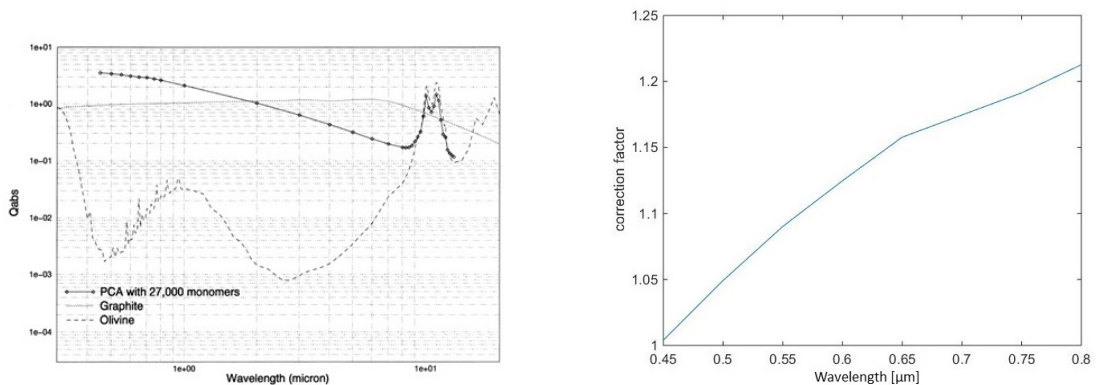
cloud component	parameter	Description	COBE fitted mean value
Solar Ring	$n_{SR}$	density at 1AU	$1.83 \times 10^{-8} \text{ AU}^{-1}$
	$R_{SR}$	radius of peak density	1.03 AU
	$\sigma_{rSR}$	radial dispersion	0.0025AU
	$\sigma_{zSR}$	vertical dispersion	0.054 AU
	$i_{RB}$	inclination	$0.49^\circ$
	$\Omega_{RB}$	ascending node	$22.3^\circ$
Trailing Blob	$n_{TB}$	density at 1AU	$1.9 \times 10^{-8} \text{ AU}^{-1}$
	$R_{TB}$	radius of peak density	1.06 AU
	$\sigma_{rTB}$	radial dispersion	0.10AU
	$\sigma_{zTB}$	vertical dispersion	0.0091 AU
	$\theta_{TB}$	longitude w.r.t Earth	$-10^\circ$
	$\sigma_{\theta TB}$	longitude dispersion	$12.1^\circ$

### 2.1.2. Transformation of the optical thickness model to VIS domain

The optical thickness of a medium depends on the frequency in which it is observed. Hence also the optical thickness model of the zodiacal dust is valid only for a certain frequency. As the model of the COBE mission is used to describe the optical thickness in the infrared (IR) domain it needs to be transformed to represent the visual (VIS) domain in which LOUPE shall observe the Earth, which is from 400-800nm. This transformation is done using the extinction cross-section of the dust particles at these two different frequency domains, as this is a measure for the amount of light that is scattered and absorbed. If the extinction cross-section of the dust particles is known in the IR domain and the VIS domain, the optical thickness model can be linearly scaled with the ratio of the cross-sections.

Finding the absorption cross-section of dust particles in the IR and VIS domain is a challenging task. Not only because data is often not published, but also because it is not known exactly what these dust particles look like. As was already mentioned in section 3.1.3 it is known that dust particles are aggregates. Modelling these aggregates however requires to make a lot of assumptions and their validity has only been partially discussed. There are, for example, different ways a particle aggregate can be built up. One way is the Ballistic Particle-Cluster Aggregation which occurs when a lot of monomers are present or if they are continuously being produced. The resulting aggregate is relatively closely packed (e.g. Levasseur-Regourd et al., 1997; Dominik & Tielens 1997). The Ballistic Cluster-Cluster Aggregation type occurs when predominantly clusters of monomers collide with each other. Aggregates of this type are relatively fluffy. The amount, size, shape and the material (determining the refractive index) of the individual monomer are also subject of the assumptions to be made.

For this thesis the work of Nakamura (1998) was used, in which the optical properties of dust aggregates in the disk of  $\beta$  Pictoris are described using a Discrete Dipole Approximation method for fluffy particles generated using Particle-Cluster Aggregation (PCA). Each dust particle consists of 27,000 monomers that each consist of a silicate core and a graphite mantle in accordance with (Greenberg, 1982). Slight modifications were made in the exact constitution of the material to match the silicate features as measured for the dust disk around  $\beta$  Pic.



(a) Absorption cross-section of the PCA simulated dust particles consisting out of 27,000 monomers. (Nakamura, 1998)

(b) Ratio of the absorption cross section at the indicated wavelength over the wavelength at  $2.5\mu\text{m}$

Figure 2.4: Absorption cross section for dust particles in  $\beta$  Pictoris and the ratio's that were found to correct the IR optical thickness models for the visual domain.

Although the dust around  $\beta$  Pic is thought to be slightly different from the zodiacal dust found in our Solar System, the results for  $\beta$  Pic dust particles found in (Nakamura, 1998) are used to adapt the optical thickness model of the dust in our Solar system to the visual domain. The differences between zodiacal dust and the dust orbiting  $\beta$  Pic are predominantly in the infrared domain, as the dust around  $\beta$  Pic shows a silicate feature around  $10\mu\text{m}$  that is not present for the dust in the Solar System (Telesco & Knacke, 1991). Therefore it is expected that if the results presented by (Nakamura, 1998) are used for wavelengths  $< 10\mu\text{m}$  (which it is as for LOUPE the domain of interest is the visible) it is a valid assumption to make.

The simulated absorption cross-section of the simulated PCA particles with 27,000 monomers can be found in Fig. 2.4a. Although in (Kelsall et al., 1998) it is noted that the COBE model should be valid for frequencies from  $(1.25 - 240\mu m)$ , only three observational wavelengths were used to fit the COBE data namely  $1.25$ ,  $2.2$  and  $3.5\mu m$ . Therefore as a reference the absorption cross-section was chosen at  $2.5\mu m$ . In Fig. 2.4b the ratios of the absorption cross-section in the visual domain with respect to the cross-section at  $2.5\mu m$  can be found. As such this graph can be used to scale the observations in the visual domain with the COBE/DIRBE optical thickness of the cloud. For example, to model the zodiacal cloud at  $600nm$  the optical thickness model as discussed in section 2.1.1 should be multiplied with 1.13.

### 2.1.3. Adapting the model for the Earth circumsolar ring

It appears that the COBE/DIRBE model (Kelsall et al., 1998) does not represent the Earth circumsolar ring correctly. Dermott et al., (1994) have shown that the Earth circumsolar ring is a structure with higher and lower density regions, see Fig. 2.5. In this figure the Earth trailing and leading blob is clearly visible.

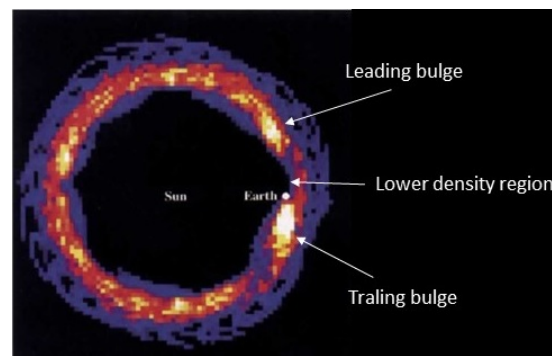
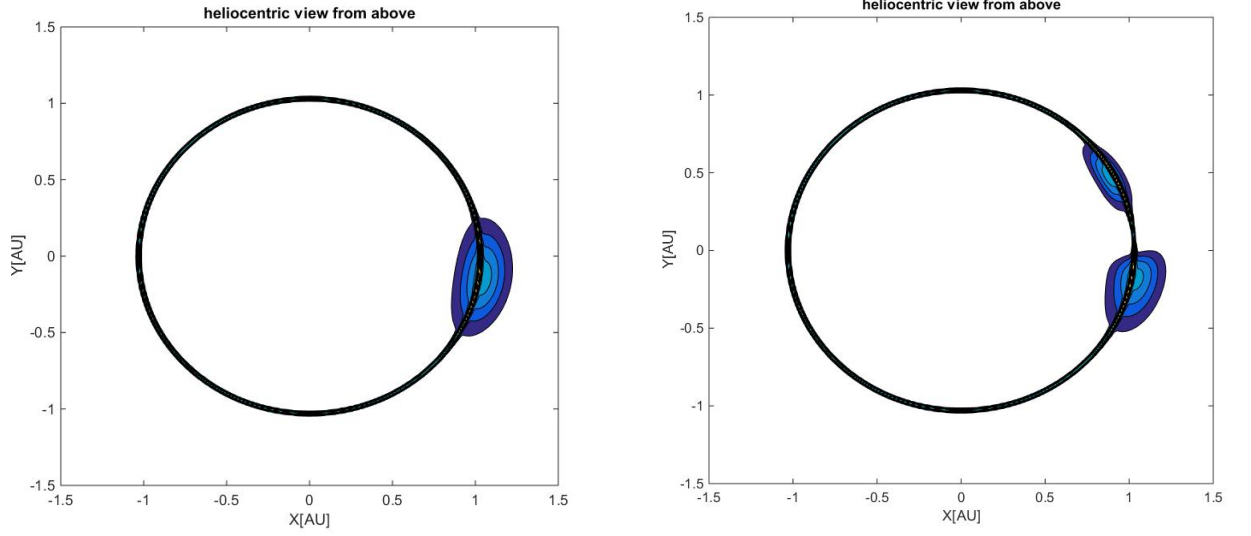


Figure 2.5: Result of a numerical simulation of the structure of Earth's heliocentric dust ring. The frame is centered on the Sun and co-rotates with the Earth. (Dermott et al., 1994). The leading and trailing high density regions are clearly visible.

The Earth leading blob is not present in the model of Kelsall et al., (1998) that is shown in Fig. 5.8a. Furthermore the shape of the Earth trailing blob does not match the simulation. Therefore it was decided to create an adapted version of the Earth circumsolar ring and use both the original model and the adapted model for the simulation. The adapted model has an additional buldge leading the Earth in its orbit and a negative density region was added to the model to account for the lower density region in the Earth's vicinity (directly leading the Earth in its orbit). The parameters used for these regions can be found in Table 2.4. The original model is shown as a reference in Fig. 5.8a, the adapted model in Fig. 5.9a



(a) Original model

(b) Adapted model

Figure 2.6: Isodensity contours of the Earth circum-solar ring models. Isodensity contours are shown for  $[0.2, 0.4, 0.6, 0.8, 1.0, 1.2, 1.4, 1.6, 1.8, 2.0]n_{SR}$  with  $n_{SR}$  the density of the smooth ring component at 1AU

Table 2.4: Parameters for the additional leading blob in the Earth circum-solar ring and the negative density region.

cloud component	parameter	Description	COBE fitted mean value
Leading Blob	$n_{LB}$	density at 1AU	$1.3 \times 10^{-8} \text{ AU}^{-1}$
	$R_{LB}$	radius of peak density	1.0 AU
	$\sigma_{rLB}$	radial dispersion	0.05AU
	$\sigma_{zLB}$	vertical dispersion	0.007 AU
	$\theta_{LB}$	longitude w.r.t Earth	$30^\circ$
	$\sigma_{\theta LB}$	longitude dispersion	$8^\circ$
Negative density region	$n_{NB}$	density at 1AU	$-2.3 \times 10^{-8} \text{ AU}^{-1}$
	$R_{NB}$	radius of peak density	1.03 AU
	$\sigma_{rNB}$	radial dispersion	0.10AU
	$\sigma_{zNB}$	vertical dispersion	0.004 AU
	$\theta_{NB}$	longitude w.r.t Earth	$3^\circ$
	$\sigma_{\theta NB}$	longitude dispersion	$5^\circ$

## 2.2. Model of $\beta$ Pictoris' dust disk

The dust disk present in the  $\beta$  Pictoris planetary system is often discussed in literature. Its optical thickness is relatively high and the disk is seen close to edge on and hence the dust disk can be observed well. The disk itself shows resonant structures that are thought to be a result of orbiting planet  $\beta$  Pic b and probably other planets. The disk as observed by Hubble can be seen in Fig. 2.7.

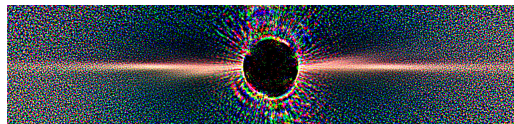


Figure 2.7: Observed disk of  $\beta$  Pictoris by Hubble Space telescope<sup>1</sup>. The star is blocked out by a coronagraph, resulting in the black disk in the center.

The recent paper of Millar-Blanchaer et al., (2015) in which observations by the Gemini Planet Imager (GPI) and models of polarized light scattered by the  $\beta$  pictoris dust disk are presented, is the reason why this disk is chosen as a subject of study. The density model used in (Millar-Blanchaer et al., 2015) is a classical fan model (see Section 2.1), which is adapted to include an additional density variation as a function of ecliptic latitude. A resulting cross-section of the density model is shown in Fig. 2.8. The reference isodensity is not mentioned in the paper and therefore it is adapted from (Artymowicz, 1997) who reports an optical density of  $8.5e-3 AU^{-1}$  at 50AU.

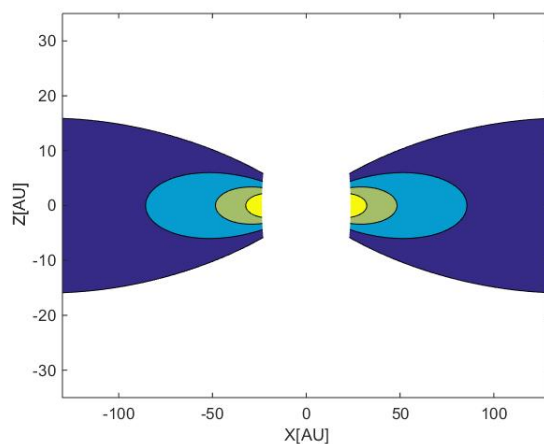


Figure 2.8: Isodensity contours of the modified classical fan model as presented in (Millan-Blanchaer et al., 2015) using a reference optical density of  $\rho_0=8.5e-3 AU^{-1}$  at 50AU (Artymowicz, 1997). Isodensity contours are shown at [0.2 0.4 0.6 0.8] of the density at 1AU.

### 2.2.1. SMACK collisional model

The modified classical fan model presented by (Millan-Blanchaer et al., 2015) does not represent any detailed density structures, such as the warp that can be seen in Fig. 2.7. This apparent X-like structure is well discussed in literature and often subjected to reconstruction simulations.

Recently the Superparticle-Method Algorithm for Collisions in Kuiper belts (SMACK) was presented by M.J. Kuchner and E.R. Nesvold (Nesvold & Kuchner, 2015), a computational code which allows to analyze the location of planetesimal collisions in Kuiper belts and debris disks. With this they have simulated the collisional locations of debris in a  $\beta$  Pic like disk and calculated how much dust was produced upon every collision. The addition of a planet with properties similar to  $\beta$  Pic b has shown that the X-like structure is caused by the stirring effect of this planet on the disk. Until now the X-warp was often modelled using two disks: a large main one and an inclined smaller one (e.g. Backman et al., 1992; Ahmic et al., 2009). Therefore the SMACK model is the first to explain observations with a single

<sup>1</sup>Retrieved from <https://www.spacetelescope.org/images/opo0625b/>

and smooth model. As the SMACK model is based on orbital mechanics of the debris in the disk it is concluded during the thesis research that this is currently the most reliable basis for the construction of an optical thickness model. The SMACK dataset with collisional locations and masses was provided by E.R. Nesvold by e-mail and the collisional locations are shown in Fig. 2.9.

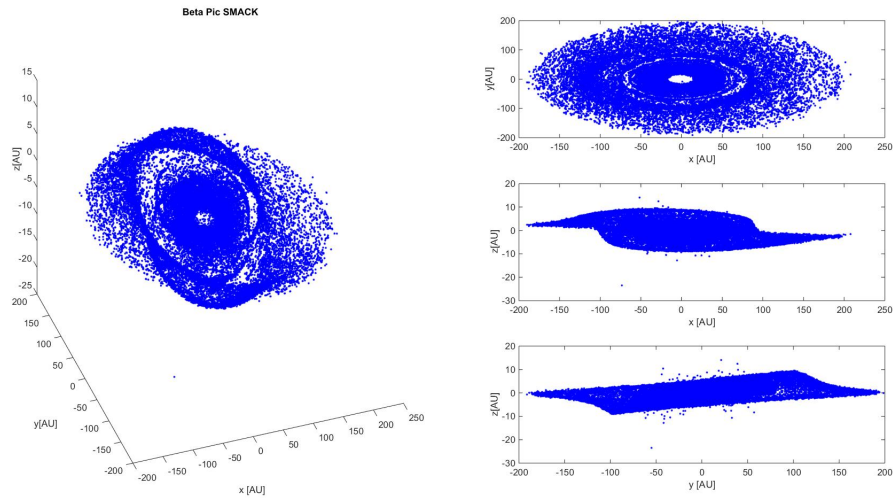


Figure 2.9: Location of the planetesimal collisions as calculated by SMACK between 10-10.1 MY. These figures were created with MATLAB using the SMACK data provided by E. Nesvold.

## 2.2.2. Transformation of SMACK model into an optical thickness model

The SMACK dataset represents the location of collisions and the dust mass produced. It does not provide the optical thickness. Hence it is necessary to process this data before it can be transformed into an optical thickness model of the dust cloud. In reality orbits of the produced dust particles are immediately changed under the influence of Poynting-Robertson drag and Solar radiation pressure. Poynting-Robertson drag causes particles that are not small enough to be blown out of the Solar System to spiral towards the sun, as the solar radiation causes the particle to continuously lose angular momentum. Unfortunately the orbits of the dust particles given in the SMACK dataset are not known which are necessary to derive the optical thickness. By data processing the dataset is smoothed and this problem partially avoided.

The optical thickness models of the Solar System is a function of heliocentric coordinates. It is not possible to represent the optical thickness model that shall be derived from SMACK in this way. Rather an average optical thickness shall be defined for grid cells that cover the complete dust cloud. The grid cells are part of a sphere and are located along the azimuth, elevational and radial directions. As such the resulting optical thickness can be represented by a 3D matrix that contains the average thickness for each grid cell. Further explanation on grid cells can be found in Section 4.2.1.

### Data selection

Some of the original datapoints are grouped in trails and represent the effect of debris parts that collide when in a resonant orbit, see Fig. 2.10.

When the mass of the dust producing planetesimals is large, the local dust density is high, especially in the case a dust trail is produced. If the locations of these collisions are kept in the datafile, the produced dust mass at these locations is high, whether in reality the orbits of the dust produced have evolved and the dust has been spread out. Hence it is undesired to take the contribution of the dust trails in account in the optical density model.

Therefore 20% of the datapoints is removed that yield the largest instantaneous dust mass produced. The dust masses of the remaining dataset is binned in the reference grid cells to yield a total dust mass

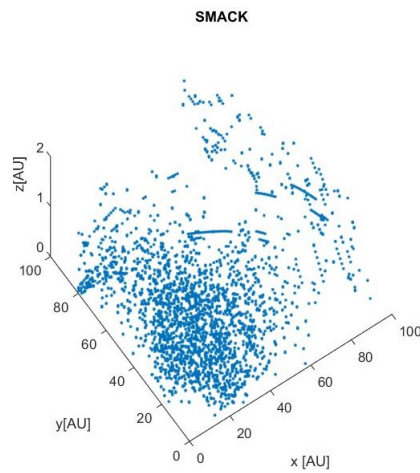


Figure 2.10: Location of the planetesimal collisions as calculated by SMACK between 10-10.1 MY. This zoom clearly shows trails of collisions. These figures were created with MATLAB using the SMACK data provided by E. Nesvold.

per reference grid cell. To smoothen the data even more the data is averaged with its surrounding grid cells. The resulting matrix that now contains a dust mass for each grid cell can be made visible using a set of randomly generated dust locations that are weighed to the grid cell value see Fig. 2.11

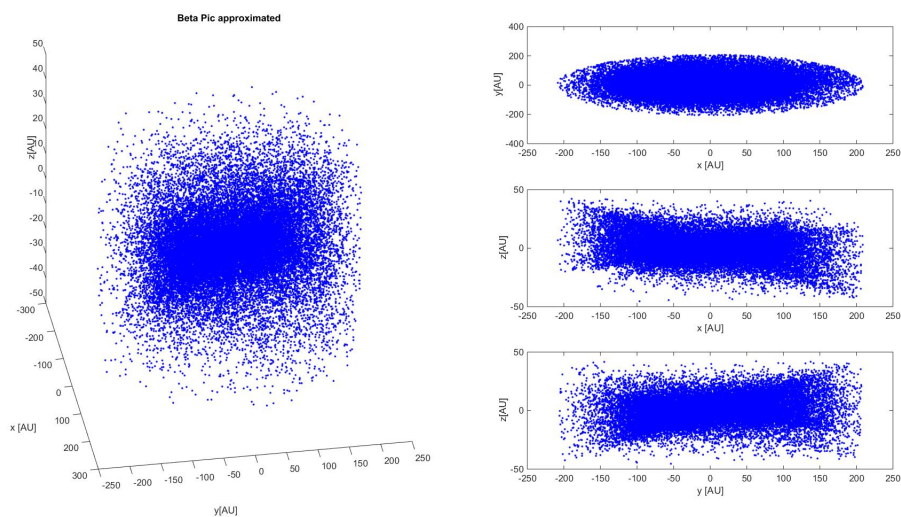


Figure 2.11: Normalized density model of the dust disk around star  $\beta$  Pictoris. The dust mass produced at the locations indicated by SMACK are binned for each grid cell in ZPEC. The mass distribution in the grid cells is normalized to the maximum mass in one of the grid cells, then multiplied by 1000. Therefore the grid cell with maximum dust density shows 1000 dust locations, less dust particles are located in the other grid cells. This view has 30 azimuthal bins, 10 elevation bins and 10 radial bins.

### Conversion to optical thickness

A conversion is necessary to obtain the cloud optical thickness from the matrix containing the cumulative dust mass. Again the reference optical thickness is adapted from (Artymowicz, 1997) and equals  $8.5e-3 AU^{-1}$  at 50AU. It is assumed this optical thickness is derived from observations and hence contains information along the line of sight. It is therefore assumed that this is the average optical density along the line of sight in the symmetry plane of the dust cloud at 50AU.

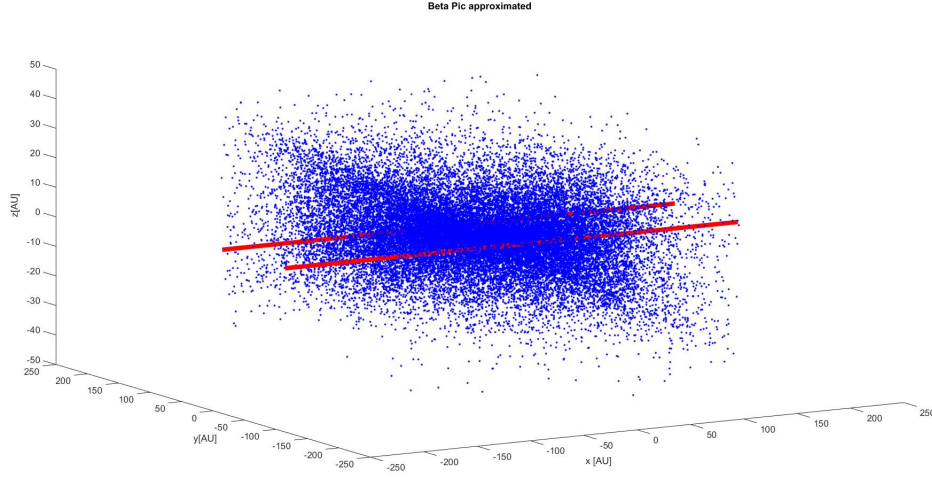


Figure 2.12: Similar to Fig. 2.11, the normalized dust density model of the dust disk around star  $\beta$  Pictoris. In addition to Fig. 2.11 two lines of sight are shown in red which are used to retrieve the optical density model from the normalized density model

This assumption is used to draw two lines of sight in the disk of  $\beta$  Pic, see Fig 2.12 at 50AU from the center of the disk (seen as by a distant observer, so these lines are parallel with the x-axis). For the locations along these two lines the total dust mass in the corresponding grid cell is stored and added, yielding a total cumulative dust mass along the lines of sight. Then the average dust mass per AU is calculated by dividing the cumulative dust mass by the total length of the lines of sight travelling through the reference volume. The reference value of  $8.5e-3 AU^{-1}$  divided by this average cumulative dust mass is used as a scaling factor. The original matrix with cumulative dust mass for each grid cell is multiplied by the scaling factor to obtain the optical thickness matrix.

This procedure results in a density model in which the average optical thickness is  $3.7e-3 AU^{-1}$ . The average optical thickness along the line of sight can be obtained by integrating it over the disk height, it is visible in Fig. 2.13. The line of sight that is referred to now is also parallel to the X-axis and similar to the lines drawn in Fig. 2.12, but now these lines are not located at 50AU but are varied from distances from (0,210) AU. For clarity the optical thickness model that is used by Millan-Blanchaer et al., (2015), a simple fan model, is also shown. It can be seen that at the reference location (50AU) the optical thickness matches well. Closer to the central star the optical thickness is higher than the reference model and in the wing. At distances  $> 20AU$  the largest deviation is  $\simeq 60\%$  at 120AU for the right wing as can be seen in Fig. 2.14. It was decided not to smoothen the optical thickness model even more, as this would remove the SMACK collisional structure for the disk.

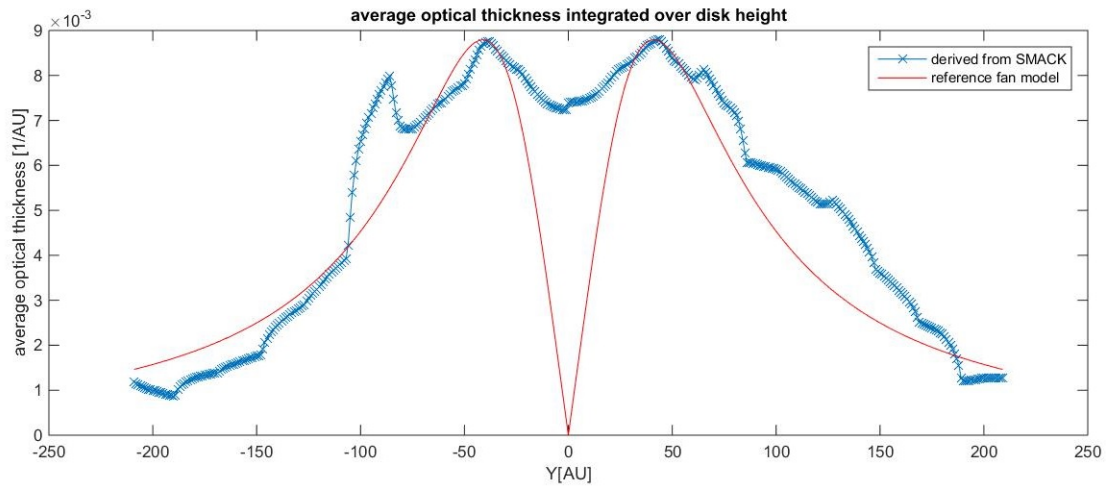


Figure 2.13: The average optical thickness along the observer line of sight looking along the y-direction, integrated over the disk height. Discontinuities are visible for the SMACK model, whereas the reference fan model, the smooth fan model of Artymowicz (1997) does not. The result is an optical thickness integrated in X and Z direction.

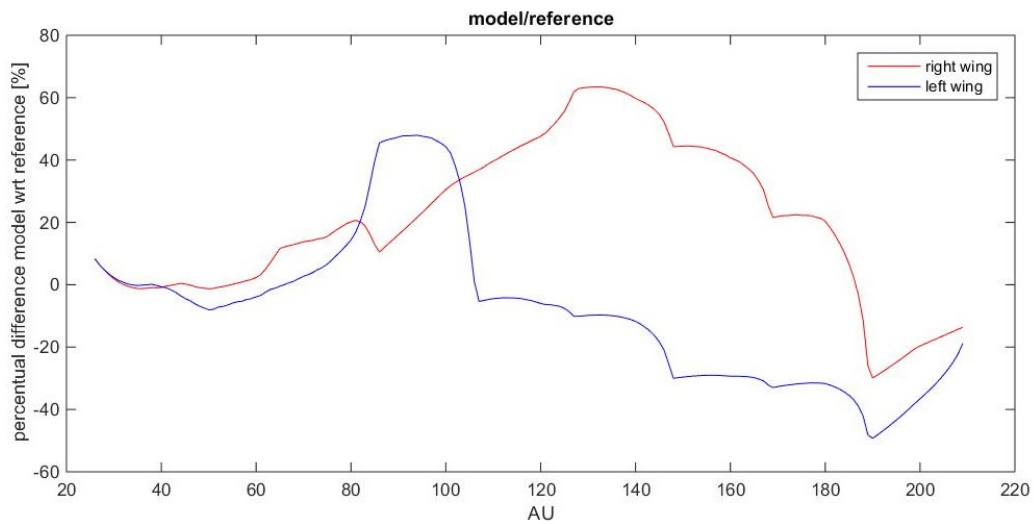


Figure 2.14: Difference in optical thickness between the smooth fan model (Artymowicz, 1997) and the SMACK derived optical thickness model as a function of the distance to the central star (on the horizontal axis). The left wing corresponds with negative Y-coordinates, the right wing with positive Y-coordinates.



# 3

## Single scattering by zodiacal dust particles

Now that the reader has been introduced to the general shape of the cloud, the theory on single scattering by zodiacal dust particles can be discussed as well as the aspects that are of importance to compute multiple scattering. Light scattering by particles is a broad topic that covers several research areas. First the mathematical description of light and scattering shall be given, then more information shall be given on scattering functions in relation to particle properties after which a discussion follows of what is known about the properties of dust in the Solar System.

### 3.1. Introduction to single light scattering

Light travels as an electromagnetic wave that can be mathematically described by wave functions (Hansen & Travis, 1974). The light has two components: an electric field and a magnetic field that can both be described by a vector. Light travels in a certain direction, that we call  $z$ , and is characterized by its circular frequency  $\omega$ . The intensity of the light radiation can be sensed by our human eye and instruments, which is the 'rate of energy flow across a unit area perpendicular to the direction of propagation' (Hansen & Travis, 1974).

#### 3.1.1. Polarization degree of light

When taking a closer look at the plane perpendicular to the direction of propagation, the electric vector traces out an ellipse over time, see Fig 3.1, which is called the polarization ellipse. In special cases the light is completely polarized and the electric vector traces out a preferred shape that is identical for each wave. The preferred shape that is traced out by the electrical field vector is not necessarily an ellipse; it can also be a line or a circle. On the other hand the electric field vector of natural light (such as direct Sunlight) traces out shapes that are completely uncorrelated and the light is unpolarized. Often only a part of the light has a preferred direction and the total light beam consists of a polarized and unpolarized part. Using the intensity of the beam,  $I$ , this can be mathematically described as:

$$I = I_{unpol} + I_{pol} \quad (3.1)$$

Where the degree of polarization is defined as the ratio of the polarized over the total intensity  $P = \frac{I_{pol}}{I}$ . In general the beam is elliptically polarized, which can be separated in a linear part  $I_{lp}$  and a circular part  $I_{cp}$

$$I_{pol} = \sqrt{I_{lp}^2 + I_{cp}^2} \quad (3.2)$$

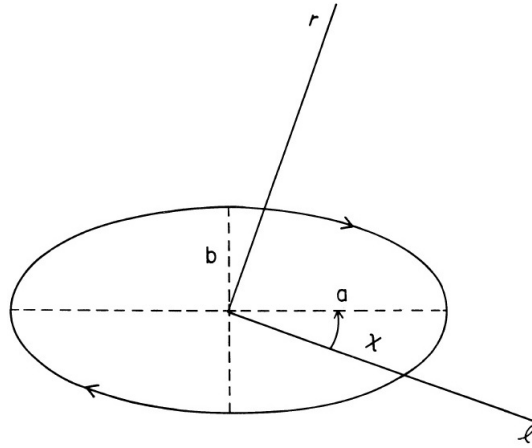


Figure 3.1: Illustration of the polarization ellipse. The propagation direction is into the page and the indicated sense of rotation corresponds to right-handed polarization (Hansen & Travis, 1974). In this illustration  $a$  is the elliptic half-major axis,  $b$  is the elliptic half minor-axis,  $\mathbf{r}$  and  $\mathbf{l}$  are unit axes perpendicular to the direction of propagation,  $X$  is the angle which the major axis makes with the  $\mathbf{l}$  direction.

The electric vector of a light wave is expressed by vector  $\mathbf{E}$ . This vector can be described using two vectors in two perpendicular directions that are represented by unit vectors  $\mathbf{r}$  and  $\mathbf{l}$  (see Figure 3.2) that both have a magnitude ( $a_l, a_r$ ) and phase  $\epsilon_l$  and  $\epsilon_r$  (Hansen & Travis, 1974);

$$E_l = a_l e^{i(\omega t - kz - \epsilon_l)}; \quad E_r = a_r e^{i(\omega t - kz - \epsilon_r)} \quad (3.3)$$

Where  $t$  represents time,  $i = \sqrt{-1}$ ,  $k$  is the wavenumber defined as and  $\mathbf{r} \times \mathbf{l}$  is the direction of propagation. In case of a single scattering event  $\mathbf{r}$  is chosen perpendicular to the plane of scattering (containing the plane indicating the directions of incidence and scattering).

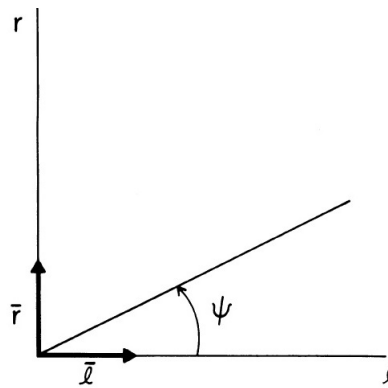


Figure 3.2: Illustration of unit vectors  $\mathbf{l}$  and  $\mathbf{r}$  and angle  $\psi$ . The direction of propagation is into the plane. (Hansen & Travis, 1974)

The importance of the expressions for  $E_l$  and  $E_r$  is clear when light is expressed using the Stokes Parameters which results in the so-called Stokes vector ( $\delta = \epsilon_l - \epsilon_r$ );

$$\begin{bmatrix} I \\ Q \\ U \\ V \end{bmatrix} = \begin{bmatrix} a_l^2 + a_r^2 \\ a_l^2 - a_r^2 \\ 2(a_l a_r \cos \delta) \\ 2(a_l a_r \sin \delta) \end{bmatrix} \quad (3.4)$$

The Stokes vector is relevant for this thesis research as it is a way to obtain 'measurements' of polarization (Hansen & Travis, 1974). To explain this, suppose  $E_r$  is continuously delayed with factor  $\epsilon$  with respect to  $E_l$ . Now call  $I(\psi, \epsilon)$  the intensity of light as a function of this delay and the angle of the electric field vector with respect to its unit vector  $\mathbf{l}$ . Then it follows that:

$$I(\psi, \epsilon) = \frac{1}{2} [I + Q \cos 2\psi + (U \cos \epsilon + V \sin \epsilon) \sin 2\epsilon] \quad (3.5)$$

From which it can be derived that:

$$\begin{bmatrix} I \\ Q \\ U \\ V \end{bmatrix} = \begin{bmatrix} I(0^\circ, 0) + I(90^\circ, 0) \\ I(0^\circ, 0) - I(90^\circ, 0) \\ I(45^\circ, 0) - I(135^\circ, 0) \\ I(45^\circ, \pi/2) - I(135^\circ, \pi/2) \end{bmatrix} \quad (3.6)$$

(Note that  $I(0^\circ, 0) + I(90^\circ, 0)$  equals  $I_l + I_r$  and  $I(0^\circ, 0) - I(90^\circ, 0)$  equals  $I_l - I_r$ .)

Or in other words:  $I$  represents the total intensity of the beam,  $Q$  is the lineary polarized flux in  $l$  direction ( $\psi = 0^\circ$ ) minus lineary polarized flux in  $r$  direction,  $U$  is the lineary polarized flux in direction of  $\psi = 45^\circ$  minus the lineary polarized flux in  $\psi = 135^\circ$  and  $V$  is the excess intensity of right-handed circular polarization over left-handed circular polarization. It means that the total lineary polarized intensity can be written as  $I_{lp} = \sqrt{Q^2 + U^2}$ , and the intensity of circularly polarized light  $I_{cp} = V$ . Hence the degree of polarization can be written as;

$$P = \frac{I_{pol}}{I} = \frac{\sqrt{Q^2 + U^2 + V^2}}{I} \quad (3.7)$$

### 3.1.2. Describing scattering behavior using scattering functions

If the incoming flux is unpolarized (as is the case for natural light) only scattering by particles, such as dust particles, can cause a beam of light to become polarized. The way light is polarized depends on the nature of the particle, therefore the relation between the reflected Stokes vector  $I$  as a function of the incoming Stokes vector  $I_0$  characterizes the particle. The relation itself is expressed by the scattering matrix  $F$ . The scattering matrix is a function of the scattering angle  $\theta$  which is the angle under which the light is deflected from its normal path when scattered by a dust particle, see Fig. 3.3. The phase angle is understood as  $\pi - \theta$ . Both are used in this report.

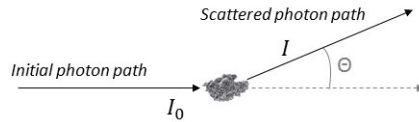


Figure 3.3: Illustration of scattering angle

Classically the relation between the incoming flux vector  $I_0$  and the scattered flux vector  $I$  is given as;

$$I(\theta) = \begin{bmatrix} F_{11}(\theta) & F_{12}(\theta) & F_{13}(\theta) & F_{14}(\theta) \\ F_{12}(\theta) & F_{22}(\theta) & F_{23}(\theta) & F_{24}(\theta) \\ F_{13}(\theta) & -F_{23}(\theta) & F_{33}(\theta) & F_{34}(\theta) \\ F_{14}(\theta) & F_{24}(\theta) & -F_{34}(\theta) & F_{44}(\theta) \end{bmatrix} I_0 \quad (3.8)$$

It is often assumed that the particles in a scattering medium are symmetric or have a similar amount of mirror particles and are in addition randomly oriented. For such type of particles the scattering matrix reduces to (Hansen & Travis, 1974):

$$F = \begin{bmatrix} F_{11}(\theta) & F_{12}(\theta) & 0 & 0 \\ F_{12}(\theta) & F_{22}(\theta) & 0 & 0 \\ 0 & 0 & F_{33}(\theta) & F_{34}(\theta) \\ 0 & 0 & -F_{34}(\theta) & F_{44}(\theta) \end{bmatrix} \quad (3.9)$$

If the scattering medium is optically thin it is likely that the individual photons are only scattered once before they are observed. It is then possible to reconstruct the scattering functions  $F(\theta)$  based on

observations, if the amount of scattering particles is known. Hence, for optically thin media the first order properties of singly scattered light can be derived using the scattering matrix with the scattering functions  $F(\theta)$ . The scattering functions of various samples can be found in the Amsterdam-Granada Light Scattering Database (Muñoz et al., 2012).

In case the incoming light is unpolarized and the light is scattered only once, the polarization degree reduces to  $P = \frac{-F_{12}(\theta)}{F_{11}(\theta)}$  (Hansen & Travis, 1974). The reader might notice that there is a difference between this notation and the notation used in Eq. 3.7. It should hence be noted that the expression in Eq. 3.7 only describes the *magnitude* of the polarized part of the light. The expression  $P = \frac{-F_{12}(\theta)}{F_{11}(\theta)}$  also holds information on the direction of polarization.

An example of a set with scattering matrix scattering functions can be found in Fig. 3.4. For this example the functions were retrieved using measurements of scattered laser light by a sample of volcanic ash. It can be seen that for small scattering angles (hence in forward scattering direction) the  $F_{11}(\theta)$  function shows high values, which means that these particles scatter the light primarily in forward direction.

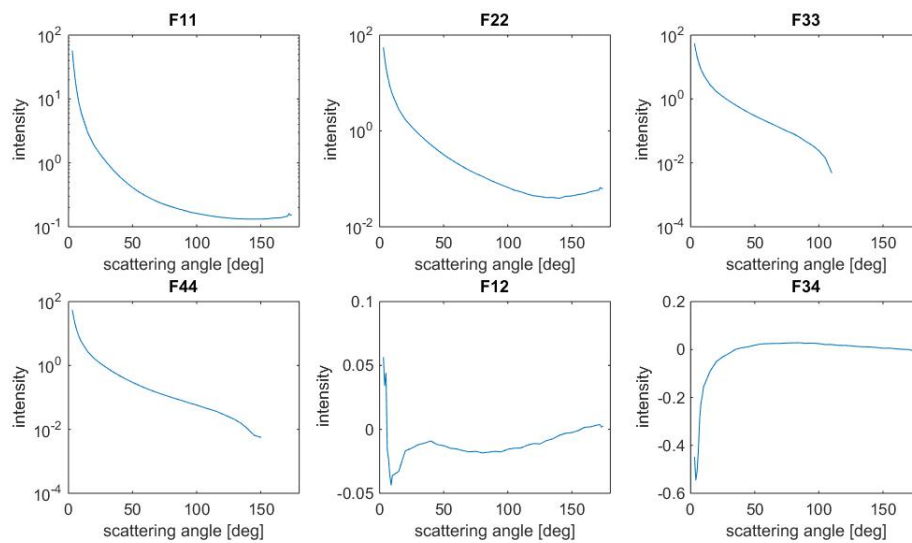


Figure 3.4: Scattering matrix elements of Spurr Gunsight volcanic ash, measured at a wavelength of 632.8nm (Muñoz et al., 2004).  $F_{11}$  is normalized to 1 at a scattering angle of  $\theta = 30^\circ$

### 3.1.3. Scattering regimes

The most important factor that influences how light is scattered is the wavelength of the light with respect to the particle size. The latter is expressed by the dimensionless size parameter  $x = \frac{2\pi R}{\lambda}$  in which  $R$  is the radius of the particle and  $\lambda$  the wavelength. Depending on this parameter, scattering of light can be distinguished in three regimes;

- For  $x \gg 1$  one speaks of optical scattering in the geometric optics regime. All wavelengths of the light are scattered in the same way.
- For particles with  $x \approx 1$ , Mie scattering applies when bodies are spherical particles. The light is scattered in an inhomogeneous way i.e. the observed scattering light depends on phase angle and wavelength. The phase scattering function is often strong in the forward regime.
- For particles with  $x \ll 1$  Rayleigh scattering applies which is predominantly seen for gases. When these small particles are ‘hit’ by light, their electric field starts to move with the same frequency as the light. This causes the particle to become a small radiating dipole that absorbs all the incoming radiation and emits it which is observed as the scattered light. The observed scattered light depends on both phase angle and wavelength. The scattered intensity is (about) equal for all scattering angles.

For each of these different scattering regimes, different sets of equations and numerical approaches exist to approximate scattering and absorption properties, refractive indices and wavelength dependence (Hovenier & Muñoz, 2009). The description of light that is scattered by zodiacal dust particles is complicated as zodiacal dust particles are often aggregates of individual monomers that have grown to larger structures during their lifetime. Therefore the dust particles themselves are irregular in shape and can contain different materials.

## 3.2. Properties of dust particles in the Solar System

The observed scattered light is influenced by two distinct groups of variables. The first group contains the observational parameters such as scattering angle. This means that, for example, certain particles show stronger forward scattering features than others. The characterization of particles by remote observations is amongst other things based on this characteristic. The second group with variables that influence the light scattering concerns the particle properties. It may be clear that the differences in scattering functions are caused by a difference in particle properties e.g. material and structure.

### 3.2.1. The shape, structure and material of IDPs

Interplanetary dust particles are believed to have similar properties as cometary dust. Greenberg (1982) states that cometary dust particles are likely fractal aggregates consisting of elongated monomers i.e. monomers of the prolate type with a core and a mantle, see Fig. 3.5.

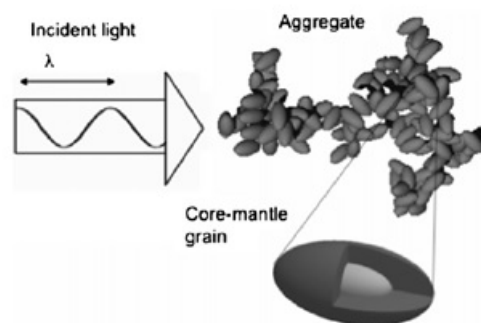


Figure 3.5: A fractal aggregate that is built up of small prolate grains with a silicate core and an organic mantle. In this case the effective radius of the particle is on the order of the wavelength. (Levasseur-Regourd et al., 2007)

It is described by Levasseur-Regourd et al., (2007) that the smooth scattering functions found for interplanetary and cometary dust suggest that particles are likely to be aggregates with irregular shapes and a size larger than the wavelength.

In the interplanetary medium different materials can be found but especially silicates tend to accrete to build up particle cores. Such particles are often described as being 'loosely structured particles with high porosity (Katyal, Banerjee & Puri, 2014). When these aggregates are collected in the stratosphere the mantle is often found melted while the core has kept its morphology. It is often found that the mantles of these particles contain an organic compound.

Interplanetary dust particles (IDPs) or zodiacal dust particles are often of the carbonaceous chondrite type, meaning they consist of the most primitive material found in our Solar System. This is supported by a study of Keller, Messenger and Bradley (2000) that presents a detailed study of a highly porous deuterium enriched particle containing olivine and pyroxene. These particles are of the anhydrous type (it lacks water/hydrogen), but also hydrated IDPs are studied meaning they have a silicate layer (Jessberger et al., 2001). In general it can be concluded that particles are a complex mixture of amorphous components and minerals and that the four primary constituents are (e.g. Katyal, Banerjee & Puri 2014):

- Silicates of Iron, Magnesium, Aluminum and Calcium
- Complex organic molecules of Carbon, Hydrogen, Oxygen and Nitrogen

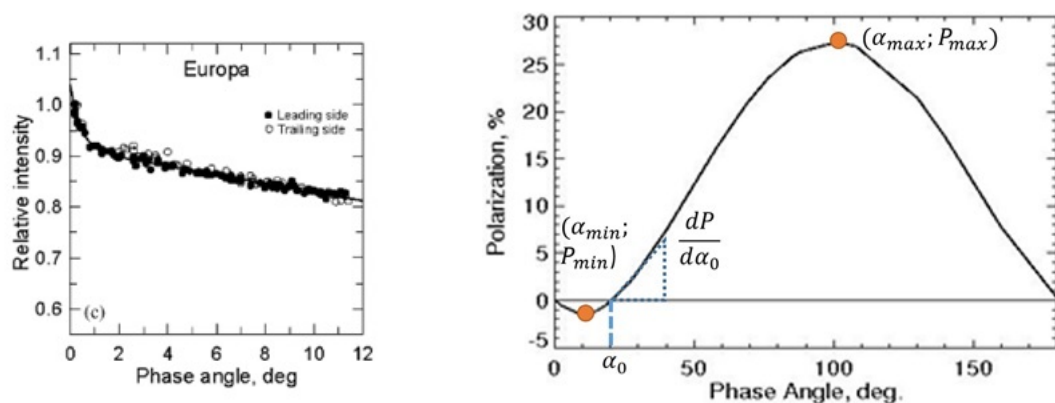
- Small carbonaceous particles of graphite, coal and amorphous carbon
- Ices of Carbon dioxide, water and ammonia The abundance of silicates is large and as was already mentioned is primarily found to accrete to form porous cores (Greenberg, 1982).

As the composition of IDPs largely corresponds to the composition of cometary dust, it is likely IDPs are of cometary origin which supports the hypothesis of Kresak (1980) and Delsemme (1976) although it is known that the dust has evolved under the influence of Solar radiation pressure and Poynting-Robertson drag.

### 3.2.2. Typical flux and polarization features

To characterize dust particles typically flux and polarization are observed, for which in general two functions are important. The first function is the brightness/polarization curve as a function of wavelength, which shows information about the composition of the observed medium through, for example, absorption or emission spectra. The second function is the brightness or polarization curve as a function of phase angle, which provides more information about the particle size or composition/structure of aggregates.

The polarization and brightness phase curves show very particulate features near opposition (phase angle close to  $0^\circ$ ), see Fig. 3.6. These effects are extremely sensitive to albedo, composition and structure of a particular surface or particle (Rosenbush, Kiselev & Avramchuck, 2006) and thus they provide characteristic information on particles, bodies in our Solar System and polydisperse dust media.



(a) A typical Brightness opposition effect for Jovian moon Europa. Source (Rosenbush, Kiselev & Avramchuck, 2006). Please note this curve does not concern individual dust particles but the complete moon. It is therefore only used as an illustration of the BOE.

(b) Typical polarization phase curve for cosmic dust, original retrieved from (Kolokova et al., 2011) edited to show characteristic values that describe the polarization phase curve. Here,  $\alpha_0$  is called the inversion and  $dP/(d\alpha_0)$  the slope at inversion.

Figure 3.6: Examples of brightness and polarization phase functions

The first phenomena that is present for various dust particles is the Brightness Opposition Effect (BOE): a nonlinear intensity increase near opposition for the brightness phase curve. An example of a typical BOE for Jovian moon Europa can be found in Fig. 3.6a. (Please note this curve does not concern individual dust particles as is this curve is valid for the complete moon. It is therefore only used as an illustration of the BOE.) The opposition effect is probably caused by a mechanism called the coherent backscattering mechanism: the interference of waves that travel in the exact backscattering direction are thought to be constructive, causing an increase in brightness near direct opposition and at small angles (e.g. Hovenier & Muñoz 2009).

Also the polarization phase curve shows particular features. An example polarization phase curve is shown in Fig. 3.6b that is typical for cosmic dust. In this image the maximum polarization point  $(\alpha_{max}; P_{max})$  is shown, as well as the the minimum  $(\alpha_{min}; P_{min})$ , the inversion angle  $\alpha_0$  and the slope at inversion  $dP/(d\alpha_0)$ . Typically the polarization curve for dust has a wide positive branch and a small

negative branch near opposition. It is believed the Negative Polarization Branch (NPB) is caused by the coherent backscattering mechanism just like the BOE. The negative polarization effect is described as follows:

- A wide NPB, reaching to about  $25^\circ$ .
- Or a negative (narrow and asymmetric) spike, close to opposition.

The latter is called the Polarization Opposition Effect (POE). A combination of this is also sometimes visible, then we speak of a bimodal phase-angle curve. Two superimposed minima are then visible, one for the POE and one for the NPB.

### 3.2.3. Reconstruction of the zodiacal dust scattering functions

Although the former sections do provide some information on the general shape of the polarization and brightness scattering functions of dust, the information is incomplete. In order to calculate the reflected Stokes vector, it is necessary to know *all* the scattering functions in the scattering matrix  $F_{11}(\theta) \dots F_{44}(\theta)$  and such functions for zodiacal dust were not found in literature. Therefore the information that is given in literature needs to be used to reconstruct the scattering functions. The following information that was found about the zodiacal dust scattering behavior was used for this reconstruction;

- The polarization phase curves of cometary dust and zodiacal dust are similar (Levasseur-Regourd et al., 2007)
- The maximum degree of polarization for zodiacal dust increases with increasing heliocentric distance and latitude (Levasseur-Regourd et al., 2007). The local polarization degree increases from 20% at 0.5AU to 30% at 1AU to (Levasseur-Regourd, 1998).
- The polarization degree of the zodiacal light at 500nm is between -3 and +21 % as measured from Earth.

In the Amsterdam-Granada light scattering database scattering functions can be found that have been constructed using laboratory measurements. The administrator of the database, O. Muñoz advised us to use the scattering functions of an olivine or fosterite particle or the particles of the Allende comet, the polarization functions of these samples can be found in Fig. 3.7. This means that one single phase function shall be used and that the heliocentric dependence of the maximum polarization degree is neglected.

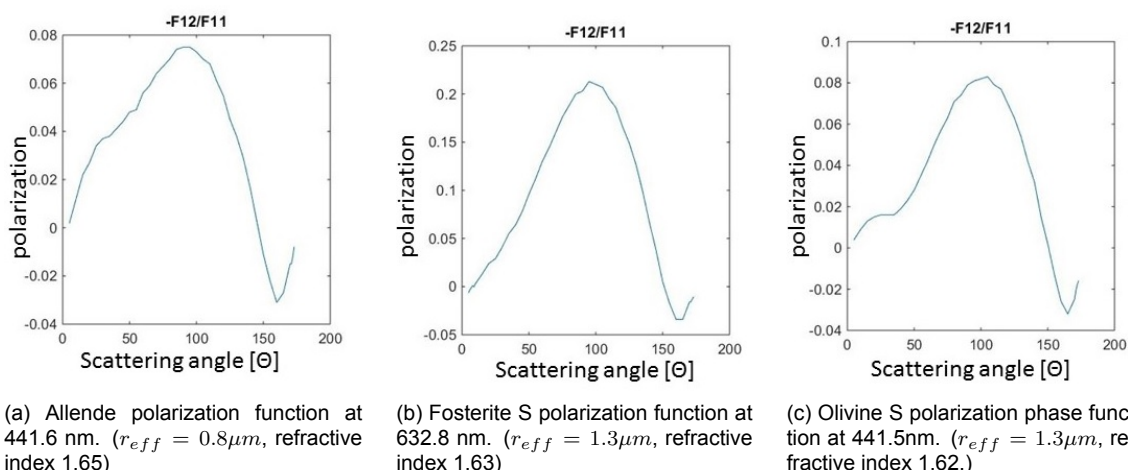


Figure 3.7: Polarization scattering functions of three types of dust particles that could show the behavior of interplanetary dust particles (Muñoz et al., 2012)

It was found that the polarization degree of the fosterite samples (Fig. 3.7b) best matches the expected behavior of interplanetary dust. The scattering functions for the olivine particles (Fig. 3.7c) and the dust particles of the Allende comet (Fig. 3.7a) have a maximum polarization degree that is too low compared

to what information was found in literature. Furthermore their increase in the region around  $\pm 40^\circ$  phase angle is not smooth; for zodiacal dust this phenomenon has not been reported.

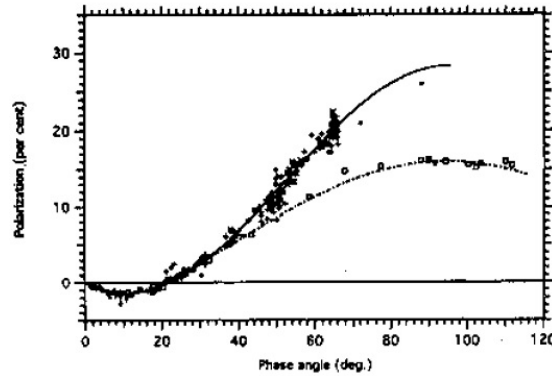


Figure 3.8: Phase function typical for comets at  $670 \pm 50nm$ . (Levasseur-Regourd & Hadamcik, 2003). The upper curve represents comets West, Halley, Bradfield and Levy. The lower curve represents comets Okasaki-Levy-Rudenko and Austin.

However it can be seen in Fig. 3.7b that the polarization function for the fosterite particles is not smooth. In addition, the phase angle resolution is  $3^\circ$  and data for  $\theta = 0^\circ$  and  $\theta = 180^\circ$  is missing. Therefore it was decided to generate a similar phase function using Excel by fitting a fourth order polynomial through the data. As can be seen in Fig. 3.8 that the highest polarization degree for cometary dust is obtained for  $\theta \approx 90^\circ$ , so the peak of fosterite particles that originally is at  $\theta = 100^\circ$  is shifted using the Excel approximation.

The  $F_{11}$ ,  $F_{22}$ ,  $F_{33}$  and  $F_{44}$  functions of the fosterite samples all have virtually the same values but also lack data at exact forward and backwards scattering directions. Therefore it was decided to adopt  $F_{11}$  results from a Mie-code calculation for a particle with  $r_{eff} = 1.3\mu m$  and a refractive index 1.63. Although Mie-calculations are only valid for spherical particles, the resulting forward scattering peak mainly depends on the particle size and not on the shape. Therefore the results can be adapted in this case.

The results of the data fitting can be found in Fig. 3.9. It can be seen that by using the Mie-code fitting the forward scattering peak of the  $F_{11}$ ,  $F_{22}$ ,  $F_{33}$  and  $F_{44}$  functions has been shifted to the right, meaning the approximation shows less strong forward scattering than the fosterite samples.

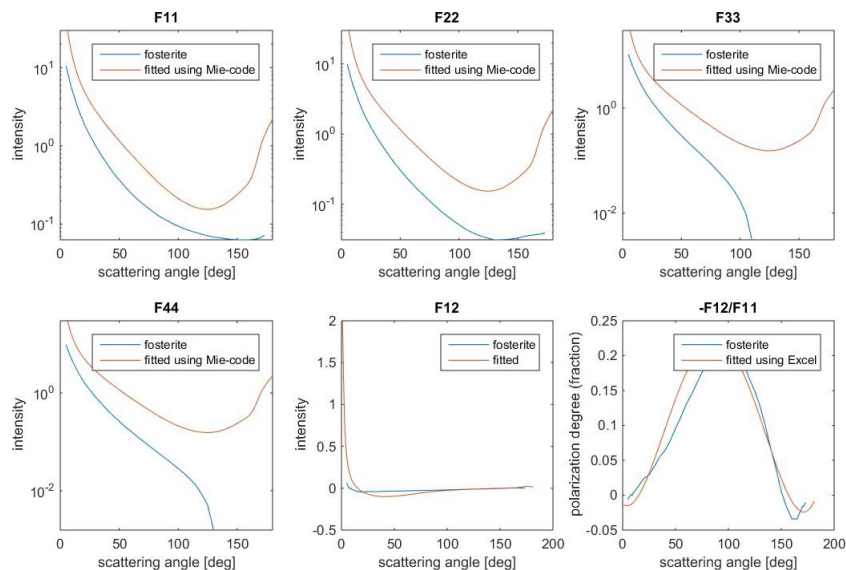


Figure 3.9: Comparison of the fosterite scattering functions and the fitting

## Albedo

The albedo of the dust is of importance as it determines what fraction of the light is absorbed and what fraction is scattered. Hence a collision event means either absorption (and re-emission at another wavelength) or a scattering at the same frequency.

From literature it is concluded that the albedo of the zodiacal dust is low and  $\simeq 0.1$ . Artymowicz (1997) suggests that 0.1 is a normal value for bodies like comets, for the dust of comet Halley, asteroids of class C, B and G, carbonaceous chondrites and the rings of Uranus. Levasseur-Regourd (1998) mentions that the albedo differs across the zodiacal dust disk, what could be caused by different mineralogy or processes that cause the structure or composition of the particles to change as they travel inwards to the Sun. It is reported that at 1AU the albedo is  $0.15 \pm 0.08$  in VIS. For the COBE mission (Kelsall, 1998) an albedo of 0.205 was found to match observations at a wavelength of  $1.25\mu m$ .

Based on the abovementioned findings it was concluded that for modelling purposes of the zodiacal disk three different albedos are of interest: 0.07 for the lower limit, an average of 0.15 and 0.23 as a higher limit.

### 3.2.4. Reconstruction of $\beta$ Pictoris dust scattering functions

As no specific information on the scattering functions of dust particles in  $\beta$  Pictoris was found, the scattering functions used for the Solar System are used for this disk as well.

The albedo of dust in the debris disk is however higher than that in the Solar System. Artymowicz (1997) reports that the albedo is  $0.5 \pm 0.2$ . This is supported by the simulated absorption and scattering cross sections of Nakamura (1998) (see Fig 3.10). The average albedo  $A$  depends on the scattering cross-section  $Q_{sca}$  and the absorption cross-section  $Q_{abs}$  as follows:

$$A = \frac{Q_{sca}}{Q_{sca} + Q_{abs}} \quad (3.10)$$

It can be seen in Fig. 3.10 that in VIS  $Q_{sca} \approx Q_{abs}$  and hence the assumption that  $A \approx 0.5$  is correct. This value shall be used for the dust in the disk surrounding  $\beta$  Pic.

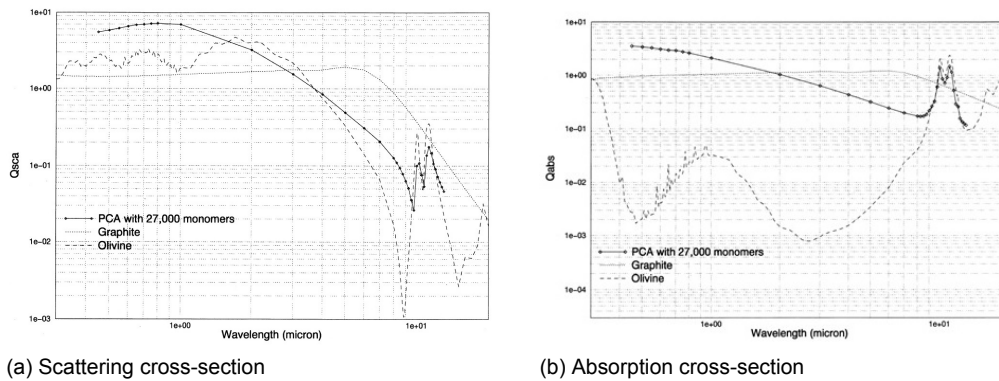
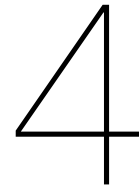


Figure 3.10: Scattering and absorption cross-sections of PCA simulated dust particles consisting out of 27,000 monomers (Nakamura, 1998).





# Multiple scattering: the zodiacal dust polarization evaluation code

Now that an overview has been given of the basic theory of light scattering by dust particles, the computational code that has been developed can be discussed. The Zodiacal dust Polarization Evaluation Code (ZPEC) allows the evaluation of polarization properties of unpolarized incident starlight that is scattered by zodiacal dust. It tracks the paths of the individual photons and simulates the scattering process and the corresponding properties of the photon that change upon every scattering event or encounter with a dust particle. The objective of this Monte-Carlo (MC) based code is to obtain the mean properties of the scattered light by the evaluation of a large amount of photons for which the scattering direction is determined by statistics.

ZPEC has been developed from scratch during the thesis work. Its development started with the evaluation of single scattered photons that were transmitted through a small volume element. This basic piece of code was developed further to include multiple scattered photons, as well as propagation of the photons through multiple volume elements and corrections for transformation of the Stokes vector in the scattering plane.

Although the basics of MC evaluation of photons transmitted by a medium are described in literature, it is not straightforward how to incorporate this in a computational code that allows to analyze a large amount of photons scattered by zodiacal dust. During the development of the code the main challenges were to keep track of the photon properties and to manage a huge amount of data. Creativity was needed to solve these problems and to answer questions like 'Where does the photon leave a volume element after it has been scattered?' and 'How can it be determined how often a photon is scattered within a volume element?'. During the development it was further found out that running the code was computationally extremely demanding. Thus major improvements were made to reduce computation time, which was finally reduced with 97% with respect to the initial code.

As the development of ZPEC has been major part of the thesis work the final lay-out of the code shall be explained thoroughly in this chapter. Also the verification results of the code shall be explained.

## 4.1. ZPEC main simulator structure

The main task of ZPEC is to propagate photons through a reference volume (consisting of multiple grid cells) and evaluate what properties these photons obtain upon scattering. A functional flow diagram of ZPEC is given in Fig. 4.1. In this functional flow diagram the dark blue boxes represent a part of the code in which calculations are made. As these together form the basics of the code these shall be elaborated upon in the next section. However a short summary shall be given first, to give the reader an idea of the complete code before more details shall be discussed.

- The first step is the initialization of ZPEC. During this step data on the dust particles is loaded (optical thickness per volume element, total number of particles to be propagated, dust optical

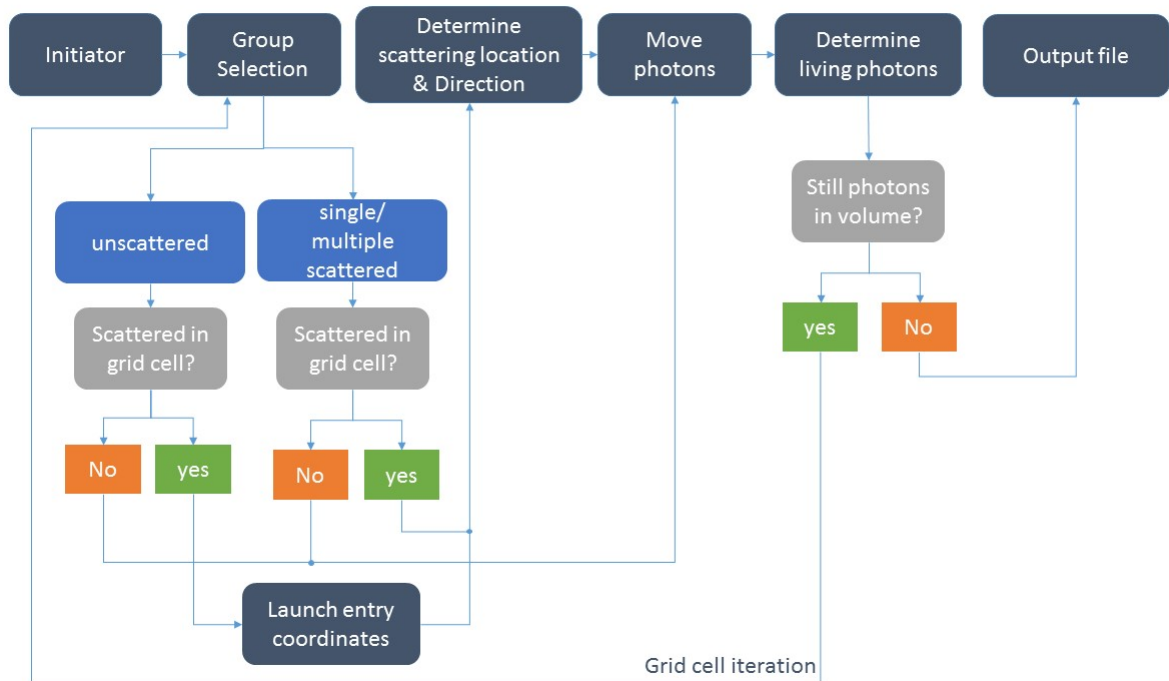


Figure 4.1: Functional flow diagram of the ZPEC main code

properties). A first grid cell to start the photon propagation is chosen.

- The photons arriving in the grid cell are either undisturbed or disturbed. The latter group comprises of singly scattered photons and photons scattered multiple times. Depending on what particles are in the grid cell, ZPEC follows a different procedure.
  1. For the undisturbed photons it is determined what fraction is scattered in the current grid cell. The part of photons that is not scattered in the grid cell is moved undisturbed and leaves the current grid cell. From the fraction that is disturbed, first the entry coordinates are computed, then it is determined where in the grid cell the photons are scattered and in what direction. Only after this the photons are moved throughout the cell.
  2. Also from the group of disturbed photons it is determined what part will be scattered in the current grid cell. However the initial coordinates do not need to be computed and the code immediately starts evaluating the location and direction of scattering. The part that is not scattered is moved undisturbed throughout the cell.
- If the photons are moved throughout the cell, it is determined in which directions the photons travel: if they are moving to other grid cells (and if yes, to what grid cells) or if they are leaving the dust disk. If there are still photons left in the dust disk, ZPEC keeps iterating over the grid cells until there are no photons left. Then an output file is generated with the properties of the scattered photons.

As this short summary does not provide the reader with deep insight in the structure of the code (why the code was structured like this), all the individual parts of the code shall be elaborated upon in the coming section. This overview serves as a reference throughout this detailed discussion.

## 4.2. ZPEC algorithm

In order for ZPEC to follow the individual photons to determine their properties upon scattering, several steps have to be taken. During these steps it is determined what part of the photons is scattered and in what direction they are scattered. Upon every scattering the scattered Stokes vector is calculated

and stored. This section shall be structured in correspondence with the functional flow diagram shown in Fig. 4.1, starting with the initialization of the code.

### 4.2.1. Initialization

In order to initialize ZPEC several inputs are necessary;

- A spherical reference volume with grid cells. The spherical reference volume is defined by a minimum radius (in AU), a maximum radius and azimuthal and elevational span which is by default from  $[0, 360^\circ]$  for the azimuth and  $[-90, 90^\circ]$  for the elevation as shown in Fig. 4.2a. The amount of grid cells in the three directions (radius, azimuth and elevation) is determined by the radial span  $\Delta R$ , azimuthal span  $\Delta az$  and an elevational span  $\Delta el$  of the individual grid cell as shown in Fig. 4.2b. It is assumed that dust is only located inside the reference grid and for every grid cell an average density is assumed. The different grid cells can have a different optical density. Hence the amount of grid cells determines the level of cloud detail that can be retrieved.
- A dust optical density model. The dust density model may be with high level of detail, but ZPEC works with an average value for each grid cell. The optical density in a grid cell determines the average path of a photon, see section 4.2.2. The dust optical density models for the Solar System and the dust disk orbiting  $\beta$  Pic were discussed in Chapter. 2.
- Scattering functions and albedo. As explained in section 3.1.2, the scattering functions are necessary to obtain the Stokes vector upon each scattering, which is used to determine the polarization degree of the scattered light. The albedo of the dust particles determines what part of the light is absorbed and what part of the light is reflected by the dust particles. The albedo and scattering functions for (exo)zodiacal dust were given in Section 3.2.3 and 3.2.4
- Number of photons to be propagated. The higher the number of photons propagated, the better the signal to noise level of the simulated detector view.

The code keeps propagating the photon paths through the individual cells until all the photons have left the complete reference grid.

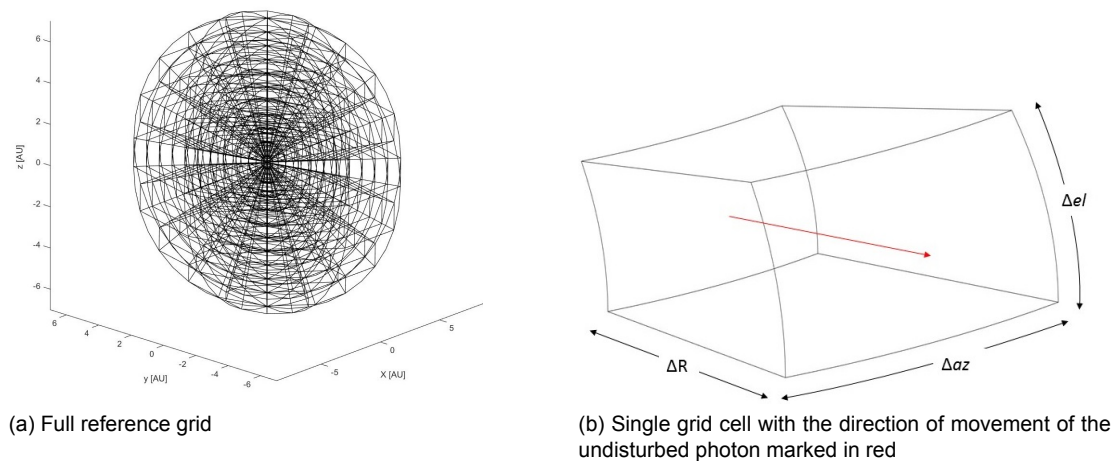


Figure 4.2: Spherical reference volume with grid cells that is used in ZPEC

### 4.2.2. Group Selection

To minimize computation time, there are two groups of photons considered within ZPEC that are treated separately. The first group of photons has not been scattered before and is hence labelled as 'undisturbed'. For this group it is only important to save its size/the amount of photons in this group while the photons travel through the individual grid cells. It is important to save the size of this group, as this number is necessary to determine how many particles shall be scattered within the grid cells. The properties of these photons are only initiated once they are scattered. This immediately shows why this reduces computation time; as this group is generally very large (for low cloud optical thickness) it avoids that the computer has to save large property matrices in its working space (that mainly contains zeros).

It is assumed that the undisturbed photons travel radially outwards, such that the distance they traverse in a grid cell equals  $\Delta R$ . This is however not a requirement for ZPEC to analyze the scattering direction of photons, but it increases the efficiency and hence decreases the computation time. The undisturbed photons enter at the back panel, the direction of movement is indicated in Fig. 4.2b. The second group is comprised of photons that have been scattered before and hence the group is labelled as 'disturbed'. When ZPEC is launched, the group of disturbed photons is empty, but typically this group grows throughout the simulation. From this group of photons the Stokes vector is stored as well as the direction of propagation (defined by two angles, see Fig 4.3), the location of where the photon leaves the grid cell (in spherical coordinates) and a reference number indicating which side the photon leaves the grid cell (either top, bottom, left, right, front or back panel).

#### Single scattering

When an undisturbed photon meets a dust particle within the grid cell, the group of undisturbed photons loses a photon and the group of disturbed photon gains one. The individual photon shall now be singly scattered. In order to determine the number of singly scattered photons the optical thickness is necessary. It is known that the flux  $F$  transmitted through a medium relates to the incoming flux  $F_0$  as described in Eq. 4.1;

$$F = F_0 e^{-\tau} \quad (4.1)$$

In which  $\tau$  is the optical thickness along the path of the photons. This means the fraction of photons transmitted through a ZPEC volume element can be expressed as in 4.2. The number of photons of the undisturbed group that is transmitted through the grid cell undisturbed can be expressed like in Eq. 4.3 where  $N_{u,e}$  is the number of undisturbed photons that enter the grid cell and  $N_{u,t}$  the number of undisturbed photons transmitted. Again, this number is important to save as it is an input to determine how many photons shall be scattered in the grid cells that are located radially outwards.

$$\frac{F}{F_0} = e^{-\tau} \quad (4.2)$$

$$N_{u,t} = N_{u,e} e^{-\tau} \quad (4.3)$$

As  $N_{u,t}$  is likely to be a decimal number it is floored down. The small error that is made by flooring down the decimal number is corrected for by applying a statistical analysis on a single photon. This determines if one photon should be added to  $N_{u,t}$ . For this photon the path length is calculated based on statistics;

$$\Delta x = \frac{1}{\tau} \ln \left( \frac{1}{p} \right) \quad (4.4)$$

In which  $p$  is a randomly drawn number between 0-1 (using MATLAB's default random generator *rand*). If  $\Delta x$  is larger than the thickness of the layer  $\Delta R$ , the photon is transmitted undisturbed. If  $\Delta x$  is smaller, it shall meet a dust particle within the grid cell and shall be marked as 'disturbed' and one photon is added to  $N_{u,t}$ .

### Multiple scattering

There is also a group of photons that enters the reference grid that have been scattered before. This group is comprised of photons that have already been scattered once or multiple times (single/multiple scattered). For this group it is also determined what photons shall be scattered again in the current grid cell. In order to do so, their undisturbed path is also calculated using Eq. 4.4. However now  $\Delta x$  is not compared against  $\Delta R$ , but with the length of the photon path if it were to travel undisturbed (not scattered in the current grid cell) through the grid cell. As these disturbed photons do not travel radially outwards and do not always enter the grid cell via the back panel as the undisturbed photons do, these distances vary.

Now a part of the scattered photons shall not be scattered again in the current grid cell. These photons shall leave the reference grid again without changing their photon property or direction of propagation. The part that is scattered is now always scattered multiple times. From this group the scattering location and direction is calculated and the Stokes vector updated.

#### 4.2.3. Launch of photon entry coordinates

When undisturbed photons are scattered in the grid cell (the single scattered photons), their entry coordinates are simulated using the random generator. It means that the location of where the photon enters the grid cell can be launched in the first grid cell, but also in grid cells crossed upon at later stages of the simulation. Hence if it is determined that a certain photon is scattered in the fourth grid cell, its entry location is generated for the fourth grid cell. This ensures that the matrix with properties of scattered photons only grows when photons are actually scattered.

The generation of these coordinates is not straightforward and this process requires a normalization. The photons should enter the reference volume at a random location equally spread over the entry surface (one of the sides of the grid cell). However towards the poles the surface of the sphere decreases in comparison to the equator. Hence if the entry locations are equally spread over a certain latitudinal range, the surface density of the entry coordinates is higher at the poles than at the equator.

Of course this is inconvenient and therefore a normalization is applied to ensure an evenly distribution of photons over the surface. To do so 500 elevation bins are made and for each of the bins the surface area  $A$  is calculated (assuming  $R = 1$ ). (For the reader that does not immediately understand what is meant by an elevation bin: imagine cutting an orange in 500 thin slices, not wedges, and calculating the surface of the colored peel for each slice.) Assume the individual bins extend from  $el$  to  $el + \Delta el$  then this area can be calculated as;

$$A = 2\pi [\cos(el + \Delta el) - \cos(el)] \quad (4.5)$$

Now these areas are used to normalize the amount of photons within the bin, i.e. if the surface of bin 1 is twice as large as that of bin 2, bin 1 shall yield twice as much photons. Within the bin itself the azimuth and elevation coordinates are generated using Eq. 4.6 with  $p_1$  and  $p_2$  two randomly drawn numbers between on the interval (0,1) with a uniform distribution;

$$\begin{aligned} az_0 &= az + p_1 \Delta az \\ el_0 &= el + p_2 \Delta el \end{aligned} \quad (4.6)$$

Once the initial coordinates of a photon have been generated, their movement of propagation is described by two angles: elevation  $e$  and azimuth  $a$  which is visualized in Fig. 4.3. These angles are expressed in the local photon reference frame which has the same orientation as the heliocentric reference frame but has its origin in the photon itself.

The initial coordinates only need to be determined for the undisturbed photons that shall be scattered in the grid cell. This means that upon initialization the photons still travel radially outwards and that their direction of movement can be expressed by the azimuth and elevation of their location, thus  $e = el$  and  $a = az$ .

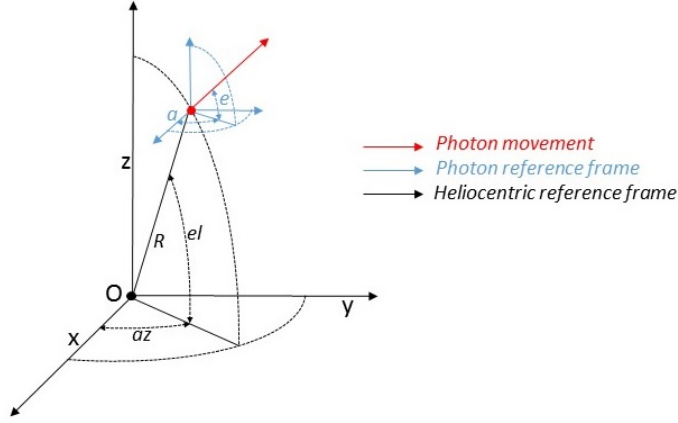


Figure 4.3: Visualization of the photon coordinates and photon movement in the heliocentric reference frame. The location of the photon is expressed by spherical coordinates in the heliocentric reference frame. The direction of movement of the photon is defined in the local photon reference frame that has the same orientation as the heliocentric reference frame but has its origin at the location of the photon.

#### 4.2.4. Scattering of the photon

When the photon meets a dust particle several steps follow in order to determine in which direction it is scattered.

##### Rejection method for single scattering

In order to determine the direction of scattering the rejection method is used (e.g. Ramella-Roman, Prah & Jacques, 2005). This method is valid for all types of scattering (multiple and single), but can be simplified for single scattering.

The chance that a photon is scattered is a function of the scattering angle  $\theta$  and depends on the phase function  $F_{11}$  as follows;

$$P(\theta) = F_{11}(\theta)I_0 \quad (4.7)$$

Now two random numbers are generated:  $P_{rand}$  is a randomly drawn number between  $0 - 1$  and  $\theta_{rand}$  is randomly drawn between  $0 - \pi$ . Now if  $P(\theta_{rand}) \leq P_{rand}$ , the angle  $\theta_{rand}$  is accepted as  $\theta$ . If not a set of two new random numbers is generated until the test is successful.

##### Rejection method for multiple scattering

In case a photon is scattered multiple times, the chance a photon is scattered does not only depend on the incoming flux  $I_0$  only, it also depends on the polarization state of the photon and thus on  $Q_0$  and  $U_0$ . The direction of movement after the scattering event is now determined by two angles: the scattering angle  $\theta$  and the azimuthal angle  $\Psi$  as is shown in Fig. 4.4. The probability function that determines the scattering direction  $P(\Psi, \theta)$  can be constructed using the scattering matrix and the rotation matrix (the need for rotation around angle  $\Psi$  shall be explained hereafter);

$$P(\Psi, \theta) = F_{11}(\theta)I_0 + F_{12}(\theta) [Q_0 \cos(2\Psi) + U_0 \sin(2\Psi)] \quad (4.8)$$

Now three random numbers are generated (instead of two for the single scattering case);  $P_{rand}$  is again randomly drawn number between  $0 - 1$ ,  $\theta_{rand}$  is again randomly drawn between  $0 - \pi$  and  $\Psi_{rand}$  is randomly drawn between  $0 - 2\pi$ . Now if  $P(\Psi_{rand}, \theta_{rand}) \leq P_{rand}$  the angles  $\Psi_{rand}$  and  $\theta_{rand}$  are accepted as  $\Psi$  and  $\theta$ . If not a set of three new random numbers is generated until the test is successful.

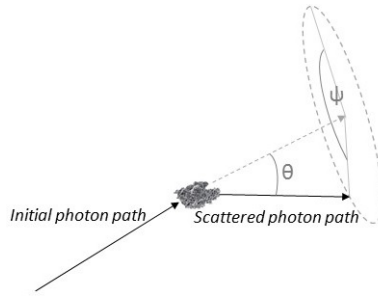


Figure 4.4: Scattering geometry. The direction of movement after scattering depends on the scattering angle  $\theta$  and an azimuthal angle  $\Psi$ .

### Stokes vector update

The polarization state of the photon and the direction of movement after scattering can be determined using three steps: two transformations and a multiplication with the scattering matrix. Fig. 4.5 shall be used to illustrate this.

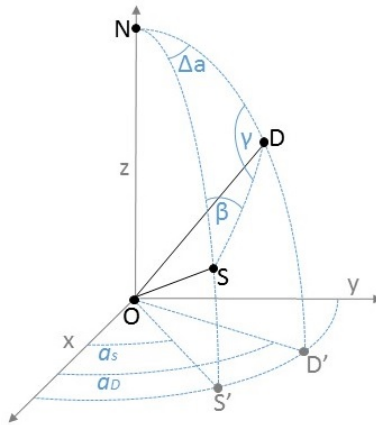


Figure 4.5: Geometry of the photon scattering

In Fig. 4.5 the line  $OD$  corresponds with initial photon path and line  $OS$  with the photon path after scattering. For clarity both vectors are plotted having the same origin. Point  $N$  corresponds with the local north, all vectors and points are shown on a unit sphere.

Now the scattering matrix is defined in the scattering plane, being the plane through  $ODS$ . However the Stokes vector shall be expressed on a common reference plane which is taken as the local meridian following the example of Hovenier & van der Mee, (1983), being the plane through  $ODN$ . Hence the first step is a rotation to align the common reference plane with the scattering plane. Using the definition as in (Hansen & Travis, 1974) the rotation angle should be taken positive rotating counter clockwise along the direction of propagation. Hence in this case a rotation is transformed over  $-\gamma$  using transformation matrix  $L(\gamma)$  ;

$$L(-\gamma) = \begin{bmatrix} 1 & 0 & 0 & 0 \\ 0 & \cos(2\gamma) & -\sin(2\gamma) & 0 \\ 0 & \sin(2\gamma) & \cos(2\gamma) & 0 \\ 0 & 0 & 0 & 1 \end{bmatrix} \quad (4.9)$$

In the case that  $a_D \geq a_S$  the angle  $\gamma$  equals the azimuthal angle of scattering  $\Psi$ .

The second step is to calculate the reflected Stokes vector in the scattering plane  $ODS$  using the scattering matrix  $F(\theta)$ ;

$$F(\theta) = \begin{bmatrix} F_{11}(\theta) & F_{12}(\theta) & 0 & 0 \\ F_{12}(\theta) & F_{22}(\theta) & 0 & 0 \\ 0 & 0 & F_{33}(\theta) & F_{34}(\theta) \\ 0 & 0 & F_{34}(\theta) & F_{44}(\theta) \end{bmatrix} \quad (4.10)$$

The third step is to rotate the Stokes vector that is now defined in the scattering plane to the local meridian at S. Now the rotation is around an angle  $+\beta$  that is yet still unknown. This angle can be calculated using the equations for the Side-Angle-Side problem as given by Wertz (2009), see Appendix A. The application of this problem to the rotation case also leads to the rotation angle  $\Delta a$ .

Now the rotation matrix  $L(\beta)$  can be constructed as shown in Eq. 4.11.

$$L(\beta) = \begin{bmatrix} 1 & 0 & 0 & 0 \\ 0 & \cos(2\beta) & \sin(2\beta) & 0 \\ 0 & -\sin(2\beta) & \cos(2\beta) & 0 \\ 0 & 0 & 0 & 1 \end{bmatrix} \quad (4.11)$$

Thus the scattered Stokes vector  $I_s$  can be written as a function of the incident Stokes vector  $I_0$  as follows;

$$\begin{bmatrix} I \\ Q \\ U \\ V \end{bmatrix}_{sc} = L(+\beta)F(\theta)L(-\gamma) \begin{bmatrix} I \\ Q \\ U \\ V \end{bmatrix}_0 \quad (4.12)$$

In the case that  $a_D \leq a_S$  the angle  $\gamma$  should not be taken equal to  $\Psi$ , but equal to  $\Psi - \pi$ . The rotation angle  $\beta$  can be taken in the same way but now the first rotation should be around  $+\gamma$  and the second rotation around  $-\beta$ .

### Absorption of a photon

Once a photon meets a dust particle it is either absorbed and radiated at another frequency or it is scattered at the same frequency. It means that when the photon properties are analyzed at a certain frequency, a part of the photons is 'lost' during absorption. In ZPEC this absorption is accounted for by using the dust albedo as a weighting factor for the Stokes vector and upon every scattering the Stokes vector is multiplied with the albedo. This way, photons are not lost during the simulation. Radiation of absorbed photons at a different frequency is not accounted for by ZPEC.

### 4.2.5. Moving the photon

After the scattering direction of a photon has been determined it can be moved through the grid cell. Depending on the type of scattering of the photon, the photon is moved through the reference grid using different strategies.

#### Undisturbed photons - not scattered

These photons have not been scattered before and are not disturbed in the grid cell. They enter the grid cell at the back panel and leave at the front panel. Solely the size of this group is stored and used as the size of the group that is passed on to the grid cell which faces the front panel.

#### Undisturbed photons - singly scattered

For each of the photons in the grid cell a random number is generated which yields  $\Delta X < \Delta R$ . Now the photon grid cell exit coordinates  $[az_2, el_2, R_2]$  are calculated using the photon entry coordinates  $[az_0, el_0, R_0]$ , the direction of movement of the photon  $(a, e)$  (see Fig. 4.3) and the number  $\Delta X$  and  $\Delta R$ . See Fig. 4.6 for an illustration of the relevant coordinates. First the spherical coordinates of

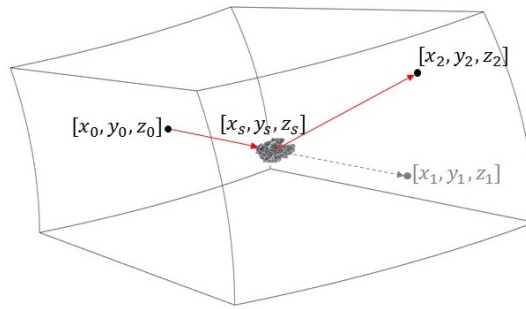


Figure 4.6: Coordinates of scattering

the grid entry location  $[az_0, el_0, R_0]$  are converted to Cartesian coordinates using Eq. B.1. Then the coordinates of the scattering location  $[x_s, y_s, z_s]$  are calculated with Eq. B.3.

Now that the coordinates of the scattering direction are known, the new propagation direction can be calculated using Eq. A.4. The new azimuthal direction  $a_s$  can be calculated as  $a - \Delta a$  if  $0 \leq \Psi \leq \pi$  and as  $a + \Delta a$  if  $\pi < \Psi < 2\pi$ . The new elevation direction  $e_s$  can be directly retrieved from Eq. A.4.

The exit coordinates of the photon are calculated using linear interpolation on the vector that describes the spherical coordinates of the scattered photon path, see Fig. 4.7. The photon path vector itself is made using a vector that extends from 0 to  $10\Delta R$  and has step size  $\frac{\Delta R}{10}$ , which is then used to calculate the spherical coordinates along this vector (together with the direction of propagation described by  $e_s$  and  $a_s$ ). This is converted to Cartesian coordinates, added up to  $[x_s, y_s, z_s]$  and converted back to spherical coordinates using Eq. B.2. It thus yields three vectors that are checked for the first element that is outside the grid boundaries. This point is then interpolated to yield the spherical coordinates of the grid cell exit location.

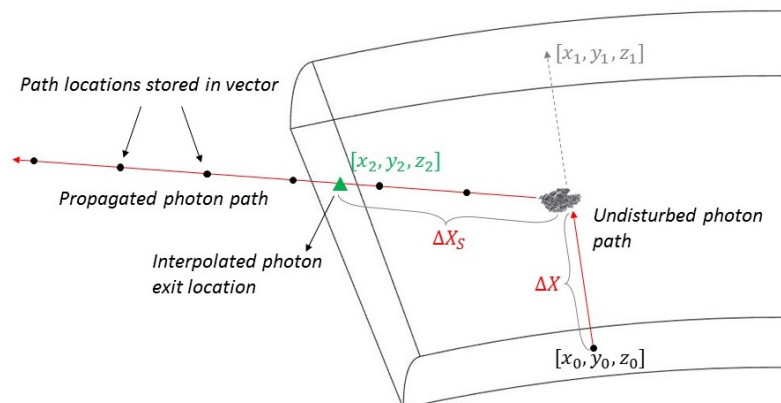


Figure 4.7: Illustration of the procedure to calculate the coordinates of scattering for an undisturbed photon

### Disturbed photons

Photons that have been disturbed earlier (either single or multiple scattered) can either travel in the grid cell undisturbed or disturbed. Using the same vector generation and interpolation as for the undisturbed photon that is singly scattered in the grid cell, the photon exit location can be calculated, see Fig. 4.8. However now the procedure is slightly different.

1. Using a generated vector the undisturbed distance  $\Delta X_D$  through the grid cell is calculated using Eq. 4.4. The random generator is used to calculate the actual length of the photon path  $\Delta X$  which is compared to the undisturbed distance  $\Delta X_D$ . If  $\Delta X > \Delta X_D$  then the photon shall not be disturbed in the grid cell.
2. If  $\Delta X < \Delta X_D$  the photon is scattered in the current grid cell. The photon path is interpolated to find the scattering coordinates  $[x_s, y_s, z_s]$ . The new photon propagation direction is calculated

using the rejection method and the equations for Side-Angle-Side spherical triangles. This photon path is then propagated to find the photon grid cell exit location.

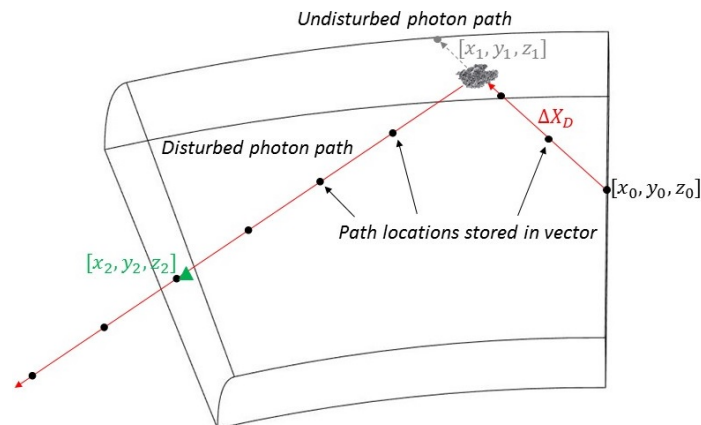


Figure 4.8: Illustration of the procedure to calculate the coordinates of scattering for a disturbed photon

For both the disturbed group and the group of photons that were undisturbed but are scattered in the grid cell, the grid cell boundary that is first crossed determines via which plane the photon is leaving. For an illustration thereof and the numbering that is used in the simulator, see Appendix B.4.

### Multiple scattering within a single grid cell

In the paragraphs above it is explained how the photons are propagated through their grid cells upon scattering as if they were scattered only once in their grid cell. However it must be noted that an algorithm was included in ZPEC that accounts for multiple scattering within the grid cell. This iterative algorithm calculates the photon path  $\Delta X_S$  from the scattering location to the exit location and using the random generator an undisturbed path length  $\Delta X$  is generated. If  $\Delta X > \Delta X_S$  the undisturbed path length is larger than the path length of the photon inside the grid cell and the iterative loop is exited. However if  $\Delta X < \Delta X_S$  it means that the undisturbed path is shorter than the path the photon traverses inside the grid cell and the photon is once more scattered inside the grid cell. A new direction of propagation is calculated and the Stokes vector is updated. This process keeps running until the photon has left the grid cell.

#### 4.2.6. Living photons

After the particles have been propagated through the individual grid cell, ZPEC determines the next cell for which it propagates the photon paths. It does so by determining the grid cell with the most photons entering it, this includes both unscattered and scattered photons. ZPEC keeps iterating over the grid cells until the reference grid is empty.

During this stage the 'lost' particles are accounted for, that are the particles that are scattered  $\geq 20$ . The properties of these particles are deleted. This is done to prevent the simulation time to go up as a result of particles being scattered back and forth in the reference volume, which drastically increases the computation time. For optically thick media a high number of scatterings may be expected, so this maximum number of scatterings can be adjusted.

#### 4.2.7. Outputs: database

ZPEC iterates over all the grid cells to propagate the photon paths until the photons have left the reference grid. For every grid cell ZPEC stores how much photons have been left undisturbed. Also ZPEC stores the properties of the photons in a 3D matrix: the rows correspond with the individual photons, the photon properties are stored in the columns and in the third dimension the photons are sorted for each grid cell. This allows to evaluate the photon paths and properties on each location inside

the reference grid. Hence for an observer located outside the dust disk the view can be evaluated, but also for an observer that is located inside the disk the view can be analyzed.

An example of the database output can be found in Fig. 4.9. To generate this image all locations of the scattered photons were plotted that are located at the outermost layer of the reference volume at 7AU. To generate this image a dust disk similar to that to the Solar System was used and a moderately forward scattering phase function. It can be seen that indeed the scattered photons are centered around the heliocentric equator as may be expected for a disk like structure.

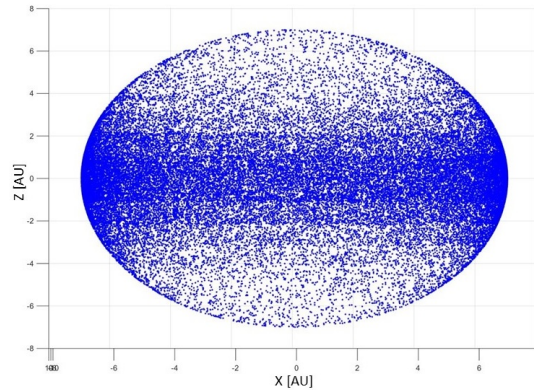


Figure 4.9: Output location of photons that were propagated through a complete spherical volume. The view is in the heliocentric plane and the sphere has a radius of 7AU. A forward scattering Henyey-Greenstein phase function ( $g=0.7$ ) was used for this simulation (Henyey & Greenstein, 1941). An accumulation is visible at the edges of the volume, which is a result of the MATLAB 3D plotting function. The dots represent all the photon output locations, also the ones that are located at the left, right and back of the sphere. As a result an accumulation is seen at the sides of the sphere.

### 4.3. Verification using the Adding-Doubling code

Results of ZPEC and a computational code that uses the adding-doubling method shall be compared in order to verify the ZPEC works correctly. First it is explained what reference case shall be used, secondly the results are given and a comparison is made.

#### 4.3.1. Reference case

The Adding-Doubling code (de Haan et al., 1987) calculates the flux travelling through a layer with finite thickness in z-direction, but which stretches to infinity in x and y direction (Fig. 4.10a). Within the layer photons are scattered in different directions, multiple scattering is accounted for.

This reference case is approached using part of a spherical volume at infinite distance from the origin. In this way, the curvature of the volume is virtually zero (Fig. 4.10b). In practise the volume cannot be located at infinity but is located at a large distance,  $R = 10^{10} AU$  (Fig. 4.10c). Both the azimuth and elevation range are chosen as  $0.0001^\circ$ , which makes the sides of the volume  $\simeq 1.7 \cdot 10^4 AU$  while the thickness of the volume is  $1 AU$ . The optical thickness is taken variable between  $1 AU^{-1}$  and  $5 AU^{-1}$ . Initially the albedo is taken 1 but later it shall be varied. Furthermore it is assumed that if a particle is scattered  $> 20$  times it is completely absorbed. For the phase functions the particles type A of de Rooij & van der Stap have been used (de Rooij & Van der Stap, 1984). These phase functions are valid for generalized homogeneous spherical particles with an effective size parameter of 2.628.

The polarization degree as calculated by the Adding-Doubling code is given as a function of scattering angle. In case of multiple scattering, this can be understood as the angle of the photon propagation direction with respect to the local normal. For all the photons transmitted by the volume (Fig. 4.10d) the scattering angle is retrieved (Fig. 4.10e). The properties of the photons are added for bins  $[0^\circ, 10^\circ)$ ,  $[10^\circ, 20^\circ)$  etc. and the polarization degree is calculated. As this will result in an average polarization degree for a bin it is expected that the results from ZPEC will differ slightly with the Adding-Doubling code, as the latter calculates the polarization degree for each scattering angle.

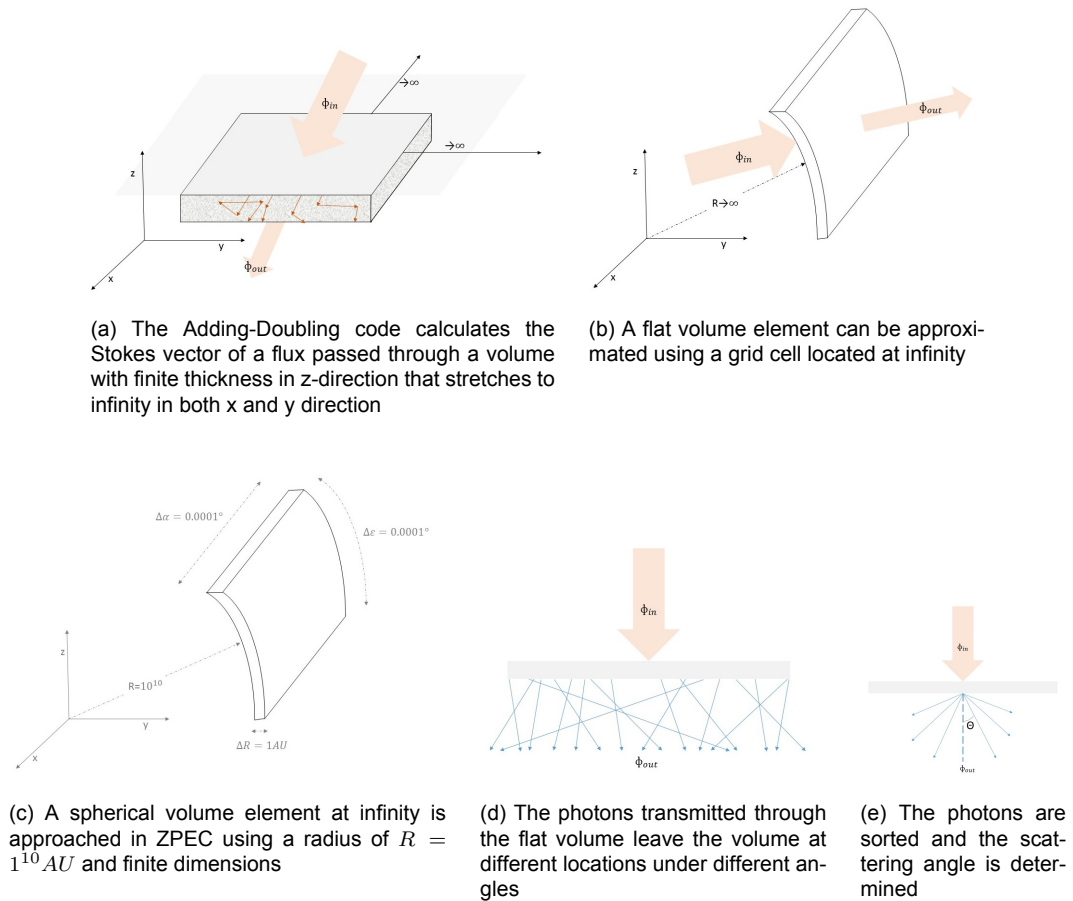


Figure 4.10: Geometries used for the verification case

### 4.3.2. Results and Discussion

A comparison of the Adding-Doubling code and ZPEC can be made when the photon properties computed with ZPEC are added for bins of  $10^\circ$  in width. For all the bins the intensities I, Q and U are added after which these are used to calculate the average polarization degree in the bins. This bin size is chosen such that the resulting graph is able to represent the general trend (hence the bins should not be too large) while still having enough datapoints in it to yield a representable average (hence the bins should not be too small). To generate the data presented in this section, ZPEC used  $10^6$  particles. The single order polarization degree (the degree of polarization of the particles that were only scattered once) is plotted separately from the total order polarization degree (polarization degree of all the scattered particles).

First let us examine the results for just one optical thickness, for  $\tau = 1 AU^{-1}$ . The results from both the Adding-Doubling code and from ZPEC can be found in Fig. 4.11. In addition, the individual datapoints for the single scattered photons are shown. It can be seen that although these datapoints exactly match the results for the Adding-Doubling code, the ZPEC single order line is slightly below the Adding-Doubling graph. This is an effect of averaging the data across the bins that are  $10^\circ$  in width. The difference is at maximum 0.21% (absolute) at a scattering angle of  $75^\circ$ . This effect is also present for the ZPEC total scattering order polarization graph. Unfortunately it cannot be checked directly how large the difference is due to averaging, as the multiple scattered datapoints do not follow the trendline: some photons have a higher polarization degree, some photons have a lower polarization degree.

The computed ZPEC linear polarization degrees for all the different optical thickness cases can be found in Fig. 4.12. There are a few things that should be discussed;

- The single scattering polarization degree line of ZPEC matches the result of the Adding-Doubling

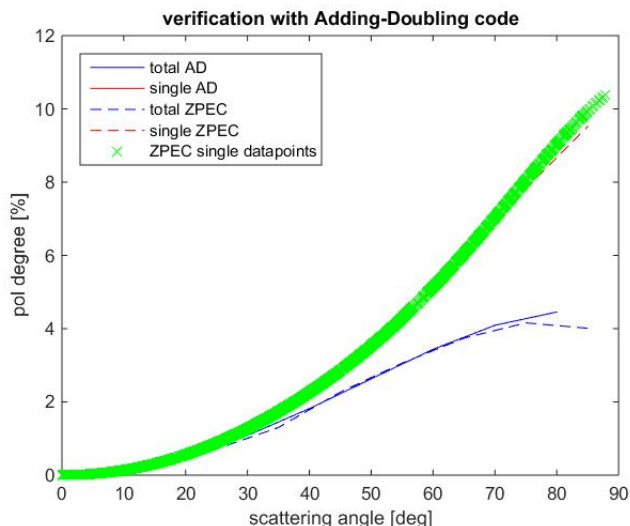


Figure 4.11: ZPEC polarization values compared to the Adding-Doubling code, showing the individual datapoints of the single order.  $\tau = 1[AU^{-1}]$

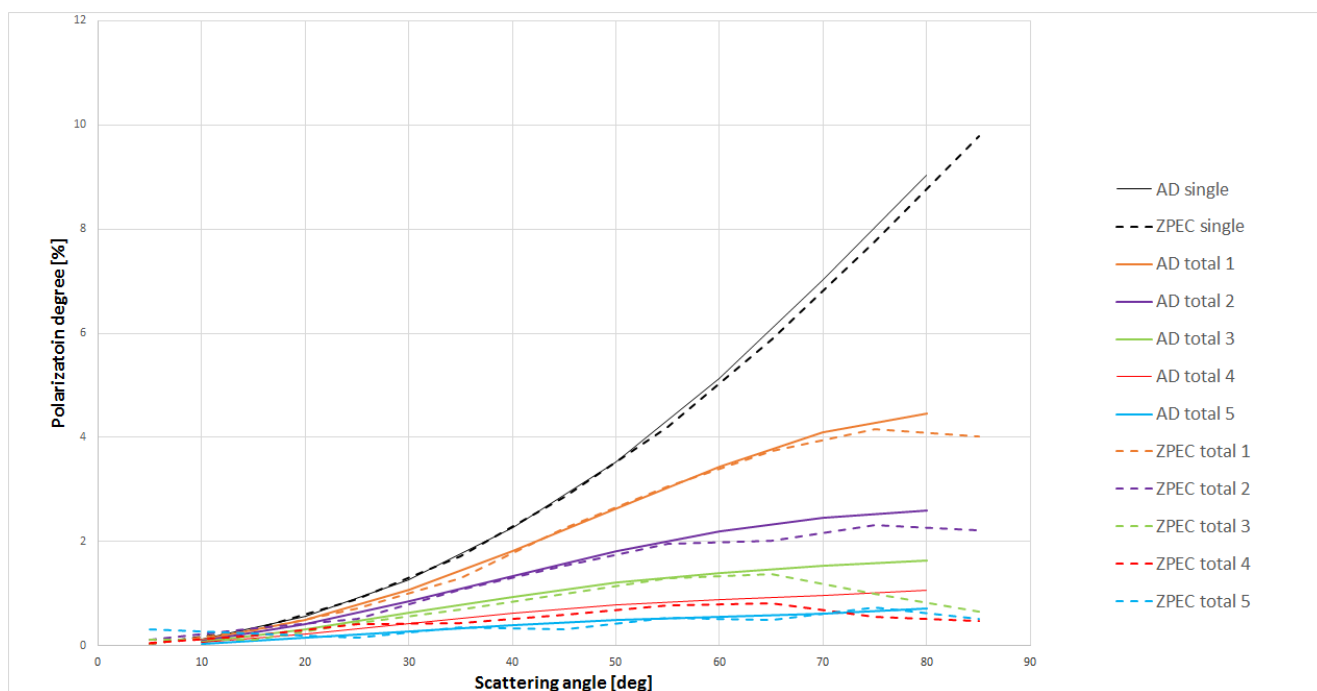


Figure 4.12: Verification of ZPEC with Adding-Doubling code. To generate these datasets the optical thickness of the layer was varied from  $\tau = 1, 2, \dots, 5AU^{-1}$  and the albedo of the particles was taken 1. The ZPEC dataset contains  $10^6$  particles but only the particles *transmitted* by the layer were selected. For the phase functions the particles of type A are used as described by de Rooij & van der Stap.

code very well. In the region  $< 60^\circ$  the difference is less than 0.06% and in the region above it is 0.18%. As discussed, this is the effect of bin averaging.

- It seems that for (almost all) graphs there are two regions visible: a region  $< 60^\circ$  for which the simulated graphs match the reference graphs quite well and a part  $> 60^\circ$  where the agreement is slightly worse. This is likely to be caused by the nature of the phase function that is used, which is strong in forward scattering. Hence, there are less particles scattered under larger angles and less particles leave the surface under an angle of  $> 60^\circ$ . As a result the averages in these bins

are subject of deviation.

- All the ZPEC lines representing the total order of polarization match the results of the AD-code the best for regions  $< 60^\circ$ . One exception is the line for  $\tau = 5AU^{-1}$ , which clearly does not follow the trend at small scattering angles. It is not known exactly what causes this deviation but it is clearly a result of the high optical thickness. It is possible that the high optical thickness causes the particle to scatter so often that there are less particles that leave the surface under small scattering angles which gives a deviation while calculating the average polarization degree in the bin.
- The differences between ZPEC and the adding-doubling code can be found in Table 4.1 for the two regimes. There is no clear relation between the error and the degree of polarization. In all cases the maximum deviation  $> 60^\circ$  is larger than for the regime  $< 60^\circ$  except for the case when  $\tau = 1AU^{-1}$ .

Table 4.1: Differences in degree of polarization between ZPEC and Adding-Doubling code (absolute). The optical thickness is given in  $[AU^{-1}]$

Case	Max deviation $< 60^\circ$ [%]	Max deviation $> 60^\circ$ [%]
Single scattering	0.06	0.21
Total order $\tau = 1$	0.07	0.50
Total order $\tau = 2$	0.08	0.42
Total order $\tau = 3$	0.01	0.63
Total order $\tau = 4$	0.11	0.55
Total order $\tau = 5$	0.19	0.02

### 4.3.3. Quantification of the Monte-Carlo effect

It is believed that the errors at large scattering angles ( $> 60^\circ$ ) for the total scattering order as shown in Fig. 4.12, are the result of the code being based on Monte-Carlo. The effect can be best described as a lack of particles at certain scattering angles, causing a difference between the calculated polarization degree and the actual one. To support this hypothesis an analysis is made in order to quantify this effect and to explain the origin of the errors better. The effect that is quantified in this section shall hereafter be indicated with *the MC-effect* for convenience.

As the scattering direction of a particle depends on its phase functions, the amount of particles found scattered at certain scattering angles also depends on these phase functions. It is therefore that the error differs for different particle types. Therefore the analysis is first made for the particles that were used for the verification case, then the same analysis is made for zodiacal dust particles in order to estimate the error that may be expected for the zodiacal cloud simulations.

#### MC effect for type A particles

To verify the polarization degree with the Adding-Doubling code, the average polarization degree is calculated for bins with a width of  $10^\circ$ , thereby referring to the verification case as described in Section 4.3.1. In Fig. 4.13 the amount of photons in the bins can be found, for the case when  $\tau = 5AU^{-1}$ . It can be seen that for small scattering angles and large scattering angles, the amount of photons in the bins is only 25% of the maximum. It means that the average value at these scattering angles has a larger variance than for the mid-range of scattering angles.

In order to quantify this effect the standard deviation of the polarization degree needs to be analyzed. To do so, the standard deviation of the mean polarization degree is calculated across the bins. The resulting  $1\sigma$  error represented by these values and shown in Fig. 4.14 can now be understood as the error due to the MC-effect or due to the variation in available datapoints for different scattering angles. The total error is only calculated for the total order polarization graphs, as it was shown earlier that the single order polarization data exactly matches with the Adding-Doubling code.

From this graph the following is clear:

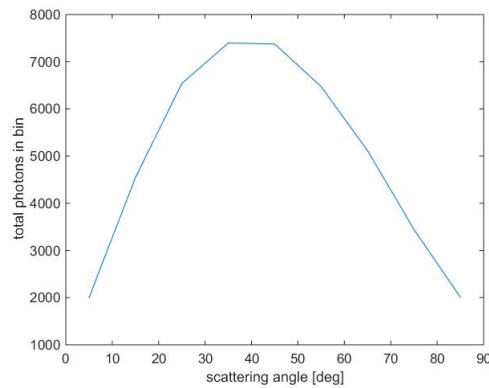


Figure 4.13: Amount of photons in the bins that are used to calculate the average polarization degree and that have been used to reconstruct the single scattering order and total scattering order polarization phase functions. This graph refers to the test case as described in Section 4.3.1,  $\tau = 5AU^{-1}$ .

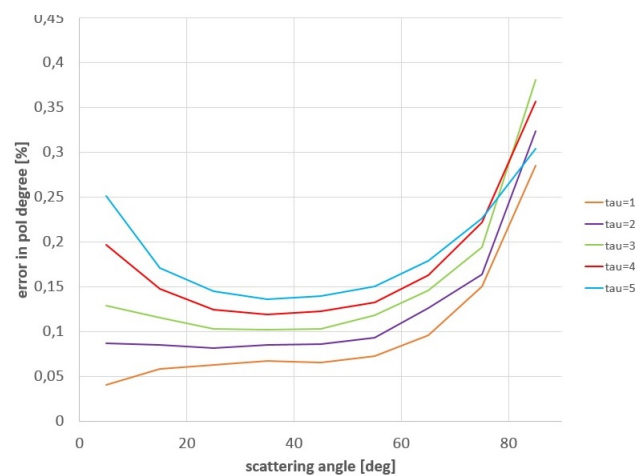


Figure 4.14:  $1\sigma$  absolute error as a result of the MC-effect

- As the optical thickness goes up, the minimum error increases. Also the relative error at small scattering angles increases.
- For low optical thicknesses  $\tau = 1AU^{-1}$  and  $\tau = 2AU^{-1}$  the error increases with increasing scattering angle. This corresponds with an average amount of scatterings of respectively 1.96, 3.42. As for the zodiacal cloud the average amount of scatterings might be expected to lie between 1 and 3, this trend can be expected for the zodiacal cloud as well.
- For higher optical thicknesses the error has a minimum at angles on the interval  $(30^\circ, 60^\circ)$ .
- The maximum error due to the MC effect is 0.38%.

Now the question arises whether the differences found in 4.12 can be fully explained by a lack of data at high scattering angles (or the so-called MC effect). This question is to be answered in order to exclude the influence of any other error sources. Now to answer this question the difference that is found in Fig 4.12 needs to be compared with the variance of the datapoints around the average, which shall give us the MC error.

The maximum found difference upon verification with the Adding-Doubling code is given in the second column of Table 4.2. As was shown earlier the found difference for the single scattering order was 0.21% due to bin averaging. This error can thus be treated as an error that shall be present for all the graphs. Subtracting this value from the found maximum verification differences (second column) gives an indication of the error that is caused by fluctuations around the trendline only. These values are called 'resulting observed MC difference' and can be found in the fourth column of Table 4.2. Now

the maximum MC error needs to be compared with these values, for clarity the maximum MC errors as found in Fig. 4.14, can be found in the last column. It can be found that in most cases the found difference falls within range of the  $1\sigma$  MC error. Only in the case  $\tau = 1AU^{-1}$  or  $\tau = 3AU^{-1}$  the found error is slightly higher than the  $1\sigma$  MC error.

Table 4.2: MC errors for single and total orders

Case	Maximum ZPEC& AD	deviation	Constant bin error	resulting MC difference	observed	MC error
Tot $\tau = 1$	0.50		0.21	0.29		0.28
Tot $\tau = 2$	0.42		0.21	0.21		0.32
Tot $\tau = 3$	0.63		0.21	0.42		0.38
Tot $\tau = 4$	0.55		0.21	0.34		0.35
Tot $\tau = 5$	0.02		0.21	0		0.30

So, the errors visible in Fig. 4.13 are in the same range as the expected error due to the MC-effect. Hence it can be concluded that the MC effect is the only error source that causes the differences visible in Fig.4.13. Of course an error that is significantly smaller than the MC effect can not be excluded based on this analysis.

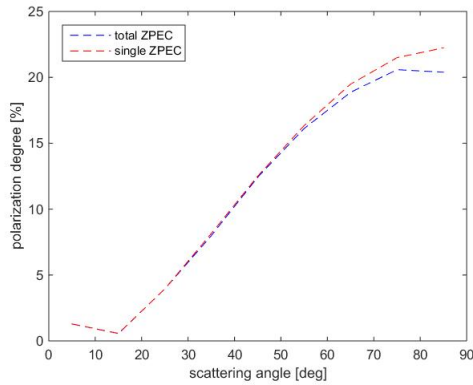
### MC effect for interplanetary dust particles

Although a quantification of the MC effect might seem nice, it is hard to generalize such a quantification and make it applicable to other cases. In the first place because the error is dependent on the total number of simulated photons: the more photons are used to generate the dataset, the lower the error for the average. Secondly the error depends on the phase functions which determine the statistics of the scattering direction and apparent scattering angle. For example; if instead of a forward scattering function an isotropic scatterer is used, the MC effect  $1\sigma$  error will show a more continuous behavior.

It is useful to analyze the effect of the MC effect using the phase functions that were established for zodiacal dust particles or the dust particles orbiting  $\beta$  Pic. For both types of dust particles the phase functions are identical and are based on those of small fosterite particles, see Section 3.2.3. From the results above it can be concluded that the MC error grows when the optical thickness increases. Hence the analysis should be performed using the maximum optical thickness in either the zodiacal cloud or the dust cloud in  $\beta$  Pictoris. The maximum optical thickness is found in the SMACK model for the  $\beta$  Pic dust disk and equals  $0.0437AU^{-1}$ . In order to make the result independent of the amount of photons in the bins, the error of the individual samples shall be presented rather than the error of the average (i.e. the standard deviation of the polarization values of the photons in a particular bin is calculated rather than the error averaged over this bin).

Using a total amount of photons of  $10^7$  and an optical thickness of  $0.0437AU^{-1}$  again the single order and total order polarization degree are calculated, see Fig. 4.15a. It can be seen that the polarization degrees are very close to each other, which is the result of the average amount of scatterings being close to one (in fact it is 1.0394, only 3.5% of the photons is scattered multiple times). The standard deviation of the polarization values in the bins can be found in Fig. 4.15b. It can be seen that  $1\sigma$  error for the single order is maximum around  $35^\circ$  and equals 1.23%. As for the type A particles it is expected that the single scattering order of the individual data points are exact, thus this deviation shows the error due to choosing a bin width of  $10^\circ$ . The  $1\sigma$  error of the total order is also maximum around this scattering angle and equals 3.1%.

Now let us link these results to a hypothetical image of a zodiacal dust disk. Imagine that for the disk certain polarization behavior can be derived as a function of apparent scattering angle. Then the standard deviation of these samples shall be the highest in the region  $(15, 35^\circ)$  and equals 3.1%. However the deviation as a result of choosing a bin width of  $10^\circ$  is 1.23%. It means that the deviation due to the MC effect only (the green line in Fig. 4.15b) is expected to be 2.1% in that region. The deviation is the highest at high scattering angles and equals 2.6%. Now the standard deviation can be turned into an error using the total amount of samples in the reconstructed bins. When it is deemed relevant this error due to the MC effect can be calculated based on this figure.



(a) linear polarization degree

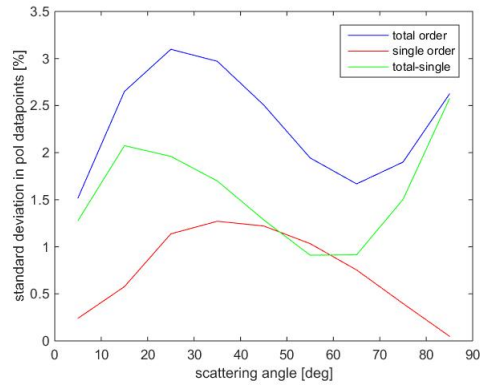
(b)  $1\sigma$  of polarization degrees

Figure 4.15: Supporting graphs for the MC error quantification analysis for interplanetary dust particles in a medium with optical thickness  $0.0437AU^{-1}$ .

#### 4.3.4. Testing with other albedo

The same approach was followed for a test but with the albedo of the particles set at 0.5, see Fig. 4.16. It can be seen in Fig. 4.16a for which a  $10^\circ$  bin with was used, that again ZPEC matches the Adding-Doubling code with a maximum error of 0.4% for angles  $< 40^\circ$ . The error grows for angles  $> 40^\circ$  to a maximum of 0.5%. As the offset for angles  $> 40^\circ$  seems constant and decreases at higher scattering angles the same plot was made but with a smaller bin width of  $5^\circ$ , see Fig. 4.16b. In this plot the deviations from the AD code are better visible. It seems that in the area  $50 - 70^\circ$  the polarization degree from ZPEC is too high on a structural basis. The deviations  $> 70^\circ$  are likely an effect of the few photons leaving the surface at higher scattering angles. As the single order polarization degree line matches the AD code very well (errors less than 0.05%) it is thought that the offset at medium angles is caused by the MC effect.

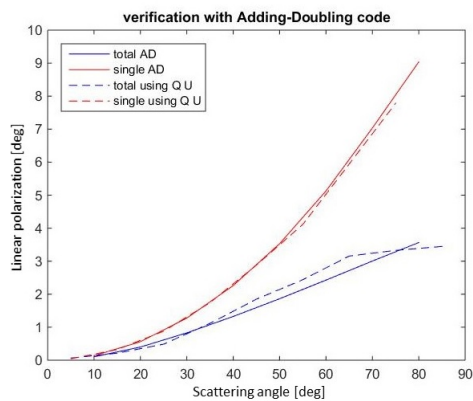
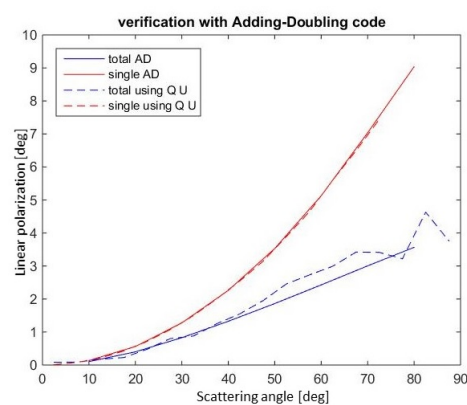
(a) Comparison with  $10^\circ$  bin width(b) Comparison with  $5^\circ$  bin width

Figure 4.16: Verification of ZPEC with Adding-Doubling code. The optical thickness of the layer was taken  $\tau = 5AU^{-1}$  and the albedo of the particles was taken 0.5. The total dataset comprises  $10^6$  particles but only the particles *transmitted* by the layer were selected. For the phase functions the particles type A are used as described by de Rooij & van der Stap.

#### 4.3.5. Testing with other phase functions

For further verification another test was performed but using another phase function as an input. Now the shape 5 particles of Moreno et al., (2006) are used, which are also a type of olivine particles. The results for a  $10^\circ$  bin width and a simulation over  $10^6$  particles can be found in Fig. 4.17, the albedo is

0.5. The single scattering polarization degree is structurally underestimated with 0.2 %, the error in the multiple scattering polarization degree is 0.25% angles <60%, and reaches a maximum of 0.55% for a maximum scattering angle of 80°.

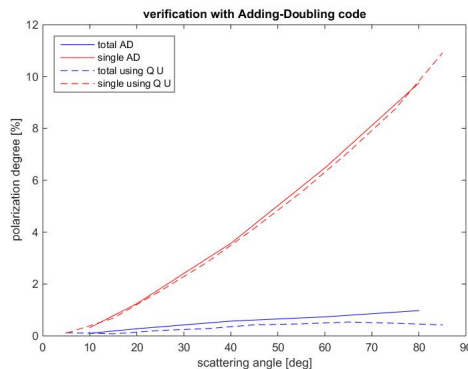


Figure 4.17: Verification of ZPEC with Adding-Doubling code. For this simulation phase functions of Moreno et al., type 5 particles were used that are valid for olivine particles. The optical thickness is taken  $5 AU^{-1}$  and the albedo of the particles is 0.5

### 4.3.6. The effect of taking the polarization state into account

ZPEC is a unique code as it not only allows to analyze multiple scattering in dust disks, but it also takes into account the polarization state of the incoming photons to determine the scattering direction. As the polarization state of the photon is sometimes neglected for particular research as mentioned by Hovenier & Muñoz (2009), it would be interesting to analyze the effect in taking/not taking the polarization state of the photon into account.

It was explained in Section 4.2.4 that the polarized fluxes  $Q_0$  and  $U_0$  are necessary to calculate the probability of scattering  $P$  for multiple scattering cases. This is taken into account by the rejection method, that is expressed in Eq. 4.8. However if these fluxes are not taken into account the equation reduces to  $P(\theta) = F_{11}(\theta)I_0$  and this may lead to a different set of adopted angles  $P(\Psi, \theta)$ . It means that if the polarization state of the photon is not taken into account to determine the scattering direction, the angles  $P(\Psi, \theta)$  are computed as if the photon were unscattered. This is no problem for single scattering as then the photons were unscattered (note that the rotation angle  $\Psi$  is hence not important for single scattering), however for multiple scattering this assumption may lead to errors. It immediately explains why the effect is only important for multiple scattering.

To analyze the effect again the flat layer reference case was used as was done for verification with the Adding-Doubling code. For the phase functions the Rayleigh scattering phase functions were used, for which the scattered intensity as function of phase angle is fairly homogeneous. This serves as an extreme case showing the largest deviations, as a Rayleigh scatterer shows very a very high polarization degree at scattering angle of 90°. Therefore, the effect of taking/not taking the polarization into account shall be larger than for a particle with lower polarized fluxes. The optical thickness was taken  $\tau = 5AU^{-1}$ . The results of the simulation can be found in 4.18.

There are a few phenomena found that need to be discussed. For convenience the case for which the polarization state of the photon is not taken into account is called 'without polarization case', for which the state is taken into account the case is called 'with polarization case'.

- First consider the single scattering order polarization degree. The single scattering degree of polarization of both cases should match as upon the first scattering, the incoming photons are unpolarized. This means that there should be no difference in the polarization degree for both cases. As can be seen in the upper left image, this is almost the case as the two blue lines almost match. Upon closer inspection (see left lower image for which the difference between the two is shown), it seems that the degree of polarization is very small for low scattering angles and is somewhat larger for higher scattering angles. However the error does not exceed 0.15%. The small difference is likely a result of the MC effect, as was also seen for the verification case with the Adding-Doubling code.

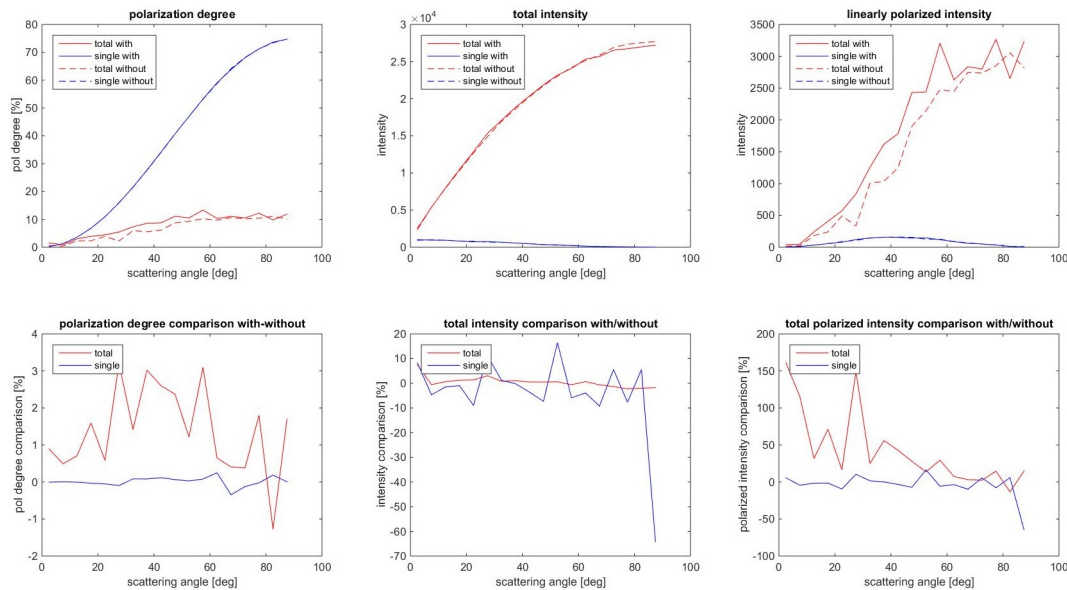


Figure 4.18: Comparison of scattering direction and polarization degree with and without the polarization state of the photon taken into account to determine the scattering direction. For this plot Rayleigh phase functions were used.

- The total intensity for the first and total order of scattering match well for lower scattering angles (middle upper and lower graphs). It can be seen that the percentual difference is higher for the single scattering order than for the total scattering order. However it is thought this is an effect from the low intensity for the single scattering order: if the total intensity is small, a small deviation results in a larger percentual difference. It can be seen that for the total scattering order the case with the polarization direction taken into account shows somewhat larger total intensity around scattering angles of  $20^\circ$  but the effect is negligible.
- The total linearly polarized intensity for the single scattering order (right upper and lower images) for both cases should match, again as the incoming Stokes vector is unpolarized. Therefore the difference between the two graphs can be treated as a 'noise' that is the result of the MC analysis. It can be seen that for the total scattering order the polarized intensity is much higher with the polarization taken into account than for the case without the polarization taken into account. The percentual difference shows fluctuations, but it is clear that a difference is present. Close to a scattering angle of  $0^\circ$  the total linearly polarized intensity is low and hence the percentual difference of  $\simeq 100\%$  doesn't tell anything about the effect of taking the polarization direction into account. Also, at high scattering angles no conclusions can be drawn on the effect as it was seen that the MC effect is present in this region. However it can be concluded that taking the polarization into account definitely increases the total linearly polarized intensity for the mid-region.

Summing up the effects it is expected that the polarization degree for the total order of scattering is at least higher for the mid-region of phase angles, comparing the 'with'-case with the 'without'-case. Indeed as can be seen in the graph in the lower left corner the polarization degree is  $\simeq 1.5\%$  higher in these mid-regions.

Now the same analysis can be done using the phase functions for zodiacal dust (see Section 3.2.3), for which the results can be found in Fig. 4.19. Again the functions show similar behavior as for Rayleigh scattering, however the effect of taking the polarization state of the photon into account is much smaller as the linearly polarized flux is lower. Instead of an isotropic scattering behavior these phase functions show a more forward scattering behavior. It can be seen from the total order polarization plot that there is not a clear difference between the two cases in the mid region. From the absolute difference plot (lower left) it can be seen that the difference is substantially for low phase angles, but it is uncertain whether this is caused by the difference in taking/not taking the polarization direction into account or whether this has another reason. At angles  $> 70^\circ$  the MC effect again comes into play and therefore

these results have to be interpreted with care. In the midregion the polarization degree is sometimes lower for the 'with' case than for the 'without' case, and is higher in the region  $40 - 70^\circ$ .

Thus it can be concluded that if these phase functions are used to analyze the polarization degree of a dust disk, and if the effect of taking/not taking the polarization state of the photon into account to determine the scattering direction, then it is expected that if a difference in polarization degree is found that this difference shall be at maximum 0.5% (as the optical thickness of the cloud shall be lower than  $\tau = 5AU^{-1}$ ) and the difference is likely to be visible in regions  $35 - 65^\circ$ . The effect on the total scattering order of the scattered intensity is negligible.

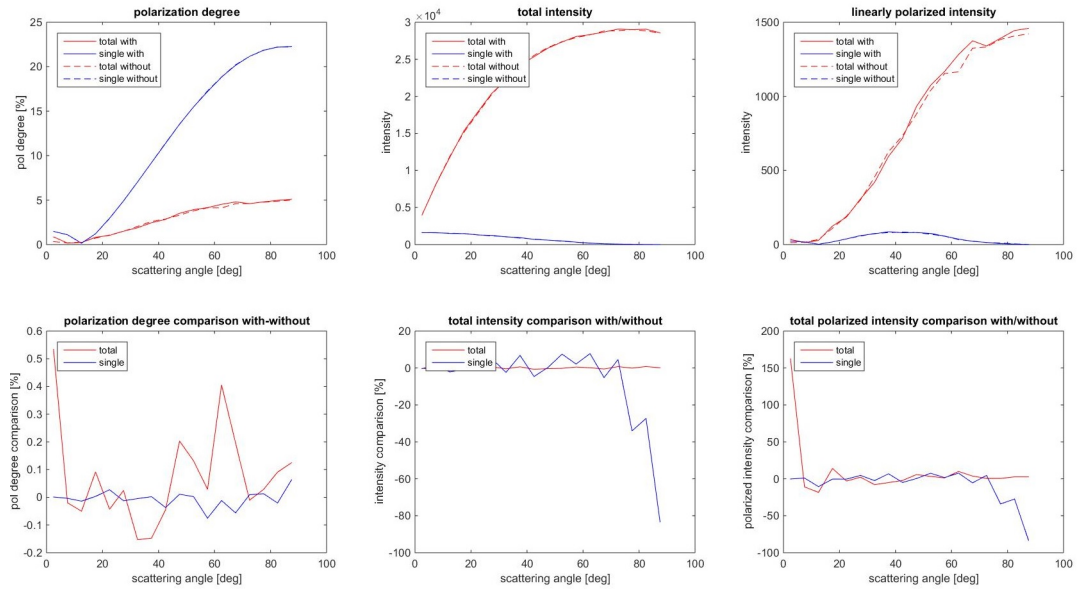


Figure 4.19: Comparison of total intensity and polarization degree with and without the polarization state of the photon taken into account to determine the scattering direction. For this plot the phase functions are used that approach the behavior of dust in the Solar System and dust in the disk surrounding  $\beta$  Pictoris, see section 3.2.3

# 5

## Results

Using the optical thickness models and particle phase functions as described in Chapter 2, ZPEC is used to compute intensity and polarization signals of dust disks. This chapter shall give the results of these simulations. First the results for the Solar System shall be discussed, then the results for the dust disk surrounding star  $\beta$  Pictoris shall be given.

The results presented in this chapter are generated assuming that only the scattered photons need to be considered and thus that the unscattered light of the star can be ignored. This is a valid assumption, as the unscattered photons representing the bright central star can and are often blocked out using a coronagraph in order not to saturate the detector.

### 5.1. Results for the dust disk in the Solar System

LOUPE's view of the Earth with the surrounding dust can be analyzed using ZPEC. With the propagator a coarse dataset is generated that contains the optical thickness of the smooth cloud and a detailed dataset is generated that contains the asteroidal bands and the Earth circumsolar ring, see Table 5.1 for inputs parameters and the total amount of photons used in the simulations. The contributions of both datasets can be added together if it is assumed that there is no interaction between the two datasets (i.e. the photons that have been scattered in the smooth cloud are not scattered in either the Earth circumsolar ring or the asteroidal rings and vice versa). As the zodiacal cloud is optically thin the effect of this assumption is minimal. To stitch the two datasets together, the results from the precise dataset are multiplied with the fraction of the total amount of photons simulated for the coarse dataset over the precise dataset.

It can be seen in Table 5.1 that there is a basic dataset and an extended dataset. The basic dataset was generated first, in order to check the difference of the detected brightness and polarization degree of the cloud at different wavelengths. It was the goal of the thesis to analyze the zodiacal cloud at different frequencies and as explained in Section 2.1.2 three wavelengths were chosen for comparison: 450nm, 650nm and 800nm. It was found out after the results for these three wavelength were compared, that the majority of the photons fall on the exact same spot on the detector surface. It was then realized that MATLAB starts at the same random generator 'seed' once it is started up, resulting in the same set of random numbers for each simulation. It results in datasets that are almost similar as the optical densities for the three frequencies differ only slightly. This was first seen as a problem, as the point of the MC simulation is doing a statistical analysis. However later this was considered as an advantage because now the differences for the three datasets are better visible. Therefore the basic datasets at different frequencies were used to analyze the effect of the wavelength on the detector views.

Unfortunately there were few photons detected, which lead to noisy images. Therefore a more extended dataset was generated that contains the properties of much more photons. As the generation of this dataset took several days it was only generated for a wavelength of 800nm. It shall be indicated when the extended or the basic dataset was used to generate the results.

Table 5.1: Inputs for the zodiacal dust precise and coarse datasets

	Precise Dataset	Coarse Dataset
$R_{min}$	0.303 AU	0.303 AU
$R_{max}$	5 AU	10 AU
bins azimuth	30	10
bins elevation	30	10
bins radius	10	10
total photons used, basic dataset	4.5e16	2.5e14
total photons used, extended dataset	1.8e17	7e14

Before the results are given, it shall be first explained how the observer view is obtained and how the planetary signal is included in the observer view.

### 5.1.1. Creating an Internal observer view

In case of LOUPE the detector view has to be created for a location of approximately 1AU (thereby neglecting the distance between the Earth and the Moon). The observer is located at  $0^\circ$  elevation and has a slight offset in azimuth direction, as the observer cannot be located exactly at the border of a grid cell. This means that it was assumed that the effect of the movement of the Moon around the Earth is not present for the detected photons and the location of the photons on the detector.

Instead of a conventional flat detector it was chosen to use a spherically shaped detector. It means that the detector view of LOUPE can be used to determine what LOUPE would see when it would view different parts of the sky. The spherically shaped detector is also useful to create a skyplot of the zodiacal light for an Earth-based observer. The detector hence shows the photons at apparent directions from  $(-\pi, \pi)$  in azimuth direction and in vertical (elevated) direction from  $(-\pi/2, \pi/2)$ . The center of the image corresponds with the vector Sun-observant.

The creation of the detector view consists of several steps that shall be discussed hereafter.

#### Selection of photons in observant grid cell

In order to select the correct set with data it is first determined in what grid cell the observer is located. The internal observant is defined as a point and hence it is not possible to locate the observer at the boundaries of the grid cell. Once this grid cell is known the correct data can be selected. In the ZPEC dataset the output locations of the photons are stored throughout their travel to the outer edges of the reference grid. It means that photons that have left the grid cell to the left of the observer at the right side plane, enter the observer grid cell at the left side. As such all the photons that might be in view of the observer can be selected.

#### Subject photons to angle constraint

Each photon that enters the observant grid cell has its direction of propagation specified. Now a vector is constructed that connects the observer and the location at which the photon enters the grid cell, see Fig. 5.1. The angle between this vector and the direction of propagation of the photon is subjected to the angle constraint: if this angle is small enough it is assumed that the photons can be detected by the observant and the photon is selected. This angle is set at  $10^\circ$  in case of LOUPE. Smaller angles are preferred but this also leads to a lower number of photons detected.

#### Locations of the photons on the detector view

To construct the detector image, the spherical coordinates of the input locations of the photons in the reference grid are used relative to the observer. The azimuth and elevation are given with respect to the heliocentric ecliptic, with the point  $(0^\circ, 0^\circ)$  towards the central star. Now the process to construct the detector view is as follows;

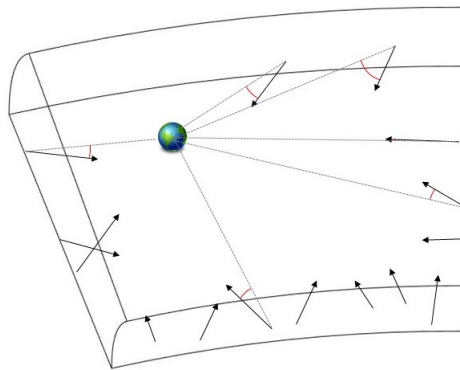


Figure 5.1: Illustration of the angle constraint for the observant located inside the reference grid. To select which photons are observed by the detector a vector is constructed that starts at the observant and ends at the location where the photon enters the reference grid. The angle with respect to the direction of propagation of the photon is subjected to the angle constraint and has to be smaller than a predefined value.

1. The detector has 200 pixels in horizontal and vertical direction, which are treated as bins. The photons are binned in these pixels according to where they fall on the detector. The coordinates of the photons are given in azimuth (corresponding to the horizontal bins) and elevation (corresponding to vertical bins). If it is determined in what bin the photon falls, the properties of these photons can be binned. Hence the net result of this process are two-dimensional matrices with photon properties.
2. The binned properties concern total intensity  $I$ , and linearly polarized intensities  $Q$  and  $U$ . The polarization degree is then calculated using these three matrices in which the horizontal bins correspond with the columns and the vertical bins with the rows.
3. The binned properties are plotted against their location in the sky given in azimuth and elevation. The point  $(0^\circ, 0^\circ)$  corresponds with the Sun.

### 5.1.2. Including Earth in the internal observer view

In order to simplify the calculations the Earth is included in ZPEC after the database has been generated. This means the properties of light scattered by Earth are calculated making use of the ZPEC databases rather than including Earth in the dust density model and use this as an input for the Monte-Carlo analysis. In this way, only the light scattered towards the observer is considered. However it therefore must be assumed that there is no interaction between the light scattered by the Earth and the zodiacal dust.

To generate images of the Earth with the dust at the background it is important that an internal view can also yield a planetary signal. In case LOUPE is considered, the instrument is located at the moon which orbits the Earth in an inclined plane. This means that the location of the Earth as seen from the moon varies throughout the year and the Earth is seen at different phase angles. The location of the Earth thus has to be determined as well as the phase angle under which it appears.

In the internal view the location of the Sun is always in the center and the locations of the detected photons are given in azimuth and elevation with respect to this vector. It is hence the purpose to calculate the location of the Earth with respect to the vector Moon-Sun such that its location can be shown in the same figures.

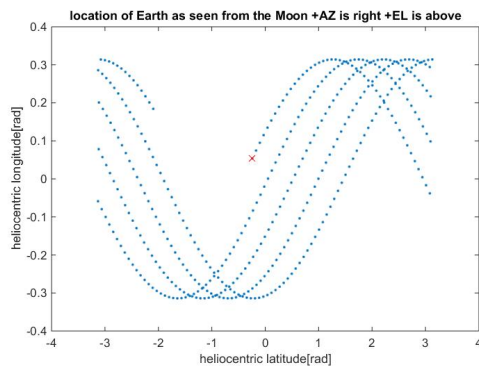
The orbit of the moon at different times of the year is shown in Fig. C.1 in Appendix C. In order to determine the location of the Earth and the Moon in heliocentric Cartesian coordinates first the Moon's orbit mean motion is calculated using Eq. C.1. Using the mean motion the true anomaly is calculated which, together with the kepler orbital parameters, can be used to determine the orbital radius. The orbital parameters are used to calculate the elements  $[l_1 \dots n_2]$  as shown in Eq. C.2 (Wertz, 2009). This is then used to calculate the Cartesian coordinates of the Moon and the Earth using Eq. C.3.

The calculations are performed for the Earth-Sun system, which yield the coordinates of the Earth

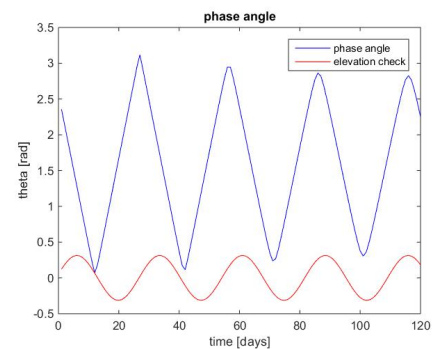
with respect to the Sun. The calculations are also performed for the Moon-Earth system that yield the coordinates of the Moon with respect to the Earth. Both coordinates are given as a function of time and can be converted to spherical coordinates, see Eq. C.4.

Now as the Earth is in the helioecliptic, the elevation of the Earth in the heliocentric frame is always zero. It means that the elevation of the Moon in the Earth-Moon reference system is the (negative) elevation of the Earth with respect to the Moon. Hence the first set of parameters can be set. The same relation applies to the azimuth angle, but the azimuth angle has to be corrected for the movement of the Earth around the Sun. This correction should be taken positive (the azimuth of the Earth in the Sun frame should be added), as the Earth rotates to the right for fixed azimuthal angles of the Moon with respect to the Earth, see Fig. C.1. Hence, the azimuth and elevation of the Earth as seen alongside the Moon-Sun vector can be expressed as in Eq. C.5.

Starting the simulation while the Moon is at a location indicated in Fig. C.1, the location of the Earth as seen alongside the Moon-Earth vector is shown in Fig. 5.2a.



(a) Location of the Earth seen alongside the Moon-Sun vector, which is in the point  $(0^\circ, 0^\circ)$ .



(b) phase angle over time

Figure 5.2: Location of the Earth with respect to the Moon-Earth vector and the corresponding scattering angles. Both results are a result of a 120 day simulation

The phase angle is calculated using the dot product of the vector Sun-Moon and Sun-Earth and is shown in Fig. 5.2b together with the apparent elevation of the Earth in the LOUPE view. It can be seen that the phase angle decreases slightly over the simulated period of time, which is caused by the inclination of the moon orbit. The orbital parameters that were used for this simulation can be found in Table C.1.

For the Earth a simplified set of equations was used for the phase functions (Fig. 5.3), and it is assumed that the flux signal is constant over the full observed disk. The phase functions are for a planet with a homogeneous black surface and a thick homogeneous atmosphere that only contains gas molecules. Rayleigh scattering was assumed to calculate the scattering behavior of these molecules. As the planet is homogeneous in horizontal direction  $U$  is zero with respect to the scattering plane (through the Sun, planet and observer) and therefore not shown in the figure. Of course this is a simplification of the real Earth, as the Earth is definitely not homogeneous. The functions were provided by the thesis supervisor.

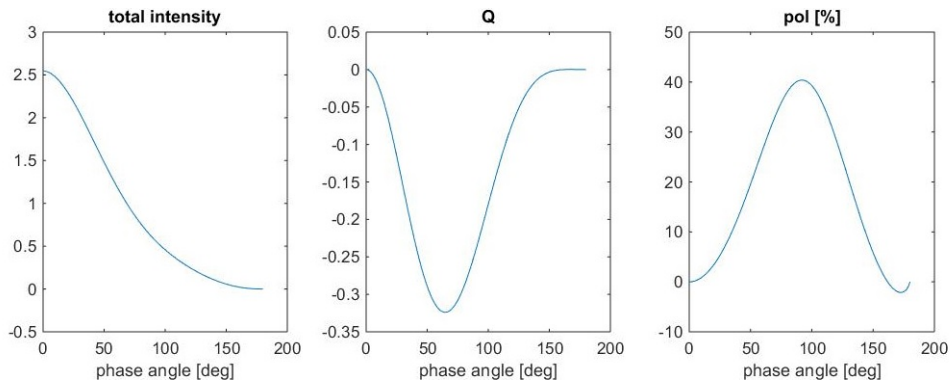


Figure 5.3: Phase functions of planet with black surface and a thick atmosphere that only contains gas molecules (Rayleigh scattering)

### 5.1.3. LOUPE view without the Earth simulated

The first result of ZPEC is a detector image that shows the polarization and flux signal of the zodiacal dust itself as seen from the moon. As it was decided to view the cloud at three different frequencies and as there are three different albedo that are to be used, two combinations are chosen: the one that sets the minimum signal and the one that sets the maximum. The minimal signal is obtained for a minimal optical thickness and albedo, hence at 450nm with an albedo of 0.07 for which the result can be found in Fig. 5.4. The maximum signal is obtained for the maximum optical thickness with the highest albedo, hence at 800nm with an albedo of 0.23, for which the result can be found in Fig. 5.5.

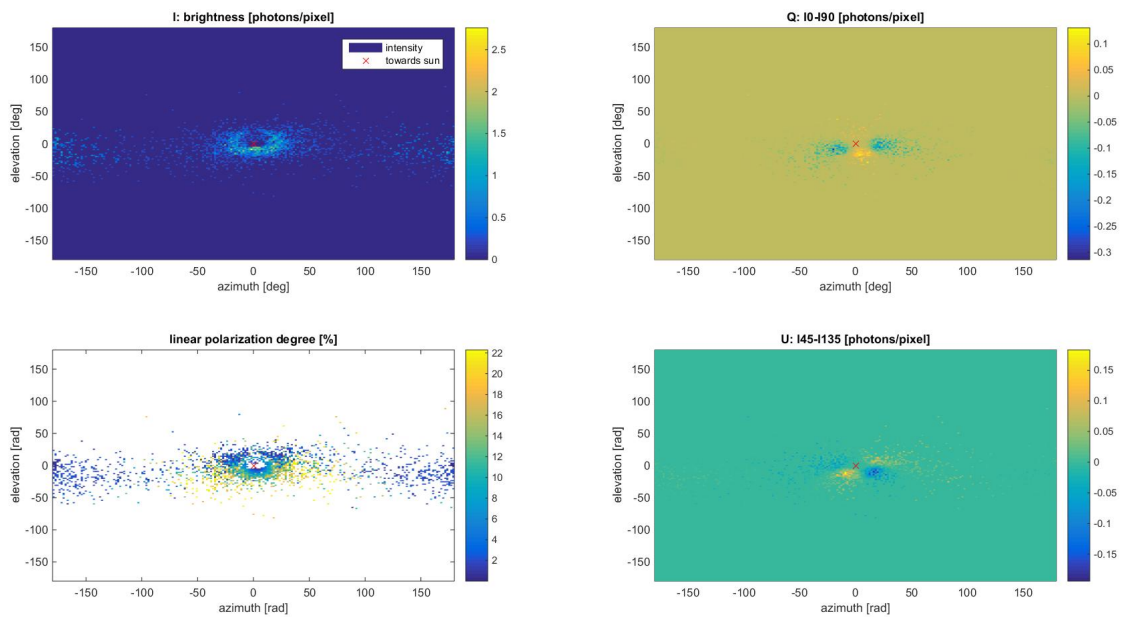


Figure 5.4: LOUPE view of the zodiacal cloud at 450nm with albedo of 0.07. To generate these views the basic datasets were used.

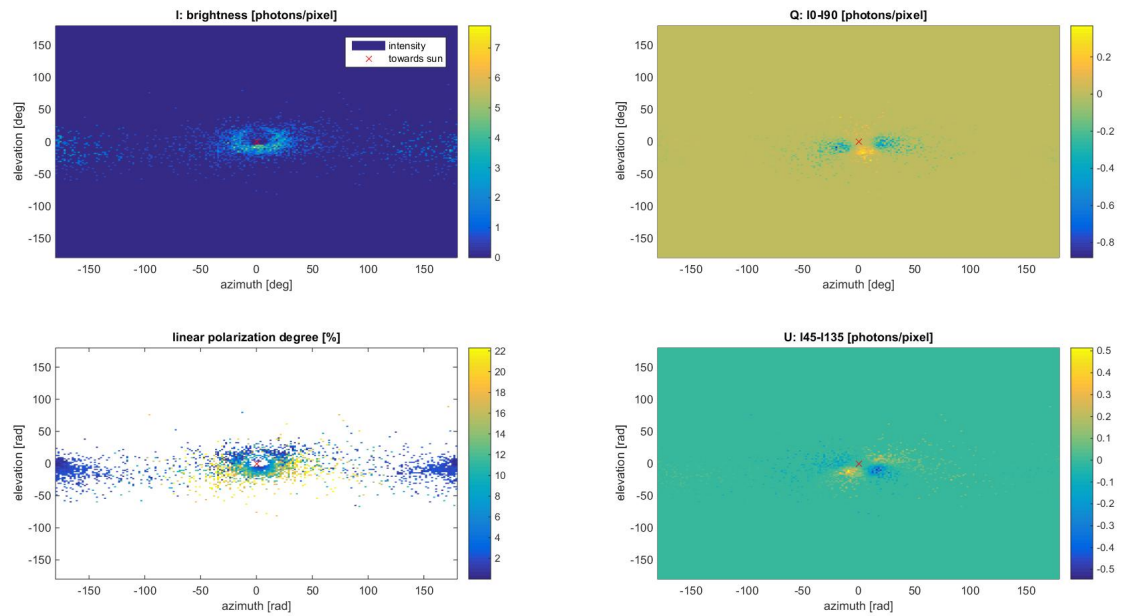


Figure 5.5: LOUPE view of the zodiacal cloud at 800nm with albedo of 0.23. To generate these views the basic datasets were used.

The first thing that needs to be discussed is the observed pattern that is found in these images.

- Close to the Sun, at  $(-50^\circ, 50^\circ)$  azimuth, there is an increased density of observed photons. This is the contribution of the smooth cloud and finds its origin in the scattering functions of the dust particles, which are strong in forward scattering directions.
- In the center of the image there is a cleared region, meaning that in this region no photons are detected. This is a striking result, as there are definitely dust particles between the Moon and the Sun that scatter the photons. It is however possible that this is the result of the relatively small distance between the cloud and the observant. If the particles are to travel in the direction of the observant they have to be scattered at extremely small angles to fall on the detector surface and as it is an MC code it is possible these small angles were not generated for these particles. It is however not certain this has caused the hole.
- The disk seems to be inclined with its right wing up, which is a result of the inclination of  $i = 2.03^\circ$  and the right ascension of ascending node of  $77^\circ$ . There is also another feature that can be explained with these two parameters, namely the ring of intensity around the Sun. The intensity of the photons detected seems to form a ring around the Sun, but this ring is less bright at the north side than at the south side. When the disk is inclined and has a positive right ascension, the observer at 1AU is actually looking to the disk a bit from above the tilted disk (i.e. if the location of the observer  $[X,Y,Z]=[1,0,0]$  is filled in in Eq. 2.2 then the found  $Z_c$  is positive hence the observed center is located above the midplane of the dust disk). It means that when looking to the Sun the cloud is more optically thick at the south than at the north, which results in more particles detected south from the Sun, leaving an apparent lower intensity region at the north. This also can be understand as the difference between forward and backward scattering: the south of the ring ring is seen in the more forward scattering region, the north in a more backwards scattering region.
- The center of the image is shifted with respect to the Sun and it seems that it is south from it, which corresponds with the negative offset in z-direction of the center of the disk with respect to the Sun. Hence this feature is as may be expected from the dust optical model as described in section 2.1.1.
- The center of the disk seems to lie a little bit to the right from the Sun, which corresponds with

the positive offset in Y-direction of the dust disk center with respect to the Sun. Hence this effect is as expected as well.

- At backwards scattering regions (close to  $-180^\circ$  azimuth and  $+180^\circ$ ) there also seems to be a high density region. These are photons scattered by the asteroidal ring. As this structure is not inclined with respect to the ecliptic, it results in a symmetric structure in horizontal direction.
- In between the forward and backwards scattering regions on the detector, photons are found that have been scattered by the smooth cloud and the Earth circumsolar ring. As the trailing and leading blobs that are found at the Earth circumsolar ring are located at approximately  $+90^\circ$  and  $-90^\circ$  it is expected that photons scattered by these dust structures show a polarization degree of  $\simeq 20\%$ , as for these phase angles the maximum polarization degree is reached. Photons detected in this region that have a lower polarization likely have been scattered at lower or higher phase angles before they were detected by the observer.
- The photons are primarily found around  $0^\circ$  elevation, meaning that the photons were primarily scattered in the helioecliptic plane. This matches the expectations as the dust disk is optically the thickest in this region. There are no or little photons detected in polar regions (close to  $\simeq 90^\circ$  elevation).

Now a more careful comparison of Fig.5.4 and Fig. 5.5 reveals the following;

- There is no difference in the detected locations of the photons, which means that the slight increase in optical thickness has no *visible* effect on the amount of photons that have been scattered by the cloud. By careful examination of the unprocessed output files of the two datasets it is concluded that there are differences present, but the differences are too small to be detected for this simulated ZPEC case. This immediately means that it is useless to compare the detected polarization degree of the cloud at these three frequencies as no difference shall be visible. The maximum brightness signal can be compared for datasets that have different albedo, but the difference shall be equal to the ratio of the albedo. Of course this is only true for cases where the amount of multiple scattered light is negligible, which is the case for the simulated detector views.
- The maximum brightness for the image at 450nm with an albedo of 0.07 is  $\simeq 2.2$  photons/pixel and for the image at 800nm with an albedo of 0.23 the maximum detected brightness is  $\simeq 7.2$  photons/pixel. The ratio between the two values is indeed equal to the ratio of the albedos. One might wonder how it is possible to have maximally 2.2 photons in a pixel, but this is caused by the way the albedo is treated in ZPEC. Instead of using the albedo as the fraction of the photons that is actually scattered when they meet a dust particle (which would be only 15% of the simulated photons in case the albedo is 0.15), the albedo is used as a weigh for the photon properties and hence it is possible to detect fractions of a photon.
- The maximum polarization degree is found for a wide range of pixels that are located in a ring close to the Sun that extends from about  $30 - 60^\circ$ . It means that these locations photons have been scattered at angles close to  $90^\circ$ . This is not due to photons that have been scattered multiple times as analysis shows that there are virtually no such photons detected, so these photons have been scattered only once by the smooth zodiacal dust cloud.

## Conclusion

Based on the detector images of the dust it must be concluded that there is no detectable difference in the degree of polarization of the scattered light at 450nm and 800nm (there would have been a difference if the phase functions for different wavelengths would differ). It is hence of no use to further analyze the detector images at different frequencies. Using a higher albedo for the datasets results in an equally higher detected maximum brightness. The location of the scattered photons on the detector can be explained using the location of the observer and the geometry of the cloud. The maximum polarization degree is 22% and is found primarily south from the Sun in a ring at about  $30 - 60^\circ$ .

### 5.1.4. LOUPE view with Earth simulated

Of course in case of LOUPE, the Earth is also in its view. To determine what is the signal of the dust in comparison with respect to the signal of the Earth, the location of the Earth as seen along the moon-Earth vector is plotted in the detector image at 800nm with an albedo of 0.15, see Fig.5.6. The signal of only the Earth is shown in Fig. 5.6a, for which the reference planet with corresponding phase functions is used as described in Section 5.2.1. The total image of the dust and the Earth is found in Fig. 5.6b. The corresponding polarization degrees are found in Fig. 5.6c and 5.6d.

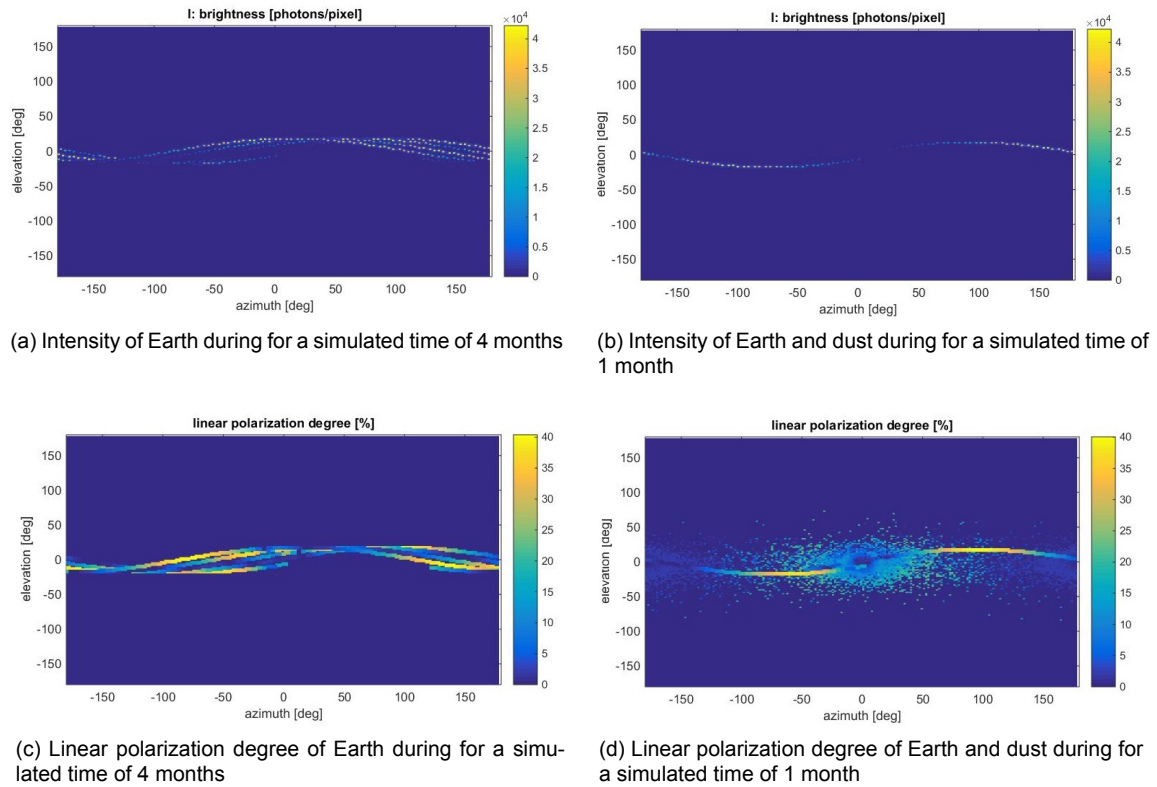


Figure 5.6: View of LOUPE detector. Image at 800nm with an albedo of 0.15, the location of the Earth is plotted with a timestep of 0.3 days. To generate these views, the extended dust databases were used.

There is no clear difference in the intensity plot for the case where only the Earth is simulated and the one where the dust is shown as well: the signal of the dust is too low compared to the Earth signal. The maximum ratio of the Earth signal compared to the dust signal is found when the Earth is located at  $58^\circ$  azimuth and  $13^\circ$  elevation, for which the received Earth intensity is  $3.787e4$  photons/pixel and the dust intensity 0.15 photons/pixel. Hence the brightness of the dust is  $\simeq 4 \cdot 10^{-4}\%$  of that of the Earth. It is even questionable if this difference can be measured by LOUPE. In the backscattering region where the signal of the Earth is lower the maximum percentage of the dust with respect to the Earth signal is found. In this region the intensity of the Earth is 209.1 photons/pixel compared to a 0.3 photons/pixel of the dust. This yields a percentage of 0.14% of the dust brightness compared to the Earth.

Although it can be concluded that when looking at the intensity of the Earth the Earth can be perfectly distinguished from its dusty surrounding, this is not always the case when considering the polarization plots. It can be seen in Fig. 5.6c and 5.6c that the Earth sometimes seems to disappear in the background polarization signal of the dust. To have a better idea of when the Earth seems to disappear in the background signal, views are made of the Earth in the background signal for each day starting from  $t=0$ , for a simulation period of about 4 months. The results for the first month can be found in Fig. 5.7, the results for the remaining months can be found in Appendix D. It can be seen that at  $t = [11, 24, 25, 26, 27, 31, 43, 44, 54, 58, 59, 70, 85, 86, 87, 102, 103]$  days the signal of the Earth has (about) the same polarization degree as the signal from the surrounding dust, this is thus 17% of the total simulation time. It however can be seen that sometimes the pixels in the images are white, indicating that there were no photons detected at these locations.

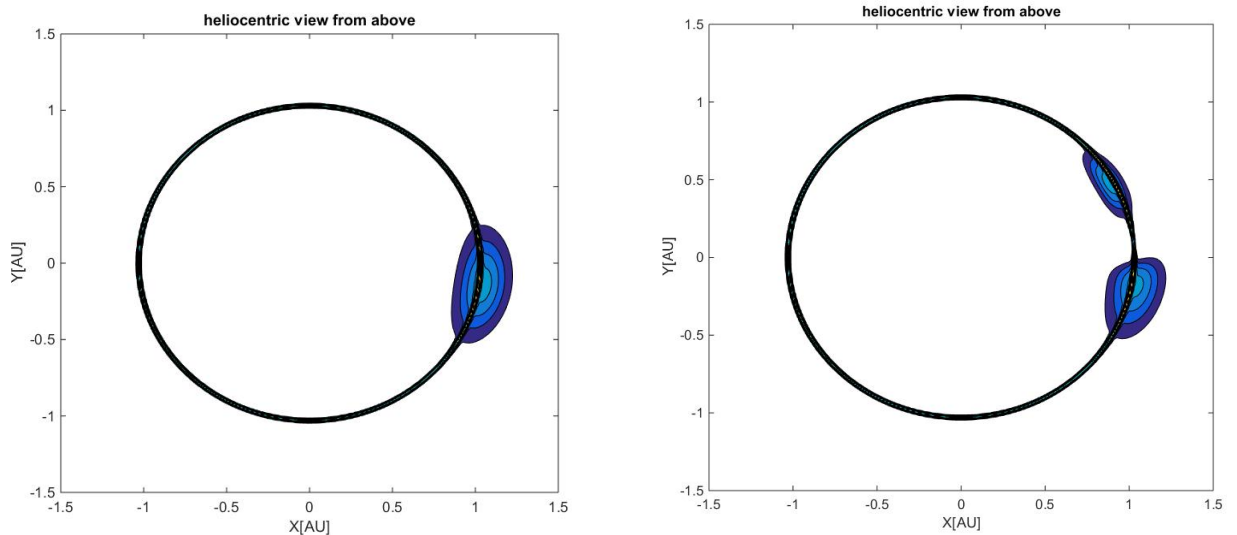


## Conclusion

When the brightness image of the Earth and its surroundings are considered the Earth can be perfectly distinguished from the dust. An analysis of the brightness of the Earth and the surrounding dust as a function of time, shows that the maximum brightness of the dusty background is 0.14% of that of the Earth. However when only the polarization degree is considered the Earth sometimes seem to disappear in the background signal of the dust, as then the light coming from the Earth has the same polarization degree as the surrounding dust. Although the images were created using the extended database it must be noted that there are still empty pixels in the simulated detector images.

### 5.1.5. Comparison with and without Earth trailing high density region

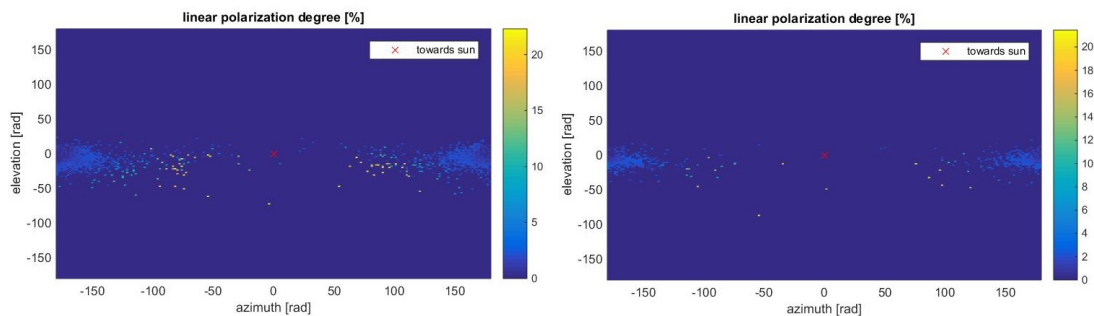
The contribution of the Earth trailing high density blob can be investigated when the results for only the precise dataset are viewed, as the precise dataset does not include the smooth cloud and only contains the asteroidal bands and the Earth circumsolar ring. To refresh the readers mind the isodensity contours of the two different considered models are once more shown in Fig. 5.8, with the original model is shown in 5.8a and the adapted model is shown in fig. 5.9a.



(a) Original model

(b) Adapted model

Figure 5.8: Isodensity contours of the Earth circumsolar ring models. Isodensity contours are shown for  $[0.2, 0.4, 0.6, 0.8, 1.0, 1.2, 1.4, 1.6, 1.8, 2.0]n_{SR}$  with  $n_{SR}$  the density of the smooth ring component at 1AU. The Earth is located at  $[1,0]$  AU.



(a) Original model, extended dataset

(b) Adapted model, basic dataset

Figure 5.9: Polarization contribution of the precise database that only contains particles scattered by the Earth circumsolar ring and the asteroidal bands. Image at 800nm with an albedo of 0.15.

It can be seen that if the observer is located at 1AU at zero degree azimuth, the observer is located in the trailing blob of the original model. In case of the adapted model the trailing bulge is much smaller and hence it can be expected that less photons shall fall on the detector at an observed angle of  $-90^\circ$  azimuth. It is also expected that more photons are found in the Earth leading direction. Considering the location of the leading blob this should be at about  $80 - 85^\circ$  azimuth angles.

Now compare the two detector images in Fig. 5.9 and the following stands out:

- For both images there are little photons observed around azimuth angles of  $-90^\circ$  (orbit trailing direction) and  $+90^\circ$  (orbit leading direction). This actually means that no definite conclusion can be drawn based on these images.
- In order to determine the influence of the trailing and leading blobs, the observed intensity can be calculated in leading and trailing directions. For this analysis the intensity at the detector for the trailing high density region was added for azimuthal angles  $(-110, 0^\circ)$ . For the leading high density region the intensity is summed up over azimuthal angles  $(0, 110^\circ)$ . It is then found out that for the original model the trailing direction is brighter with 13%. For the adapted model the leading direction is 16% brighter than the trailing direction. However as was already mentioned the amount of photons detected in trailing and leading orbit directions is so low that it is hard to give any definite conclusions, so the results must be interpreted with care.

### Conclusion

The use of the original model for the Earth circumsolar ring results in a brightness that is 13% brighter in the trailing direction, compared to the leading direction. Using the adapted model causes the brightness in the leading direction to be higher, the leading direction is now 13% higher than the trailing direction. However as for both cases the total amount of particles in the trailing/leading directions was low the uncertainty in these numbers is high. The low amount of particles detected in these regions also means that the results presented in this thesis are not affected significantly by using either the original or the adapted model.

### 5.1.6. Skyplots of the zodiacal dust intensity and brightness

The images of zodiacal dust can also be plotted as a skyplot similar to the figures shown in Fig. 5.10, which is taken as a reference case. To do this the first quadrant of data is selected, which corresponds to positive elevation angles and positive azimuthal angles.

From the reference case it becomes clear that the intensity of the dust is the highest when looking towards the Sun. Overhead (in the direction of the North Ecliptic Pole) the detected intensity is the lowest and the detected intensity gradually increases towards the ecliptic equator. The degree of polarization is the highest in the direction of the North Ecliptic Pole and seems to be the highest in an azimuthal direction of  $60^\circ$ . The brightness of the reference case cannot be compared with the simulated brightness, as the latter only concerns a part of the photons that leave the Solar surface (the amount of simulated photons is much lower than the amount of photons leaving the Sun every second). Only the contours of the intensity map can be compared. The polarization degree of the reference case *can* be compared with the ZPEC results which are found in Fig. 5.11.

Immediately there is one thing that stands out when looking at the skyplot generated using ZPEC: actually there are too little datapoints to really compare the ZPEC simulation with the reference case. However some careful conclusions can be drawn:

- The ZPEC observed brightness at the North Ecliptic Pole is zero, which could correspond with the low brightness detected in this region for the reference case.
- Moving along the ecliptic in the ZPEC simulated view, the brightness first decreases towards an azimuthal angle of  $90^\circ$  and then increases again towards  $180^\circ$ . This is the same for the reference case although in this image the minimum observed brightness is found at angles of  $120^\circ$ , whereas for the ZPEC image it is located at  $100^\circ$ .
- The region with maximum polarization seems to form a ring around the Sun and in the ecliptic it is the highest at an angle of  $40^\circ$ . This does not match the reference case that has the maximum

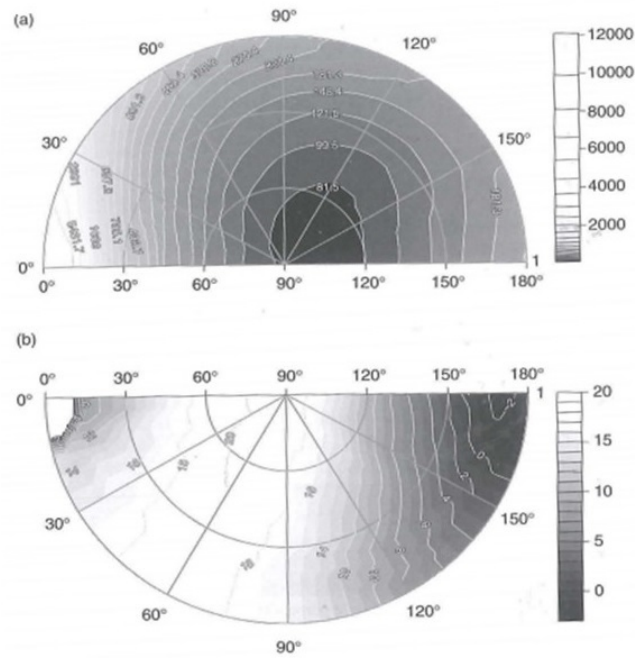


Figure 5.10: Above: map of the zodiacal light intensity ( $10^{-8} \text{ W/m}^2 / \text{sr} / \mu\text{m}$ ) at 550nm. Below: map of the zodiacal polarization. The outer circle represents the ecliptic, the point at  $0^\circ$  is the Sun and the central point is the ecliptic pole. This data is based on the data from Dumont and Sanchez (1975) and leinert et al., (1998). The image itself is retrieved from (Kolokova et al., 2015)

polarization found at an angle of  $60^\circ$ . It is possible this is an effect of the used phase function. The ring-shaped structure of the maximum polarization degree for the ZPEC simulation is also found back in the reference case, although for the reference case the maximum polarization degree is found at the ecliptic north while for ZPEC it seems the maximum polarization degree is found at  $0^\circ$  elevation.

- The value of the maximum polarization degree is slightly higher for ZPEC than for the reference case.
- For the reference case the backscattering region has a negative polarization degree. For ZPEC it can be seen that there is no negative polarization degree at the backscattering region, this is as the polarization degree is calculated as:

$$P = \frac{\sqrt{Q^2 + U^2}}{I} \quad (5.1)$$

which always yields a positive number.

Although there are differences present between the two images, some general features are seen in both the reference images and in the ZPEC generated images. The differences between both can be caused by a variety of factors. First it is thought that that the observations presented in Fig 5.10, the reference case, are made from a specific point on Earth. It means that it is possible that observations are taken in the direction of  $120^\circ$  azimuth while the observer is located at  $80^\circ$  azimuth. The ZPEC results are created as if the observer is located at the same azimuth: it observes  $120^\circ$  as if it is located at  $120^\circ$ . This could be causing a difference between the reference and ZPEC images. Secondly the phase function primarily determines the observed polarization degree. Although the phase function was constructed while trying to match the real behavior of zodiacal dust (see Section 3.2.3), it is not certain into what extend this was succesfull. Furthermore it is noted in Section 3.2.3 that the actual maximum polarization degree of zodiacal dust changes with heliocentric distance. ZPEC uses just one phase function and hence the maximum polarization degree is fixed for all heliocentric distances.

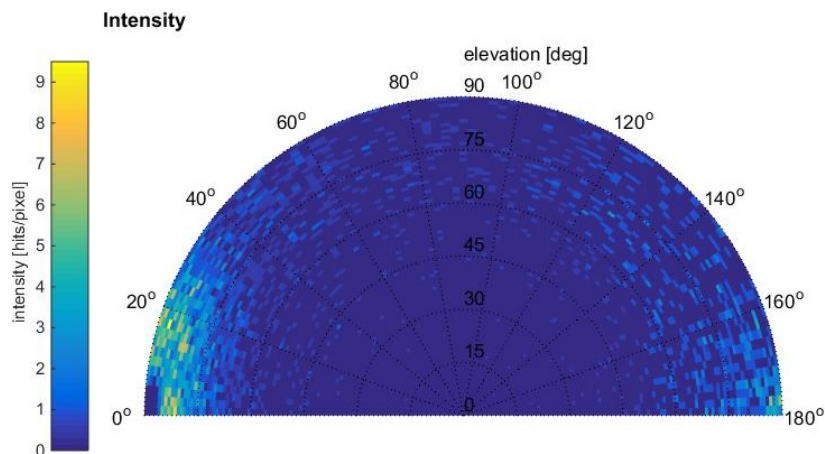


Figure 5.11: Brightness skyplot constructed for an Earth-based observant. The point  $0, 0^\circ$  corresponds with the Sun, the outer circle is the ecliptic (the elevation is measured from the North Ecliptic Pole). The North Ecliptic Pole is located in the point  $(90, 0^\circ)$ , the point  $180^\circ, 180^\circ$  corresponds with the anti-Sun direction. The extended databases were used to generate this view.

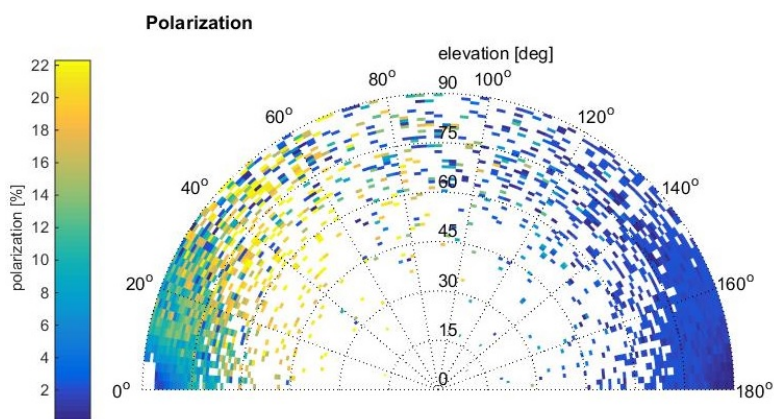


Figure 5.12: Polarization skyplot constructed for an Earth-based observant. The point  $0, 0^\circ$  corresponds with the Sun, the outer circle is the ecliptic (the elevation is measured from the North Ecliptic Pole). The North Ecliptic Pole is located in the point  $(90, 0^\circ)$ , the point  $180^\circ, 180^\circ$  corresponds with the anti-Sun direction. The extended databases were used to generate this view.

## Conclusion

Actually too little datapoints are available to make a fair comparison of the ZPEC results with the reference case. It seems in general that trends shown in the reference images are also present for the ZPEC images, but ZPEC predicts that the highest degree of polarization is found at regions closer to the Sun. It is thought that the differences are caused by the use of a phase function that does not completely match the zodiacal dust behavior as a function of heliocentric distance. In addition differences are caused by ZPEC constructing an image of the sky as if it is located exactly at the same coordinates as the direction it is viewing, whereas the true measurements of the zodiacal dust are made from a single point of the Earth.

## 5.2. Results for the dust disk surrounding $\beta$ Pictoris

Planetary system  $\beta$  pictoris has a relatively optically thick dust disk surrounding the central star and is seen edge-on. Planet  $\beta$  Pic b is a large planet, orbiting the central star at about 9AU in an orbit inclined with about  $3^\circ$  (Millar-Blanchaer et al., 2015). The clearly observable dust and the planet make this planetary system an easy target for observations. Therefore it is used as subject of our analysis.

ZPEC was used for four types of analyses on the  $\beta$  Pictoris system: a nominal view of the dust, a view of the dust in case the maximum number of scatterings was limited to one, an analysis of the importance of taking the polarization state of the perturbed photon into account to determine the scattering direction and an analysis on a dust clump.

Before the results are discussed, it shall be first explained how the observer view is created and how the planetary signal is included in the observer view.

### 5.2.1. Creating an external observer view

In the case of  $\beta$  Pictoris the observer is located outside the reference grid at a distance  $R_{ext}$  from the star. A flat detector surface with 200 pixels in both horizontal and vertical direction is assumed, it is directed normal to the radial direction. In the ZPEC data files the photons are selected that leave the reference grid through the outermost layer. To determine where the particles fall on the detector surface a few steps have to be taken.

#### Propagation of the photons

The first step is the propagation of the original photon locations that represent the exit locations of the photons from the outermost layer with grid cells, see Fig. 5.13a. It is assumed that the photons travel straight in the direction of their propagation. Using this direction the photon locations are propagated to a sphere that has a radius larger than  $R_{ext}$ , by default the radius of this sphere is  $1.5R_{ext}$ . See Fig. 5.13b for an example of such a propagated photon cloud. For all images of the  $\beta$  Pictoris dust cloud  $R_{ext} = 3.4e5AU$

#### Movement of the coordinates

Now the detector surface is located in between the two photon clouds (the one with the original exit locations and the propagated photon locations) and on their way out, some of the photons have come across the detector surface. To determine which photons have and where they have crossed the detector surface a rotation and a translation have to be performed. The goal is to get the detector surface parallel with the y-axis (so  $x = 0$  for all photons on the detector), with the center of the detector at the origin of the new reference frame.

1. The first step is to rotate both photon clouds over the heliocentric angles of the observant. In case the observant is located on the x-axis (zero azimuth and zero elevation) the net result of this rotation is zero. If the observant is located at another azimuth and/or elevation, the result is that the center of the detector now is located alongside the x-axis. To do this, the rotations are performed over the negative angles that describe the location of the observant (so if the observant is located at positive elevation, a negative rotation is performed to align the observant with the x-axis).
2. The photon locations are translated over the distance of the observant, such that the center of the detector surface is at the origin of the reference system.

#### Selection of the photons that fall on the detector

Now that the photon clouds are rotated and translated, it can be selected what photons fall on the detector surface. To do so, several steps are taken;

1. First it is determined for all the photons which ones have an x-coordinate that has switched sign. These are the photons that potentially have come across the detector surface

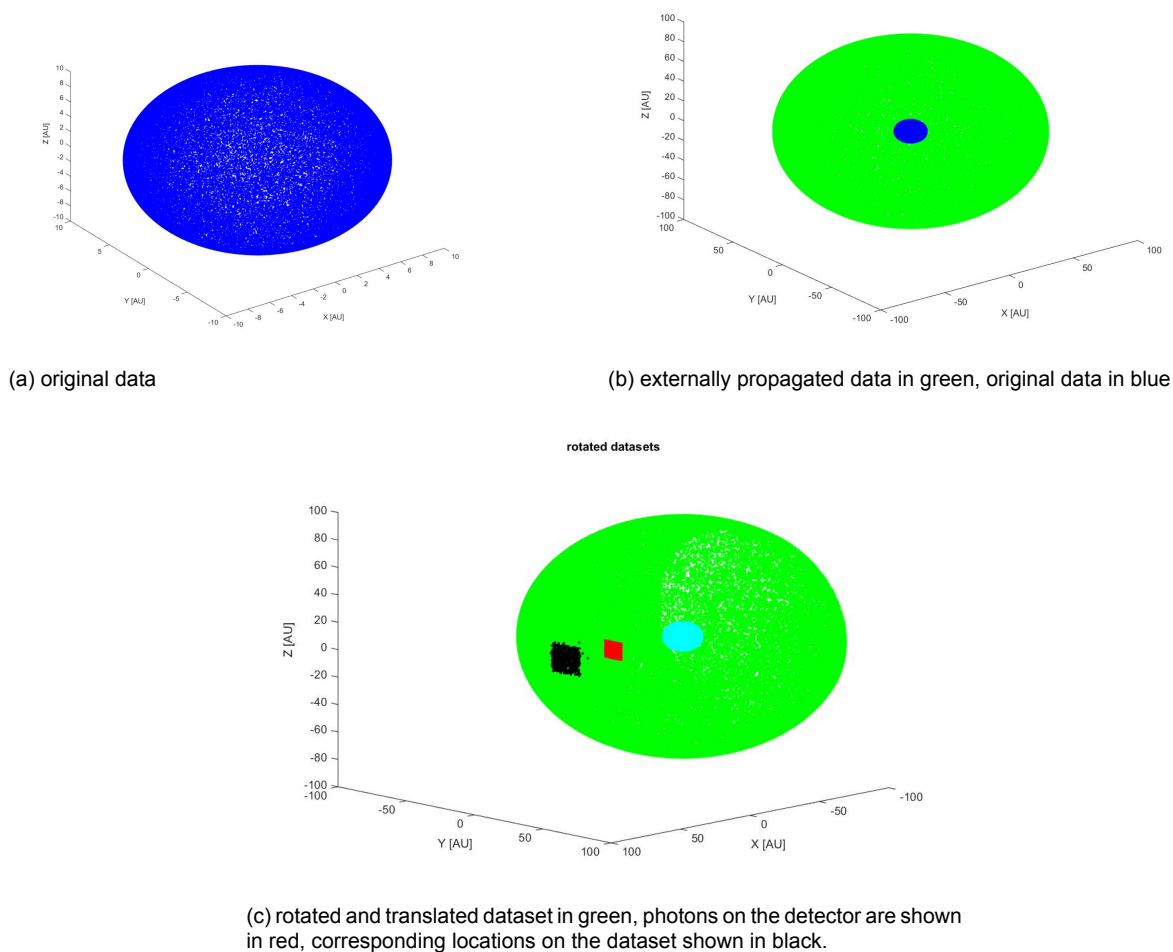


Figure 5.13: Illustration of rotations and translations to determine which photons fall on the externally located detector. Please note that these photon locations were only generated for illustrative purpose and do not represent the locations of photons scattered by the actual dust disk surrounding  $\beta$  Pic

2. Using the fact that the photons travel in a straight line now the  $y$  and  $z$  coordinates can be calculated that represent where the selected photons have crossed the  $yz$  plane.
3. Using the detector diameter the photons that actually have crossed the detector surface are selected.
4. Then the angle constraint is applied in order to select the photons that arrive at the detector surface under a satisfying angle. In reality photons fall virtually perpendicular to detector plane, as the detector is located at large distances from the observed dust disk. As this is not the case for ZPEC the photons are subjected to an angle constraint. Photons from which their incoming angle with respect to the normal is smaller than the angle constraint are assumed to hit the detector perpendicular to the surface, see Fig. 5.14. The angle constraint is set at  $3^\circ$  for the images of  $\beta$  Pic. This number was chosen such that it is not too large (which would lead to too many photons on the detector plane that have unexpected polarization properties or disturb the view) and not too small (which would lead to too little detected photons).

The result of this process can be seen in Fig. 5.13c, for which the detector size was exaggerated for illustrative purpose. Here the photons that fall on the detector are shown in red, in black are the locations of the selected photons on the propagated sphere.

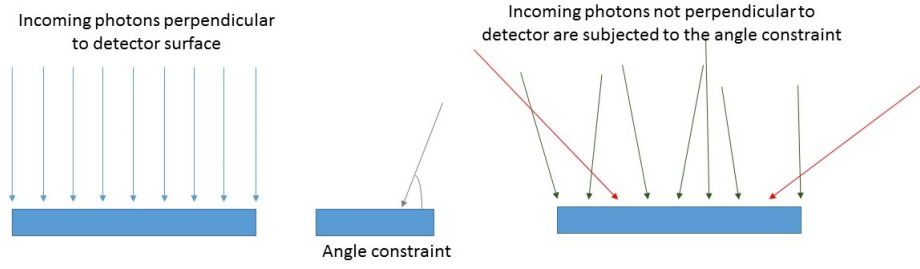


Figure 5.14: Angle constraint. In a perfect situation the photons fall in perfectly perpendicular to the detector. As this is not the case with the Monte-Carlo approach, the photons that fall on the selected are subjected to an angle constraint.

For all the output files a process file is made that stores the properties of the photons that fall on the detector and their detector location. All the process files are stitched together to yield one main process file.

### Construction of the detector image

The detector image is constructed in the same way as for the observer located in the Solar System, however now the coordinates are different. The coordinates of the photons are given in  $y$  and  $z$  (as for all the photons  $x$  is zero).  $z$  corresponds with the bins in vertical direction and  $y$  with the bins in horizontal direction. The binned properties are plotted against the detector coordinates, which are given in [arcsec] from the center of the image.

### 5.2.2. Including a planet for an external observer

In order to find out if a dust clump can be distinguished from a planet it is necessary to include the planetary signal in a dust disk. In this case the observant is located outside the reference volume. To include a planetary signal in the dataset a few steps are undertaken.

#### Incoming flux

First the geometry of the planet orbit with respect to the central star is determined. It is assumed that the orbit of the planet is perfectly circular with a predefined inclination  $i$  and longitude of ascending node  $\Omega$ .

As the planet travels through the reference volume, it travels through different grid cells. For all the simulated locations of the planet the incoming Stokes vector of the planet has to be determined. It is assumed that the photons that are scattered by the planet all come directly from the star. Therefore their Stokes vector only contains a total intensity. The intensity that is scattered by the planet is approximated using the ratio of the planetary disk  $A_{disk}$  over the cross-sectional area of the grid cell  $A_{cell}$  in the following way;

$$I_0 = N_u \frac{A_{disk}}{A_{cell}} \simeq N_u \frac{\pi D^2}{4R^2 \Delta az \Delta el} \quad (5.2)$$

in which  $N_u$  is the number of unscattered photons that travel through the grid cell,  $D$  is the planet diameter,  $R$  is the planet heliocentric distance,  $\Delta az$  is the azimuthal span of the grid cell and  $\Delta el$  is the elevational span of the grid cell.

#### Reflected flux

The scattering angle can be obtained in a similar way as for the internal observant. It is assumed that the planet is treated as a single point and that there are no variations over the planetary disk. This is a valid assumption as the planet is likely not to cover more than one single pixel at the detector surface and hence variations would not be observable. Using the scattering angle and the scattering matrix

elements the reflected Stokes vector is calculated. The elements of the scattering matrix that are used for the planet  $\beta$  Pic b are the same as for the Earth. Of course it is not likely that both Earth and  $\beta$  Pic b have the same properties and little is known about the atmospheric composition and surface of this planet. However for the purpose of this analysis it shall be enough to determine if a planetary signal can be distinguished from the dust, and for this purpose the simplified phase functions can be used. It is likely however that the signal from  $\beta$  Pic b shows different scattering angle dependent behavior and a different maximum polarization degree.

It is assumed that the light reflected by the planet is not scattered by the zodiacal dust in between the planet and observer. However absorption is accounted for by calculation and application of the extinction factor, which is a function of the optical thickness along the photon path. The photon path is discretized in  $N$  pieces until it leaves the reference volume. The total extinction coefficient  $E$  is then calculated as;

$$E = \exp \sum_{i=1}^N \tau_i \quad (5.3)$$

in which  $\tau$  is the optical thickness,  $i$  represents the discretization step. To obtain  $\tau_i$  the discretized photon path is evaluated at every point and the corresponding reference volume is retrieved. This is then used to find the corresponding optical thickness in the optical thickness matrix. The Stokes vector is multiplied with the extinction factor in order to determine the signal that is received by the observer.

### 5.2.3. Image using SMACK density model

The signal of the dust disk surrounding  $\beta$  Pic has been calculated using in total  $3 \cdot 10^7$  photons. The reference volume extends from  $3-210AU$  and in all directions (azimuth, elevation, radius) 10 bins were used. The optical density model is derived from SMACK (Nesvold & Kuchner, 2015), as explained in section 2.2. From this amount of photons 0.304% of the photons fell onto the detector surface. The results can be found in Fig. 5.15. As this case represent multiple scattering it shall be referred to as the nominal case.

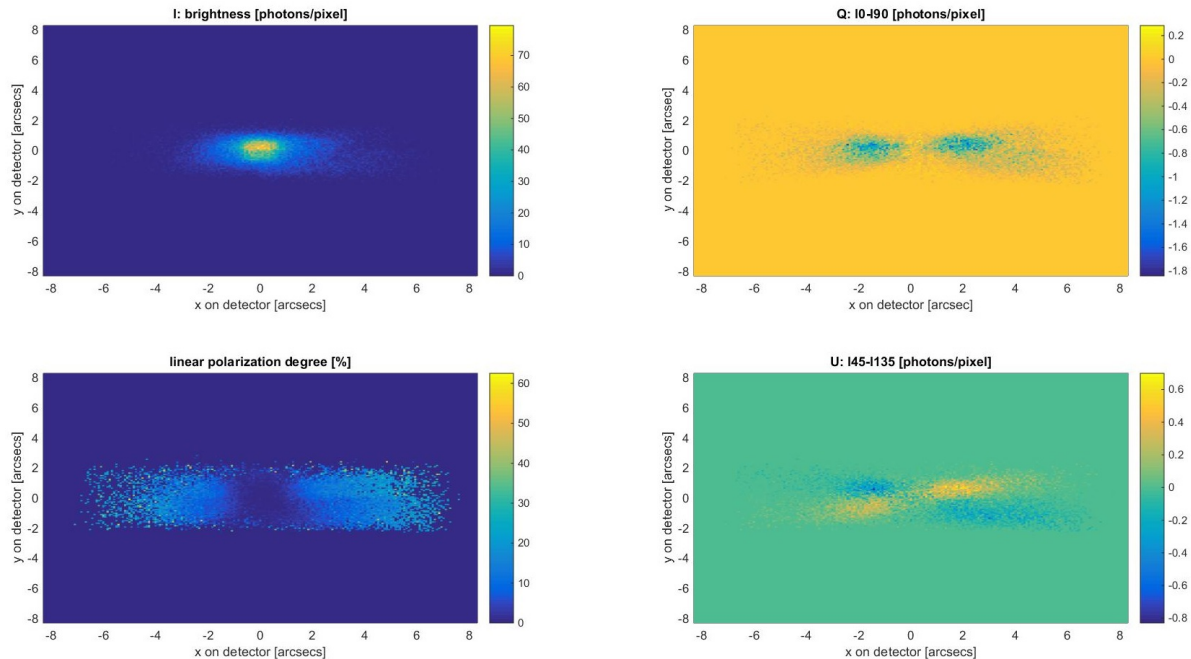


Figure 5.15: Nominal view on disk  $\beta$  Pictoris, simulated using ZPEC using the SMACK derived density model. For this view multiple scattering was taken into account

First of all it can be noticed that the scattered intensity is higher directly north from the disk center than for the south. This is due to the difference in optical thickness of the SMACK model, which is slightly higher at the northern reference grid. Furthermore a faint 'wing' can be distinguished in the fourth

quadrant, which is also a result of the SMACK reference model. It can be seen in Fig 2.9 that there is a higher optical density region present for positive  $y$ -coordinates and negative  $z$ -coordinates (these coordinates correspond with the SMACK density model coordinates, so in detector coordinates this is positive  $x$  and negative  $y$ ).

Furthermore it can be seen that the images for  $Q$  and  $U$  show a butterfly pattern. As the polarization degree is mainly positive in the local scattering plane, it is expected that the polarization vectors are normal to the radial direction. After transformation to the common reference plane (the local meridian) the polarization should be positive in the first quadrant of the  $U$ -image (the polarization vector is directed under an angle of  $45^\circ$  with respect to the local meridian) and the third quadrant. For the second and the fourth quadrant the polarization is positive in the  $U$  image, indicating that the dominant polarization vector is under an angle of  $135^\circ$  with respect to the local meridian, which is normal to the radial. The butterfly pattern in the  $Q$ -image is less prominent but the signs can be explained in a similar way.

### 5.2.4. The importance of multiple scattering in the $\beta$ Pictoris dust disk

Using ZPEC it can be verified if the disk around  $\beta$  Pic is optically thin enough to assume that multiple scattering is not important and hence that all scattering events are single scattering events. This analysis is performed using the SMACK density model from which its derivation is explained in Section 2.2.2. However, radial variations in the observed linear polarization degree will turn out to be important for this analysis and the SMACK images are not smooth in radial direction. Therefore the analysis is also performed using the smooth fan model as used in (Millar-Blanchaer et al., 2015) in order to provide a 'ground truth' for the differences found. First the results for the SMACK density model are discussed, then the results for the smooth fan model are presented.

#### Analysis using SMACK density model

In order to analyze the difference between single/multiple scattering, a dataset is created for which the maximum amount of scatterings of a photon is limited to 1. The resulting detector images can be compared with the 'nominal' view that was shown in Fig, 5.15. The detector image for a single scattering limited disk is found in Fig. 5.16.

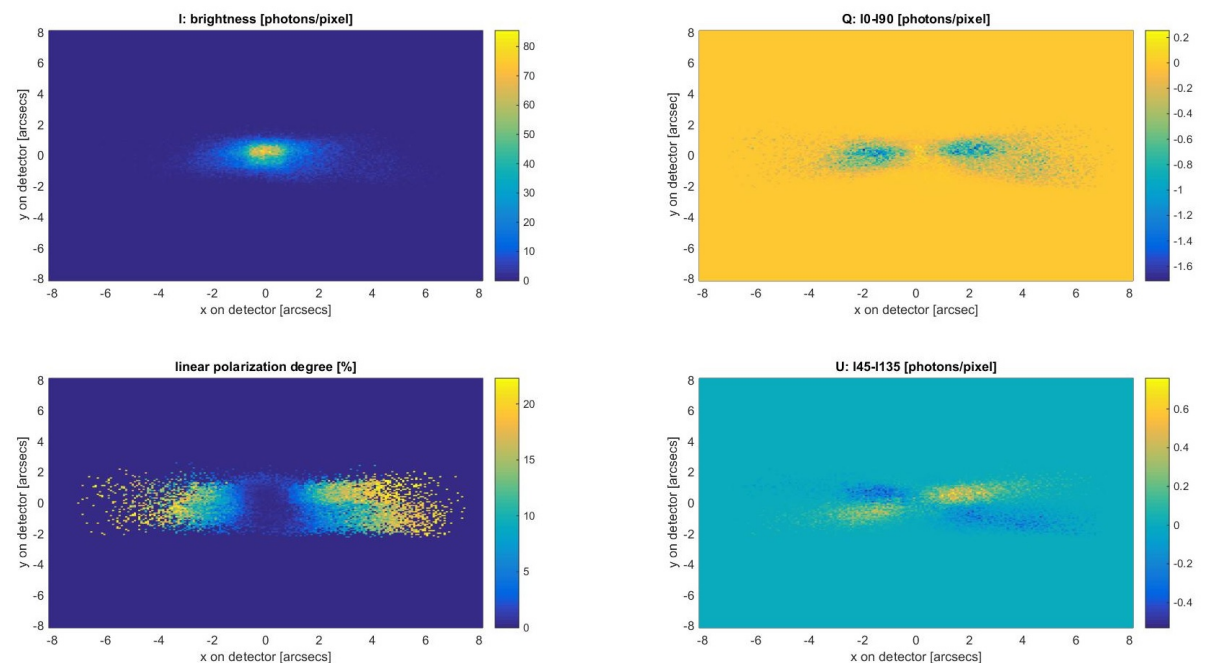
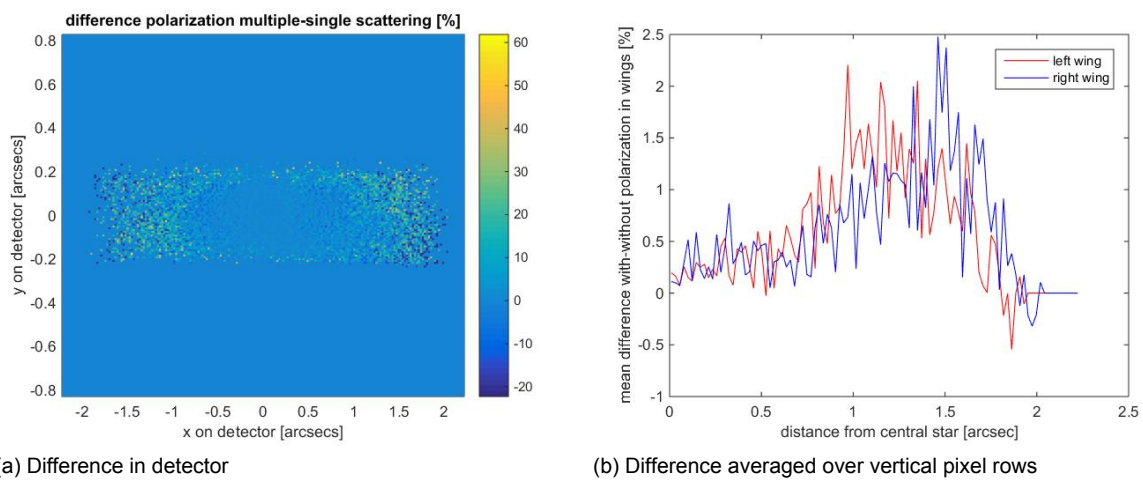


Figure 5.16: ZPEC single scattering view on the dust disk orbiting  $\beta$  Pictoris, simulated using the SMACK derived density model. To create this view the amount of scatterings was limited to one.

Immediately the difference with the nominal case is seen as the maximum polarization degree is  $\simeq 20\%$ ,

where it was incidentally  $\simeq 60\%$  for the nominal case. The difference can be further analyzed when the difference in polarization degree per pixel is plotted as shown in Fig. 5.17a. It can be seen that at the center of the disk the difference is almost zero and it increases towards the edges. Multiple scattering thus contributes more to the edges of the disk. However the difference seems noisy and it is possible that if the differences in these pixels are averaged it approaches zero as well. To analyze this, the difference is averaged over the vertical pixel rows and plotted for the left and right wing, see Fig. 5.17b. Then it is clear that there is a trend visible: the mean difference is the largest at about 1.2 arcsec from the center.

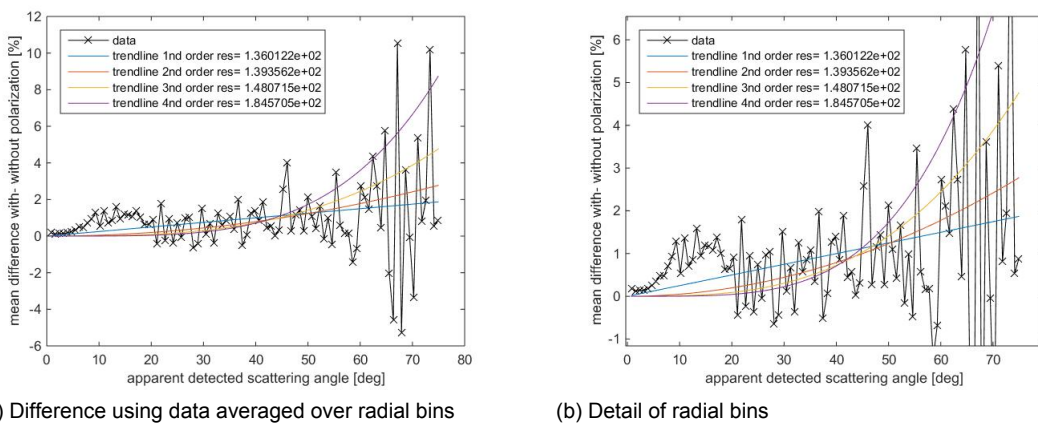
Actually the difference in polarization integrated over the disk height does not provide insight in the effect of the polarization degree as a function of scattering angle. It can be useful to establish a relationship for this effect. Namely, real observations of the  $\beta$  Pic dust disk are used to retrieve the single scattering function under the assumption that multiple scattering is neglected, which provides insight in the composition, material and structure of the dust particles. Of course, the effect of multiple scattering should not be included in the single scattering phase functions, but its contribution is uncertain. Therefore the estimation of this effect as a function of scattering angle is of importance.



(a) Difference in detector

(b) Difference averaged over vertical pixel rows

Figure 5.17: Difference in degree of polarization for multiple versus single scattering



(a) Difference using data averaged over radial bins

(b) Detail of radial bins

Figure 5.18: Difference in linear polarization degree for multiple versus single scattering as a function of scattering angle

To analyze the difference as a function of scattering angle one would like to plot the differences found in the pixels as a function of pixel distance to the central point of the image. This is done using radial bins. To create this image first the data in both the single scattering polarization plot and multiple scattering polarization plot was converted to an array with corresponding distance in arcsec from the disk center.

Then to eliminate the influence of the extreme values, the rows with a polarization degree higher than 95% of that of the maximum polarization degree were removed. This data was then binned in 100 bins and for each bin the average polarization degree calculated. Then the difference for both the datasets (single and multiple scattering) is plotted and can be found in Fig. 5.18a, Fig. 5.18b shows more detail. To construct this image, the distance to the central star was converted to the apparent scattering angle.

To analyze the trend in the datapoints shown in Fig. 5.18a polynomials of orders 1 to 4 were fitted through the data, the residuals can be found in the legend. It is concluded that the first order polynomial fits the data the best. From this fit and the data it can be concluded that taking multiple scattering into account leads to a higher polarization degree compared to only single scattering. According to the linear fit the effect increases with the apparent phase angle and is hence more visible towards the edges of the disk. However, it was already concluded earlier that at high scattering angles the MC effect is visible and hence this region is noisy. In the forward scattering regime however a clear trend is visible and at scattering angles of  $10 - 20^\circ$  the polarization degree with multiple scattering included is higher with 1%. In the region  $20 - 60^\circ$  the datapoints again seem noisy but the average is definitely positive.

### **Analysis using a smooth dust density model**

It can be seen in Fig. 5.16 that there are radial discontinuities in the resulting detector image. These discontinuities are caused by SMACK being an irregular density model. To establish a relation between the difference and the scattering angle radial bins are constructed and hence the SMACK irregularities influence the found relationship. Therefore the same analysis was performed using the smooth fan model from Artymowicz (1997), that does not show such irregularities. The resulting linear polarization degree for single scattering only can be found in Fig. 5.19a, the maximum polarization degree is 23%. If multiple scattering is included as shown in Fig. 5.19b, the maximum polarization degree increases to 45%. The difference can be shown in Fig. 5.19c.

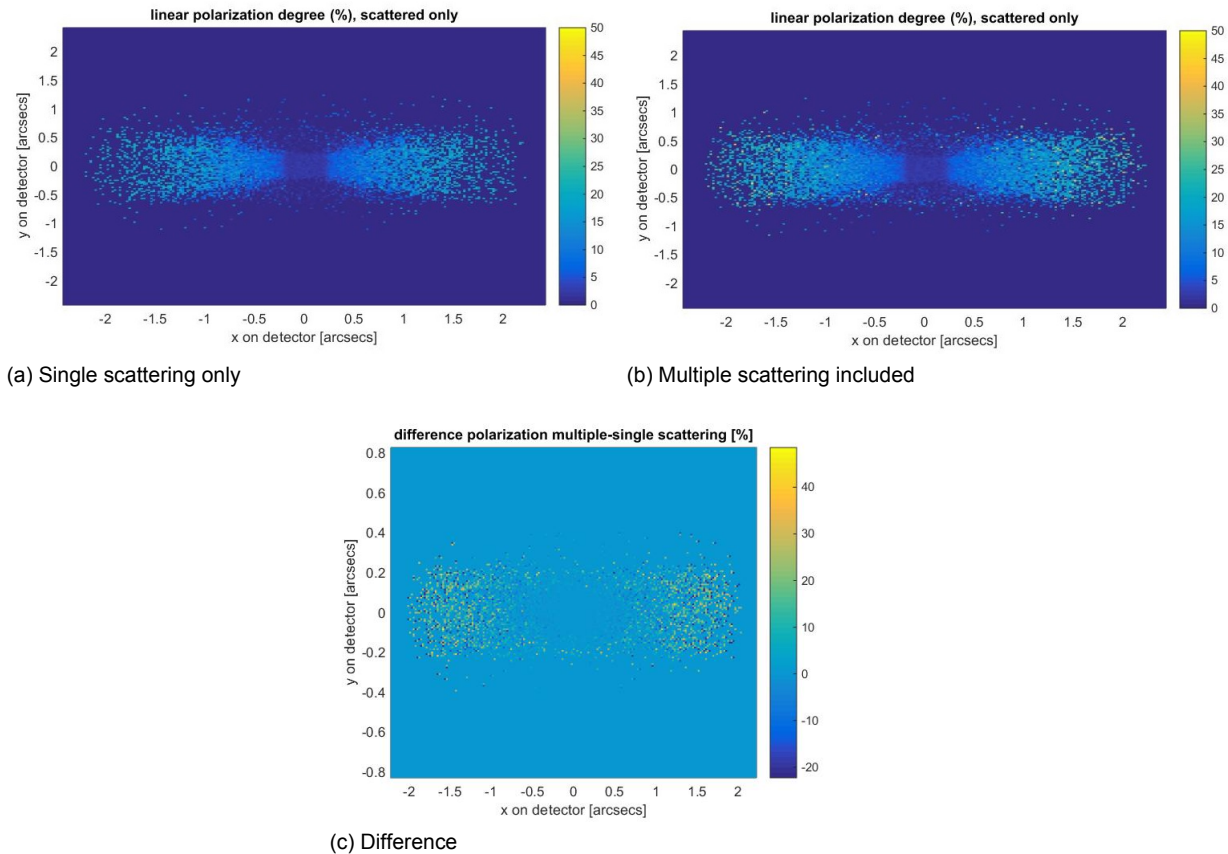


Figure 5.19: Difference in simulated linear polarization degree for the dust disk surrounding  $\beta$  Pictoris when multiple scattering is excluded or included in the simulations.

The difference can be plotted as a function of apparent scattering angle and a trendline can be fitted using 100 bins in scattering angle, see Fig. 5.20a. It can be seen that a first order fit is the best to represent the data. This trendline predicts that the difference between multiple and single scattering increases linearly up to 0.78% at scattering angles of  $75^\circ$ .

Now it can be seen in Fig. 5.20a that the data fluctuates around the trendline and hence one would like to make an estimation of the maximum error as a result of ZPEC being a Monte-Carlo simulator. This can be done using the standard deviation as was calculated in Section 4.3.3 and the amount of photons falling on the detector that are binned similar to the linear polarization degree (in radial direction). Now as the standard deviation of the MC-effect was calculated for a bin width of  $10^\circ$  this is done as well for the error calculation. The result can be found in Fig. 5.20b. Again the trendline is plotted, the datapoints and the MC error. It can be seen that the MC error is significantly smaller than the trendline it is maximally 0.0702% at a scattering angle of  $75^\circ$ .

## Conclusion

Based on the two analyses above, performed using the (irregular) SMACK density model and the (smooth) fan density model, the following is concluded;

- Taking multiple scattering into account leads to a higher polarization degree.
- A linear fit best represent the data. Depending on the density model that is used for the calculation the increase is up to 1.8% (SMACK) or 0.78% (fan model) at scattering angles of  $75^\circ$ .
- In this maximum deviation there is a  $1\sigma$  uncertainty of 0.0707% (absolute) due to the Monte-Carlo effect (this is 9% of the indicated 0.78%).

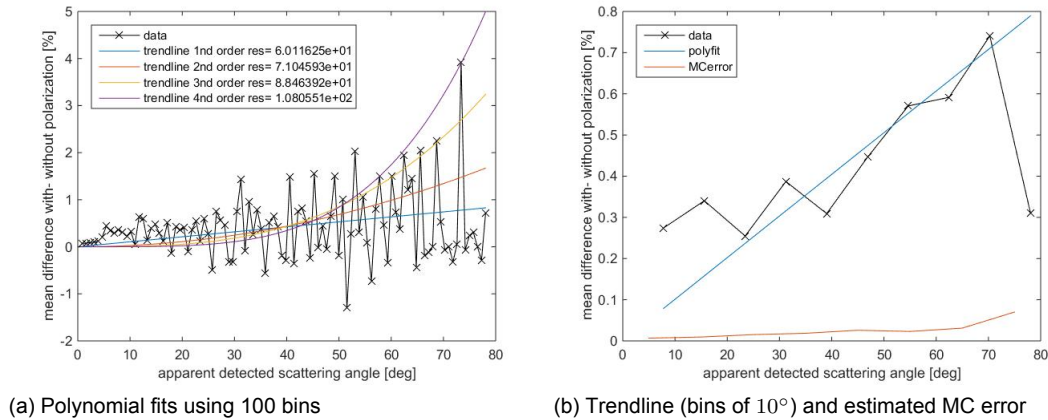


Figure 5.20: Result of polynomial fitting through the data

Therefore it is certain that if the  $\beta$  Pictoris dust disk is analyzed using single scattering theory, the linear polarization degree of the disk is structurally underestimated. Towards the edges of the disk this underestimation shall be at least  $0.78\% \pm 0.07\% (1\sigma)$ .

### 5.2.5. Effect of taking polarization into account to determine scattering direction

As was mentioned in Section 4.3.6, ZPEC can be used to analyze the influence of taking the polarization state into account for the determination of the scattering direction. This only influences images of datasets for which multiple scattering is included as for single scattering the incoming flux is unpolarized. Again as the radial trends in the SMACK image are not smooth, this analysis is again performed using both the SMACK density model and the smooth fan model.

#### Analysis using SMACK density model

A detector image was constructed for a dataset for which the polarization state of the photon is not taken into account to determine the scattering direction and it is shown in Fig. 5.21.

As the results are very similar to the nominal case a more precise analysis is performed, again in the form of a difference plot of the detector itself (Fig 5.22a) and a difference plot as a function of the apparent scattering angle (Fig 5.22b). It can be seen that the difference is almost zero at the center of the disk and seems to increase at the edges. However at the edges the MC effect is likely to play a role and the signal is noisy. This is also visible in the radial bin image, which shows large deviations at high phase angles. The average trend of this data is best fitted by a polynomial of order 2, although this fit is only 2.18% better than the second best fit which is represented by a 3rd order polynomial.

The second order polynomial predicts that the difference between the nominal and the 'without polarization' case increases up to 1.3% at scattering angles of  $70^\circ$  and that the difference increases gradually. This result partially matches the analysis on the same effect that was done using the flat reference surface and is described in section 4.3.6:

- It was concluded earlier in Section 4.3.6 that if the effect would be visible, it would result in increase in polarization of at maximum 0.5% in the regions  $35 - 65^\circ$ . These results were for a dust optical thickness of  $\tau = 5AU^{-1}$  and hence for  $\beta$  Pic the effect would be less prominent. Indeed the 2nd order polynomial fit shows that the polarization degree is larger when the polarization state is taken into account.
- It is questionable if the 2nd order polynomial fit is representable for the true increase in polarization. At a scattering angle of  $60^\circ$  it predicts an increase of 1% whereas it was concluded earlier that the maximum difference was to be in the order of 0.5%. As it is likely the MC effect affects the trendline it was decided to fit a polynomial through the datapoints for scattering angles  $< 60^\circ$  which can be found in Fig. 5.22c. Now the best fit is obtained using a 4th order polynomial. It

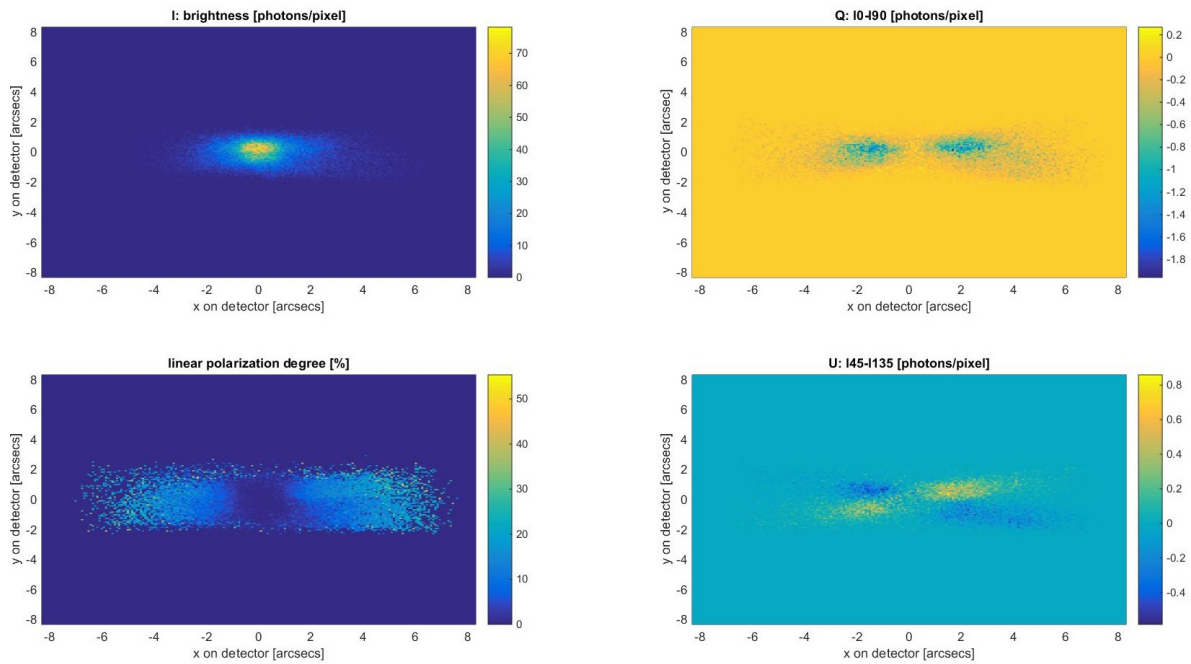


Figure 5.21: Image of  $\beta$  Pictoris but without taking the polarization state of the photon into account to determine the scattering direction.

predicts a difference in polarization degree of 1% at  $\theta = 60^\circ$ , which is still too high compared with the earlier results. The results for smaller scattering angles are closer to what would be expected, for example it predicts a difference of 0.15% at  $\theta = 35^\circ$ . However as the optical thickness of the  $\beta$  pictoris dust disk is  $\ll 5AU^{-1}$  it is questionable if this trendline is even representable for the smaller phase angles.

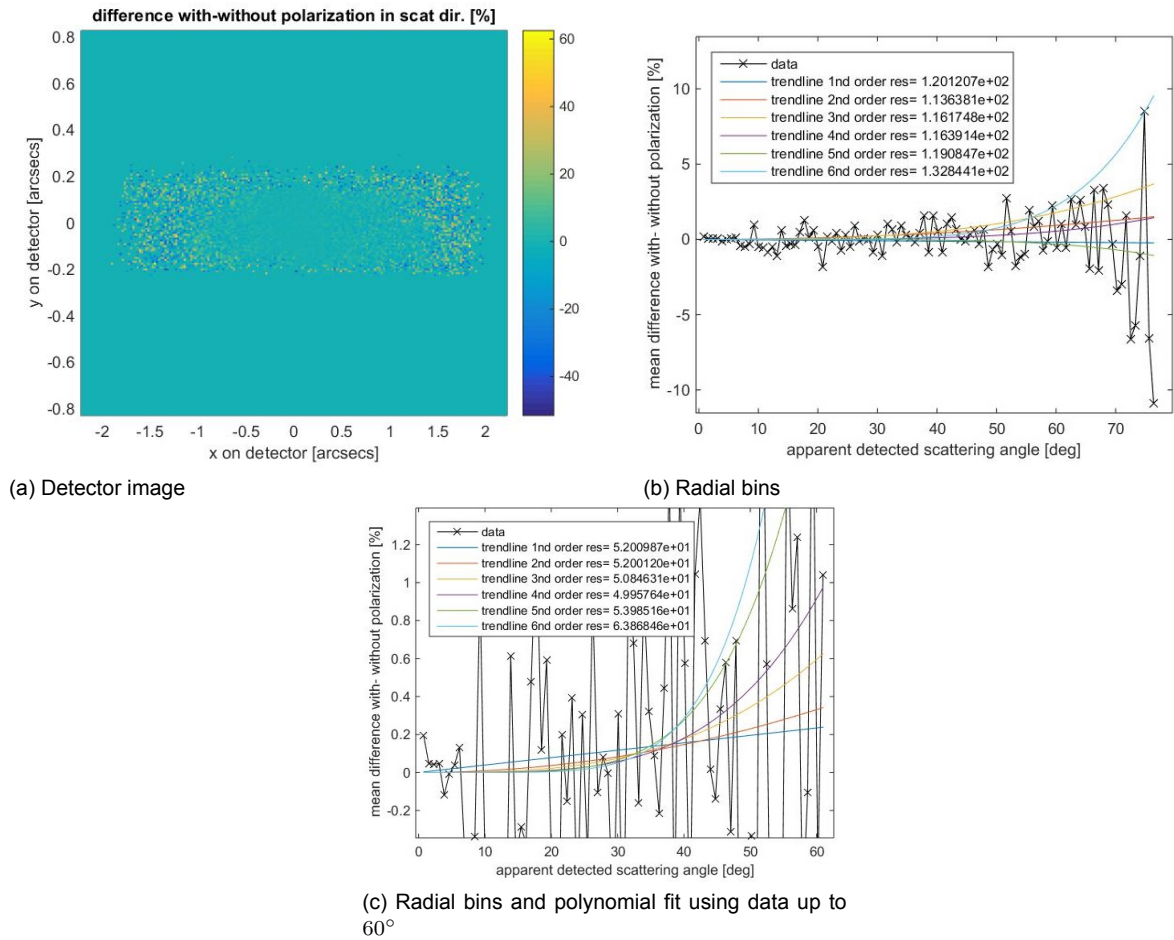


Figure 5.22: Difference of taking polarization state of photon into account versus not taking it into account

### Analysis using smooth fan model

Again the same analysis is performed using a smooth fan model. Using 100 radial bins the data is again analyzed and polynomial fits are plotted through the data as shown in Fig. 5.23a. It can be seen that the best fit is provided by a polynomial of 1st order and hence a linear relationship is expected. It can be seen that the trendline predicts very small difference between taking or not taking the polarization state of the photon into account to determine its scattering direction. Hence it is of interest to know whether this predicted difference is larger than the MC error in order to determine the validity of the results.

The MC error is again analyzed and shown for bins of  $10^\circ$  bin width in Fig. 5.23b. It can be seen that the error is of the same magnitude as the predicted trend.

### Conclusion

The polynomial fit through the radial bins and the difference plots in combination with the earlier performed test leads to the following conclusion on the impact of taking the polarization state of the photons into account to determine the scattering direction for photons travelling through the dust disk around  $\beta$  Pic;

- Depending on the datarange chosen for fitting the data, a polynomial fit through the SMACK data results in a predicted 0.15%-1% higher polarization degree in the range of  $35 - 60^\circ$  scattering angle.
- This does not match the earlier performed test from which it was concluded that the maximum effect would be 0.5% in this same range. As this test was performed for a much higher optical

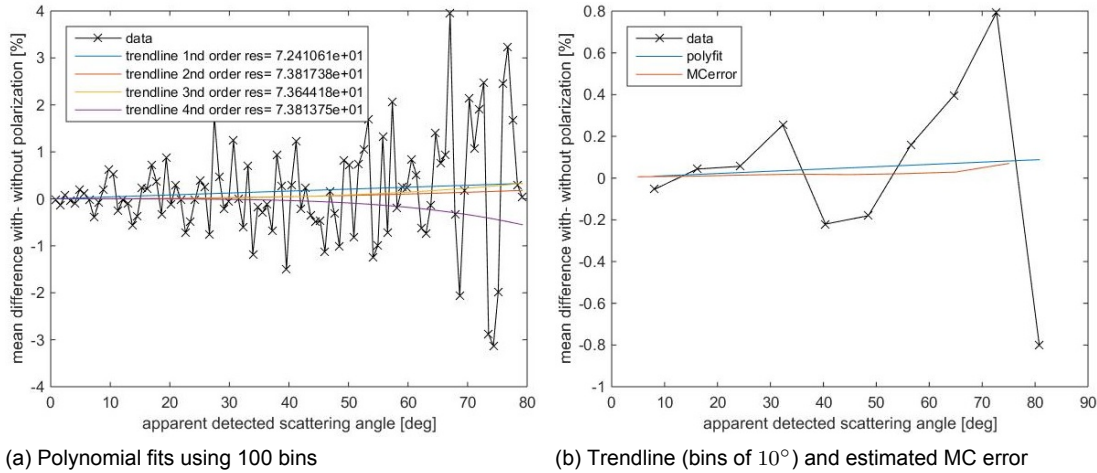


Figure 5.23: Result of polynomial fitting through the data

thickness, the effect for the  $\beta$  pic disk should indeed be less prominent.

- As the SMACK data fluctuates around the y-axis and as it is suspected that the polynomial fit seems unreliable. Therefore it might seem that ZPEC can not be used to analyze the difference.
- To rule out the effect of the radial irregularities in the SMACK model, the same analysis can be performed using a fan model. It shows that the predicted difference in polarization degree is much lower. The MC-error has about the same size as this predicted difference and hence indeed it can be concluded that ZPEC is not suitable to analyze the effect of taking/not taking the polarization state of the photon into account.

The results presented in this section could be improved by simulating more photons with the ZPEC simulator. More datapoints shall decrease the data fluctuations around a potential trendline and shall decrease the MC error.

### 5.2.6. Distinguishing a planet from a dust clump

The last analysis for the  $\beta$  Pic system considers planets and dust clumps. As was already mentioned in section 1.2 dust acts as a source of confusion in case exoplanets are to be observed. In order to compare the polarization signal from a dust clump with a planet, the polarization signal of a planet is first to be compared with that of the dust.

#### Distinguishing a planet from its surroundings

Using the methodology described in section 5.2.2 the location of the planet in the detector image can be reconstructed, as well as the scattering angle of the planet with respect to the observer. Hence the observed polarization degree of the planetary disk can be retrieved. Now as there is a wide variety of orbital parameters that influence how the planet is seen it is decided to perform calculations for two cases: using an orbit that shows a minimum difference in observed polarization degree and using an orbit that shows a maximum difference.

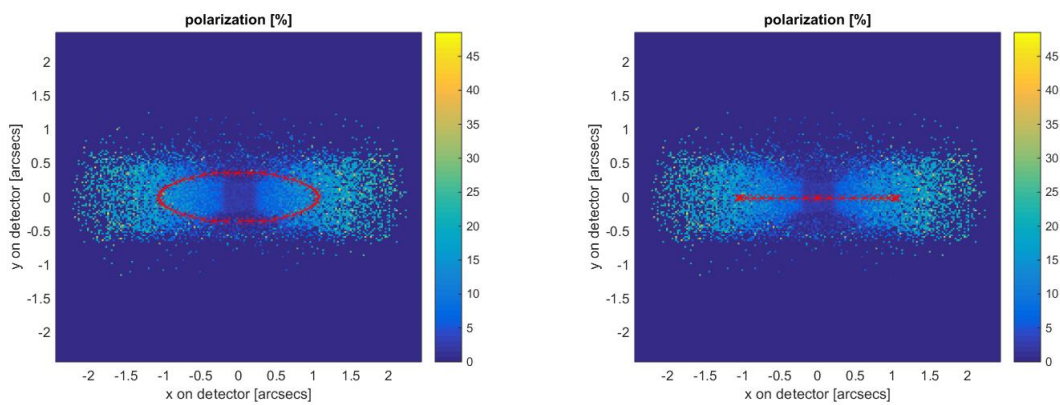
One extreme case is when the orbit is seen perfectly face-on and hence the orbital inclination is  $0^\circ$ . When the orbital inclination changes the difference between the planet and the dust might increase, but orbits with high orbital inclinations are not often seen. Therefore an orbital inclination of  $20^\circ$  is taken as the other extreme case. Of course this analysis can be done for a range of orbital radii, but for this analysis an orbital radius of 100AU is chosen. For the other orbital parameters, see Table 5.2.

The planetary orbits in the reconstructed polarized detector images are shown in Fig. 5.24. To reconstruct the detector image the fan model (Millar-Blanchaer et al., 2015) is used instead of the SMACK optical density model as it provides a smoother image for later purpose when a dust clump is included

in the database. Now the observed polarization degree of the planet is compared with that of the surrounding dust, for which an average was taken over 7x7 pixels with the location of the planet in the middle pixel. This is shown in Fig 5.25.

Table 5.2: Orbital properties of hypothetical planet orbiting  $\beta$  Pictoris.

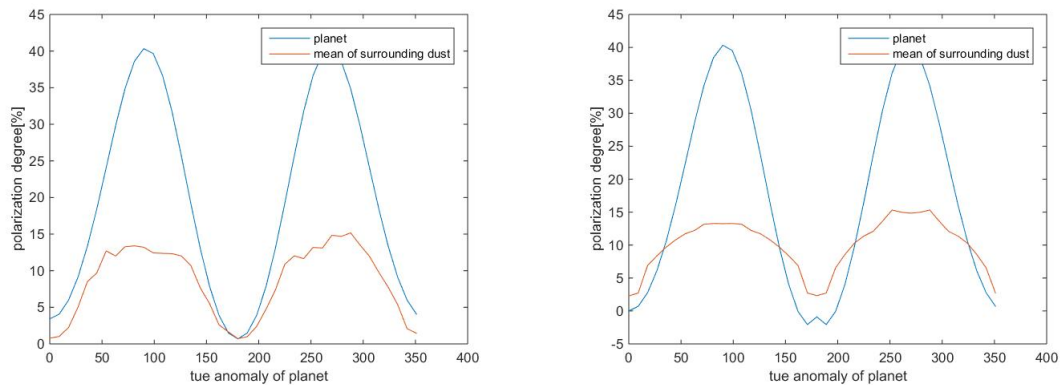
Parameter	Explanation	Value
a	Semi-major axis [AU]	100
e	eccentricity [-]	0
i	inclination [deg]	20
$\Omega$	Right ascension [deg]	0
$\omega$	argument of perigee [deg]	0
tp	time of pericenter passage [s]	0



(a) Orbital inclination of  $20^\circ$

(b) Orbital inclination of  $0^\circ$  thus edge on.

Figure 5.24: The orbit of a hypothetical planet orbiting  $\beta$  Pictoris at 100AU shown in the ZPEC linear polarization image of the surrounding dust.



(a) Orbital inclination of  $20^\circ$

(b) Orbital inclination of  $0^\circ$  thus edge on.

Figure 5.25: Linear polarization signal of a hypothetical planet orbiting at 100AU with respect to the surrounding dust. The signal is given as a function of orbital true anomaly.

As the planet orbits the central star, the signal of the background dust varies, and therefore the dust signal is different for the two cases. For both cases it is seen that when the planet has a true anomaly close to  $0^\circ$  or  $180^\circ$  (in other words if the x-location on the detector is close to 0) the observed polarization

degree of the planet is close to that of the dust and that both reach a minimum. The maximum polarization degree of the dust is about equal for both cases as well as the maximum polarization degree for the planet.

The difference between the two cases is found for the minimum: in case the orbit is inclined with  $20^\circ$  the minima of the planet and dust are the same and can be found at a true anomaly of  $180^\circ$ . In this case the planet cannot be resolved from the surrounding dust. It is however unlikely the signal of the planet is actually reaching the detector image, as it just above the central star and light from the central star is probably blocked out using a coronagraph. It is certain that the planet cannot be observed at this location when the planet is in an edge-on orbit, as the planet is then directly behind the star. However it must be said that for such a configuration the planet seems to disappear in the background signal of the dust for true anomalies of  $30^\circ$ ,  $150^\circ$ ,  $210^\circ$  and  $330^\circ$ . In these cases the observed polarization degree of both the dust and the planet are about 9%. In these cases it depends on the size of the coronagraph if the signal of the planet can reach the detector but this is likely the case.

This analysis can hence be concluded with the statement that if the planet is observed for a longer period of time, it can be distinguished from the dust as the maximum polarization degree of the planet is way higher than the dust. However when the disk is only observed at an instantaneous point in time, it is possible that the planet is close to the central star and depending on the orbital inclination, the planet might not be distinguishable.

When actually observing the planet (instead of simulating its signal) the following needs to be taken into consideration:

- The signal of the planet is unresolved and only corresponds to one single pixel. This means that high polarization values must be measurable and not, for example, being smoothed out during post-processing.
- As the planetary signal only comprises a single pixel, it shall be very hard to distinguish the planet. Especially as the maximum polarization degree that is observed is about 45%, which is the same as for the planet.
- In case of the fan model there are no pixels that show extreme values in polarization, whereas for the SMACK model it did. It may be expected that pixels showing high polarization values are also present for real observations. Therefore the high polarization pixels can be confused with planetary signals if images are only studied at instantaneous points in time (i.e. the movement of the planet around the central star is not captured).

### Distinguishing a dust clump from its surroundings

ZPEC can be used to analyze the effect of a dust clump being present in a dust disk by artificially increasing the optical density in one of the grid cells. It is however uncertain how much this optical density should be increased in order to obtain reliable results. In addition the size of the grid cells is a topic of study. Therefore two different cases were simulated that both have different input parameters.

The first dataset uses relatively small grid cells, the reference volume is divided in 16 bins in azimuthal, elevational and radial direction. A bin that is close to the central star, at 10AU, and located just above the symmetry plane has an increase optical thickness of 10 times the local optical thickness. The resulting images of detected brightness and linear polarization degree as the dust disk shifts in front of the central star are shown in Fig. 5.26 and Fig. 5.27.

It can be seen from both the brightness and polarization images that the dust clump is virtually undetectable. Only in the case that the clump is seen at an almost forward scattering angle (middle picture) there is a shadow visible. This shadow is caused by the clump itself, as multiple scattering decreases the scattered intensity in forward directions while increasing it at other scattering angles. However, this increase at other angles can not be seen from the images.

It is thought that this inability to detect the dust clump can be caused by two reasons: the optical thickness of the clump is too low for it to be detected and/or it is too close to the central star, such that the effect of the clump is negligible to the central bright spot. Therefore a second database is generated with the dust clump located at 100AU and a density 200 times the local density. To reduce

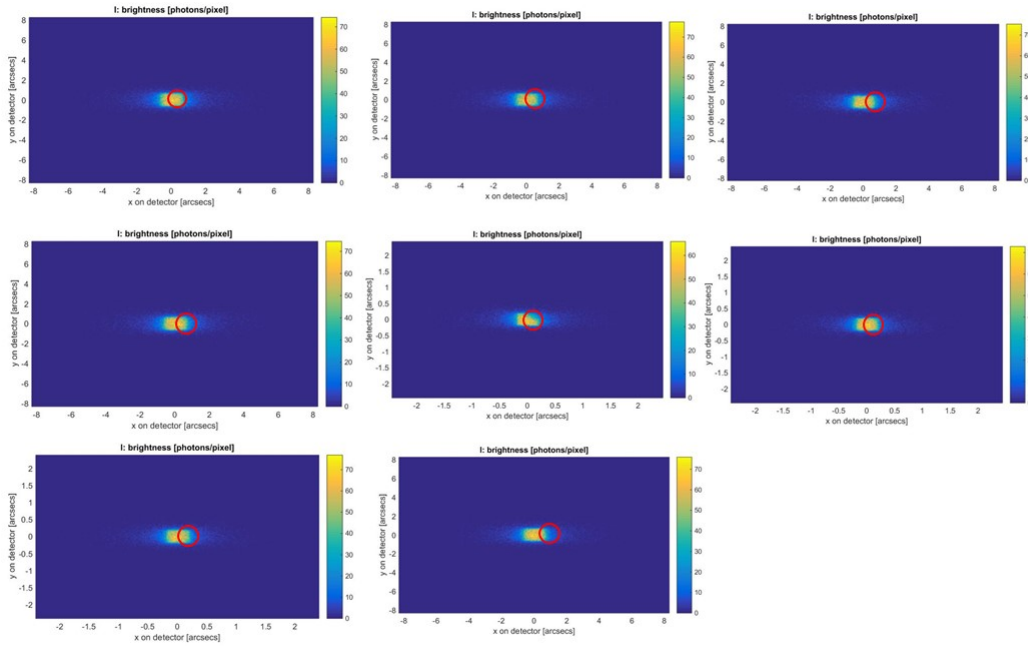


Figure 5.26: Simulated brightness of the dust disk surrounding planet  $\beta$  Pictoris with a high density region in it. The location of the high density region is indicated with a red circle. With the observant located at  $0^\circ$  azimuth the clump for the different views is located at (from upper left to lower right)  $[-90^\circ, -80^\circ, -50^\circ, -30^\circ, 90^\circ, 70^\circ, 50^\circ, 30^\circ]$  azimuth. As a result of these azimuth angles the dust clump is shown in backscattered light for the first four images and in forward scattered light in the last four images.

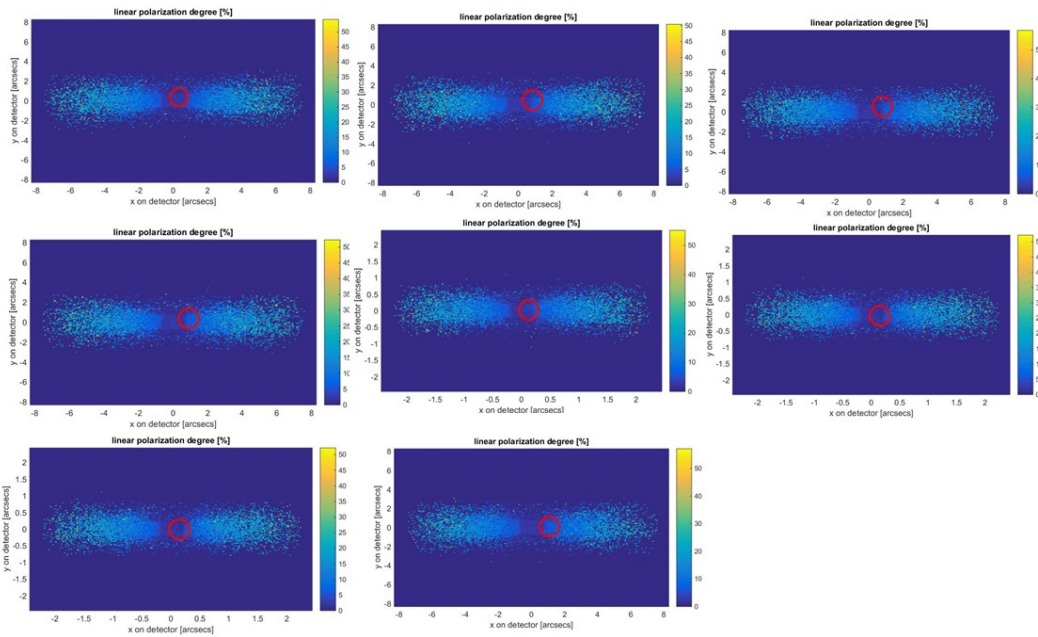


Figure 5.27: Simulated linear polarization degree of the dust disk surrounding planet  $\beta$  Pictoris with a high density region in it. The location of the high density region is indicated with a red circle. With the observant located at  $0^\circ$  azimuth the clump for the different views is located at (from upper left to lower right)  $[-90^\circ, -80^\circ, -50^\circ, -30^\circ, 90^\circ, 70^\circ, 50^\circ, 30^\circ]$  azimuth. As a result of these azimuth angles the dust clump is shown in backscattered light for the first four images and in forward scattered light in the last four images.

the computation time of the simulation the amount of bin cells was reduced to 10 in every direction. The dust clump is located slightly under the local dust symmetry plane.

From the latter database detector views were created as well, the results for the linear polarization degree are shown in Fig. 5.28. In these images the location of the dust clump is indicated by the red circle. The shadow effect that was also found for the first case, is again seen. However the effect is much larger and the shadow is also visible in regions other than the forward scattering regions. The gap is a logical result of the high optical thickness of the dust clump. The optical thickness in the high density grid cell is  $\simeq 0.5AU^{-1}$ . As the undisturbed path of the photons is  $20AU$ , the optical thickness along the undisturbed path is  $\simeq 10$ . It means that only a fraction of  $\exp(-10) = 4.5e-5$  shall travel undisturbed through the grid cell and hence the dust clump shall leave a shadow. Of course in reality such a dense dust clump shall not produce a shadow in the form of a square, but as the grid cells have a quadratic cross-section the simulated shadow also has this form.

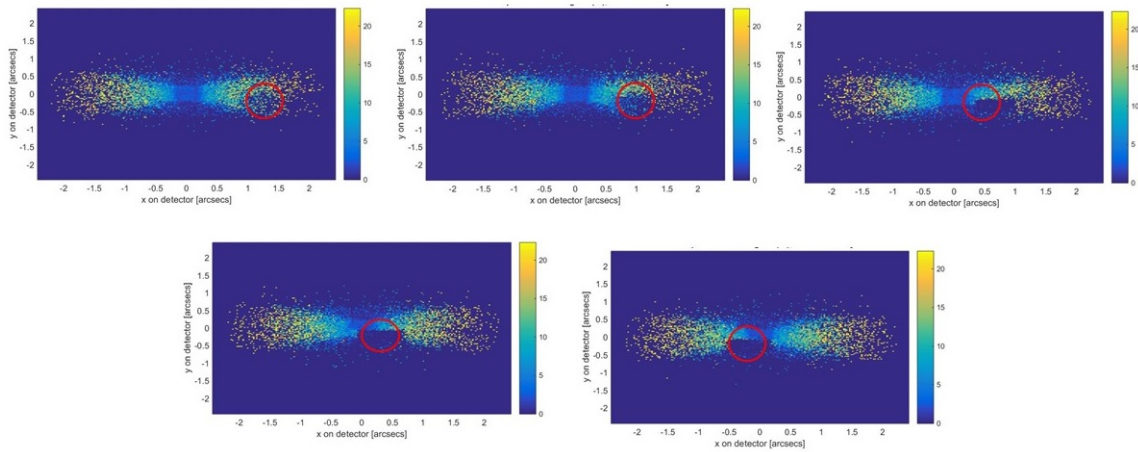


Figure 5.28: Simulated linear polarization degree of the dust disk surrounding planet  $\beta$  Pictoris with a high density region in it. The location of the high density region is indicated with a red circle. The clump starts at  $90^\circ$  azimuth and shifts towards  $0^\circ$  azimuth (in between the star and observer)

When plotting solely the locations of the photons on the detector surface, see Fig. 5.29, it is visible that just to the left of the cleared region, there is a region with a higher photon density. This effect is best visible when the observer is located at  $0^\circ$  azimuth, see Fig. 5.29a.

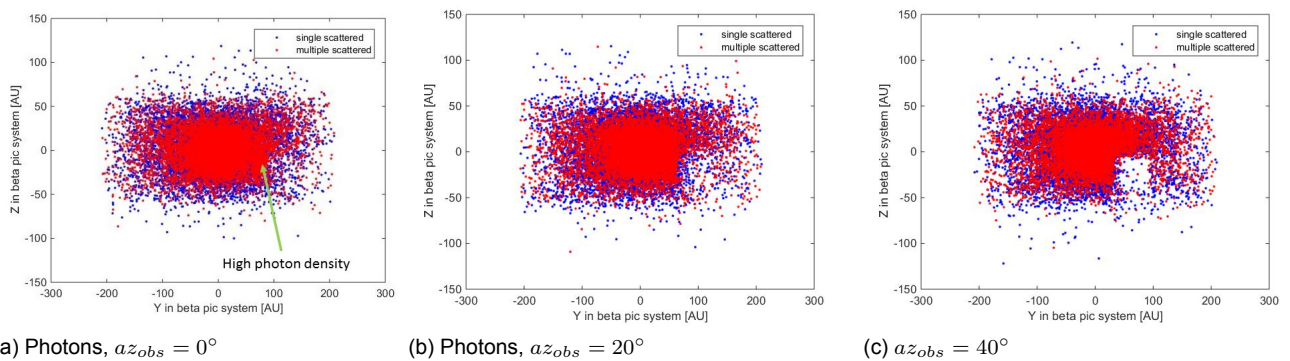


Figure 5.29: Locations of the photons that fall on the detector surface for a fan model describing the optical thickness, with a high density region centered at  $az = 90 + 18^\circ$ ,  $el = 0 - 9^\circ$ ,  $R = 100AU$ , coordinates are expressed in  $\beta$  Pic coordinates [AU]

The hypothesis that the high density region was optically too thick to transmit photons in a radial outward direction can be checked when the dust clump is seen from the other side, when the azimuth angle of the observer is negative. If the hypothesis is true then the dust clump should be visible from the back and the gap should be gone on the detector image. Both the photon locations themselves and

the detector images are shown, in Fig. 5.30 and Fig. 5.31. Indeed it can be seen that the cleared region has disappeared and the photon density is higher in the fourth quadrant of the detector surface. However in the polarization and intensity image the effect is barely visible.

A remarkable result is the increase of the maximum polarization degree of the detector plot, that has increased from 20% to 55%. Such high polarization degrees were not found for the images with positive azimuthal angles. It is not known why this difference exists.

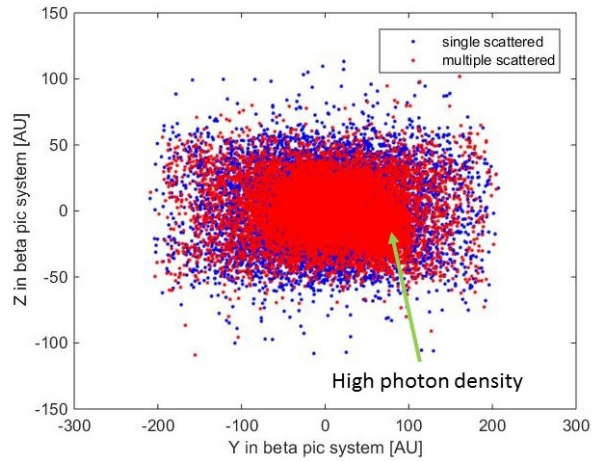


Figure 5.30: Photons,  $az_{obs} = -50^\circ$

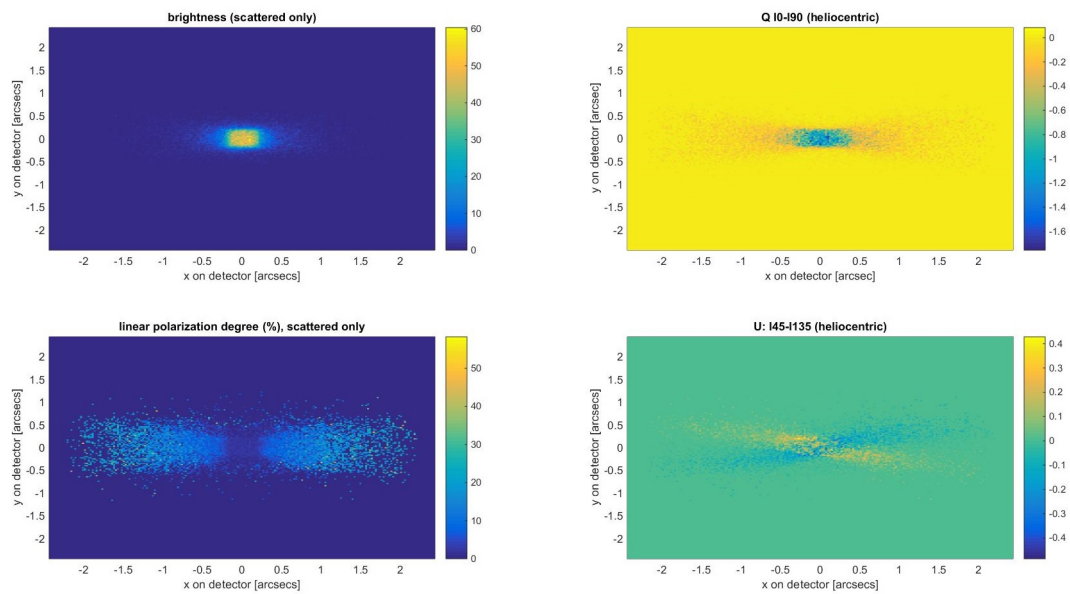


Figure 5.31: Simulated linear polarization degree of the dust disk surrounding planet  $\beta$  Pictoris with a high density region in it. The dust clump is seen in backscattered light and is located at  $130^\circ$  azimuth with respect to the observer.

It is possible that the clump is not visible in the brightness image as the albedo of the photons scattered by the clump is significantly lower than the albedo of the other photons. As the albedo was treated as a weight for the Stokes vector, and as this weight decreases with an increase in amount of scatterings, photons that are scattered often have a low weight. The photons scattered by the dust clump then would have a brightness that is too low to significantly impact the brightness images.

It was concluded earlier that multiple scattering in general increases the maximum polarization degree of the observed photons. This effect was visible at backscattering angles for the dust disk with the dense dust clump (200 times the local thickness), but it was not visible for the disk with the less dense dust clump (10 times the local thickness).

It is questionable if this analysis is enough to give a definite answer on the question whether a dust clump can be distinguished from the smoother cloud. The dust clump used for this analysis has the size of a full grid cell, which is large compared to the cloud. Also, the optical thickness was so high that it cleared the region located radially outward from the dust clump.

However there is one thing that is clear from this analysis: although the clump itself is visible considering the locations of the photon on the detector surface, the clump was less visible in the polarization and intensity images. This means that these types of 'clumps' or higher density regions do not have a significant higher polarization degree than its surroundings and hence it could be said they tend to disappear in the background of the smooth dust. This finding is important to answer the next question.

### **Can a dust clump be distinguished from its surroundings?**

It was shown that the behavior of the polarization signal of a planet differs significantly from the local polarization degree of the surrounding dust. The polarization degree of the planet was almost 2.5x higher than that of the dust. A different behavior might be expected when the orbital geometry is changed and in addition it must be noted that the maximum degree of polarization of another (real) planet can be lower than that for the used planet. However, the phase angle behavior will be still distinguishable from that of the dust.

The polarization signal of the dust clump was not clearly distinguished from the smooth surroundings. This was simulated with a dust clump having 10x the local thickness located at 10AU and a clump with 200x the local thickness located at 100AU. In both simulations a shadow effect was visible in forward scattered light, but for the dust clump at 100AU the effect was also visible at the mid-range of scattering angles. Looking at the clumps from the front (forward scattering regions) and from the back (backwards scattering regions) lead to the conclusion that the polarization degree at the location of the expected clump was not significantly altered with respect to the smooth surroundings. Hence in the simulated case the dust clumps have shown the same behavior as the smooth cloud.

As the observed linear polarization degree of the planet did not show the same behavior as the smooth cloud it thus can be concluded that a planet can be distinguished from a dust clump based on the observed polarization degree as a function of scattering angle. The shadow that is seen for the dust clump was not present for the planet, but of course this caused by the planet being included *after* the dust data was generated and hence such a shadow effect was not simulated.

Of course this analysis leaves room for improvement. Potentially there is an optimal optical thickness of the dust clump that on one hand causes enough additional scatterings for it to be detected, but at the other hand does not clear out the regions radially outward from the dust clump. If the number of grid cells is increased the results for a smaller dust clump can be computed, as it better represents a case in which scientists confuse a dust clump with a planet. To keep the computation time in bounds it is possible to simulate only a part of the cloud, but to do this ZPEC would need some slight adaptations.



# 6

## Conclusion and Recommendations

This chapter brings us to the very end of this thesis. The purpose of the thesis work was to develop a computational tool based on Monte-Carlo that can be used to analyze polarization properties of (exo)zodiacal dust. Four tasks were identified:

1. Develop the computational tool
2. Verify that the code works correctly
3. Use the tool to predict the background signal as sensed by LOUPE
4. Use the tool to analyze whether a dust clump can be distinguished from a planet

In this chapter first the conclusion with regards to the thesis objective and research tasks shall be given and then recommendations shall be given for further work on this subject.

### 6.1. Conclusion

As there was no research question to answer, the conclusion is best given by a summary of the work performed and the main findings of the research topics. Therefore the conclusion is structured accordingly.

#### The development of ZPEC

In response to the thesis goal a computational tool was developed that is called ZPEC: the Zodiacal dust Polarization Evaluation Code. The code follows the paths of each individual photon, which has as an advantage that multiple scattering can be simulated and that the full polarization state of the photon can be taken into account for the determination of the scattering direction. ZPEC uses a large computational package that creates a database of properties of dust particles that have been scattered inside a dust cloud. A detector view can be created for an observer that is located inside the dust cloud which is necessary to generate views similar to the LOUPE observations of the dust. External views of the dust can also be created, which corresponds with detector images of a distant observer. In addition planetary signals can be included in the detector views under the assumption that there is no interaction between the dust cloud and light scattered by the planet.

#### Verification of ZPEC

Verification of the code was performed using the Adding-Doubling method as a reference. For the verification dust particles were used that primarily scatter dust in forward directions. The propagation of the photons was simulated for an (almost) flat layer and it was found that the ZPEC results match the Adding-doubling code the best for apparent scattering angles  $< 60^\circ$ , for which a maximum deviation was found of 0.19%. It is thought that this deviation is primarily caused by averaging the datapoints over a bin. There were few photons that left the surface under angles  $> 60^\circ$  and hence the average

polarization degree of the photons shows larger deviations from the theoretical degree. The effect it has on the computed polarization averages can be seen as a result of the code being based on Monte-Carlo, and hence this effect is referred to as the Monte-Carlo (MC) noise. The differences found between the Adding-Doubling code and the ZPEC results for angles  $> 60^\circ$  were up to 0.55%, these differences are all within the expected MC noise level.

Using ZPEC two dust disks were evaluated: the relatively dense dust disk surrounding  $\beta$  Pictoris and the zodiacal dust disk found in the Solar System.

### Polarization signal of dust as sensed by LOUPE

Using the ZPEC *propagator* and *observer* the brightness and polarization signal of the dust could be compared with that of the Earth. However for this comparison no difference was made between the background signal and the foreground signal (hence it was not determined what part of the dust signal was found in between the Earth and the Moon). As the Moon orbits the Earth, the Earth is seen at different locations with respect to the zodiacal cloud and it is seen under different scattering angles. Taking into account these two factors it was found that the brightness of the dust compared to the Earth varies from  $4 \cdot 10^{-4}\%$  to 0.14%. When the polarization degree of the Earth is considered, the Earth is not always well distinguished from its surroundings. A simulation was performed for 120 days and it was found that for 17 of those days the light scattered by the Earth has (about) the same polarization degree as its dusty surroundings.

### The dust surrounding star $\beta$ Pictoris

The dust disk surrounding star  $\beta$  Pictoris was converted to an optical thickness model using a collisional model for dust and debris disks that was developed at NASA: the Supercomputer Method Algorithm for Collisions in Kuiper belts (SMACK). Using this optical thickness model and ZPEC two different analyses were performed.

The first analysis considers the importance of multiple scattering in the  $\beta$  Pic dust disk. In literature it is always found that it may be assumed that the disk is optically thin enough to assume photons are scattered only once. With ZPEC it was found that multiple scattering events in the dust disk actually cause the observed polarization degree to become higher than when only single scattering events are considered. Although the difference seems noisy due to the fact that ZPEC is based on MC, there is a clear trend visible for the center of the disk where the polarization degree is up to 1.5% higher (absolute) when multiple scattering is considered. A linear fit proved to fit the general trend in the best way, which predicts that multiple scattering should increase the local polarization degree of the cloud with up to 2% at the edges of the disk. As the density model of SMACK is not smooth the same analysis was performed using a smooth fan model (Millar-Blanchaer et al., 2015), in order to exclude any radial polarization features to be excluded from the estimated trend. It confirms that the linear polarization degree is higher when multiple scattering is included, but the estimated difference is lower. Data fitting shows that the effect is up to 0.8% towards the edges of the disk. The  $1\sigma$  uncertainty in this number is 0.07%.

The second analysis performed considers the influence of taking the polarization state of the photon into account to determine the scattering direction of the photon. Using a flat layer of scatterers and an optical thickness of  $\tau = 5AU^{-1}$  it was determined that if this would influence the observations, the effect is likely visible in the region with scattering angles of  $35 - 60^\circ$ . It was estimated that taking the polarization state into account increases the polarization in this region with a maximum of 0.5%. For  $\beta$  Pictoris the effect in this region was estimated to be between 0.15%-1% based on simulations using the SMACK optical thickness model, which does not match the predicted results. The analysis is also performed using the smooth density model, that provides a somewhat smoother image of the dust disk. Using this model it is estimated that the difference between taking/not taking the polarization direction into account to determine the scattering direction is about 0.01%, the uncertainty in this number is of the same magnitude. It is therefore concluded that the effect is not significant enough for ZPEC to detect it.

### **Distinguishing a dust clump from a planet**

The last analysis considers planets and dust clumps as it is of specific interest to determine if a dust clump can be distinguished from a planet. The last analysis was performed using the smooth fan model. First a planetary signal is compared with that of the background dust. It was found that along its orbit the planetary polarization signal has a larger amplitude than the polarization signal of the surrounding dust. Therefore, if the polarization degree of the planet is observed over time it should be clear to distinguish the planet from the dust.

A dust clump was included in the dust disk by artificially altering the local optical thickness in one of the ZPEC grid cells. The analysis was performed on two cases: one with a dust clump at 10AU with a thickness of 10 times the local density and another case with a dust clump at 100AU with a thickness of 100 times the local density. In both cases the dust clump cleared out the grid cells radially outward from the clump and hence leaving a shadow. The shadow was visible for both cases when the clump was seen directly from the front, but for the high density clump at 100AU this effect was more prominent and also visible at other observational/scattering angles. The observed polarization degree was virtually the same for the dust clump and the smooth surroundings, so for the simulated cases the dust clump linear polarization degree behaved the same as the smooth surroundings.

Therefore it was concluded, based on the simulated cases, that the polarization degree of a dust clump shows the same behavior as the dust disk and that it leaves a shadow when viewed in forward scattering directions. As the polarization behavior of the planet as a function of scattering angle is significantly different from the dust disk, a planet can be distinguished from a dust clump based on this difference in behavior.

## **6.2. Recommendations for future work**

A thesis is never perfect, as is the same for this thesis work. This research was mainly based on a Monte-Carlo analysis, which should show the statistical average of a large amount of data points. The question therefore rises: how many datapoints do I need to obtain a satisfying statistical average? What does satisfying actually mean? In the results section already a few recommendations were made that touch upon this topic, as it was found that a proper statistical average could not be constructed for all of the cases. This section shall summarize these recommendations again and shall provide the reader with further insight in any future topics of interest.

### **Extension of the existing datasets**

The most important improvement that has to be made for the work on the Solar System is to build databases that contain more photon properties. A more smooth inner view of the Solar System can be created which is in interest of LOUPE. It can be used to better determine the brightness of the dust with respect to the Earth and to create a better view of how LOUPE will observe the polarization degree of the Earth with respect to the dust. Furthermore it will complete the skyplot, which then can be used to verify the phase function that is used. In addition the influence of including/excluding the Earth trailing high density blob can be better analyzed.

### **Research to the optical properties of the dust and the cloud**

The phase functions that were used for this thesis were based on an approximation of fosterite particles. The use of these phase functions was recommended by O. Muñoz, but in the ZPEC skyplots of the dust as observed from the Earth, it could be seen that the region in which the maximum polarization degree is predicted is too close to the Sun. It is thought that this could have its origin in the phase function and therefore there is room left for improvement.

Although the SMACK density model nicely shows the structure of the dust disk, it was shown in the resulting images that the SMACK derived optical model shows irregularities. The optical thickness model can be improved if it is known how the created dust evolves over time. In the e-mail conversation with E. Nesvold it was mentioned such files do exist for the  $\beta$  Pic disk. Using these could improve the smoothness of the images and it is expected that the results match the Hubble view of the dust disk better.

To determine the influence of taking the polarization direction into account for the determination of the scattering direction it is recommended to use a smooth fan model for the  $\beta$  Pictoris disk. It was mentioned before that the irregularities in the SMACK derived model probably cause deviations in the data points that make any trends invisible. New databases can be build for cases with and without the polarization direction taken into account.

It was shown in this report that with the current size of the database it is useless to analyze the spectropolarimetric view of LOUPE. As the difference in optical thickness of the cloud at different frequencies is so small the effect is not noticeable. However the optical thickness of the cloud at different frequencies was based on one study only, in which the absorption cross-section was found for  $\beta$  Pic like particles. It is however questionable how well this represents the real behavior of the dust particles in the Solar System. Therefore the optical thickness of the cloud in the visual domain remains a topic of study. Especially in the case of LOUPE this optical thickness model is very important. LOUPE is a spectropolarimeter and it will enable the analysis of the Earth polarization signal at different frequencies. Therefore the optical thickness model of the dust is of importance as it is currently unknown if the dust shows any specific spectropolarimetric features that could impact the measurements.

### **Splitting the dust signal in a foreground and background model**

As was mentioned, the current analysis of the brightness of the dust and the polarization signal considers that all the dust signal is located at either the background or the foreground. To determine the maximum brightness contribution of the dust with respect to the Earth it was assumed all of the dust is located in between the Earth and the Moon. To determine if the Earth can be distinguished from its dusty surroundings it was assumed that all of the signals are found at the background. Although this provides the reader with information on the worst case scenario, it does not provide information on the actual noise level.

Such an improvement in the code is not made easily. It requires that the area between the Earth and the Moon is divided in smaller grid cells in such a way that it can be determined what photons have been scattered in between the Earth and the Moon. To provide a full simulation of the dust disk with grid cells of that size is probably impossible and the computational power is potentially too large. Therefore a clever configuration has to be made that uses a coarse grid cell configuration and a precise one. for which one could use the data of photons travelling towards the grid cell in which the moon and Earth are located as an input for the detailed simulation.

### **LOUPE as a means to study the dust cloud**

Current knowledge of the zodiacal cloud is based primarily on the data collected by the IRAS and the COBE/DIRBE satellite/instrument, which both studied the dust in the infrared region. As LOUPE encircles the Earth, it always has a part of the zodiacal cloud at the background and therefore LOUPE would be a perfect instrument to study the structure of the cloud in the visual domain. If more detailed images can be created with ZPEC, it would be possible to study the structure of the Earth circumsolar ring and the other cloud components. This can then be used in order to verify the work of Dermott et al., (1994) that predict the structure of the ring based on a numerical simulation. Also it was mentioned in literature that it is possible that the properties of the zodiacal cloud vary over heliocentric distances and that it is possible that the zodiacal cloud has a bimodal population. By further modelling of the cloud the influence of the bimodal population and heliocentric distance dependent properties can be determined. This can be used to see whether these effects are visible by LOUPE. It is then also possible to give a more definite answer to the question what kind of scattering angle dependent polarization behavior the dust particles show. This means that one could learn about the structure and the materials found for the dust particles.

In order to make these changes in ZPEC the properties of the photons need to be made dependent on the grid cell as now the dust properties vary throughout the dust disk. If these changes can be incorporated, the phase functions and optical properties can be defined per grid cell or per group. Of course it would mean an increase in required computational power, as now the ZPEC propagator has to retrieve these properties for every grid cell iteration. As the amount of grid cells has to go up to show a higher level of detail in the images this would drastically increase the computation time.

# Appendices





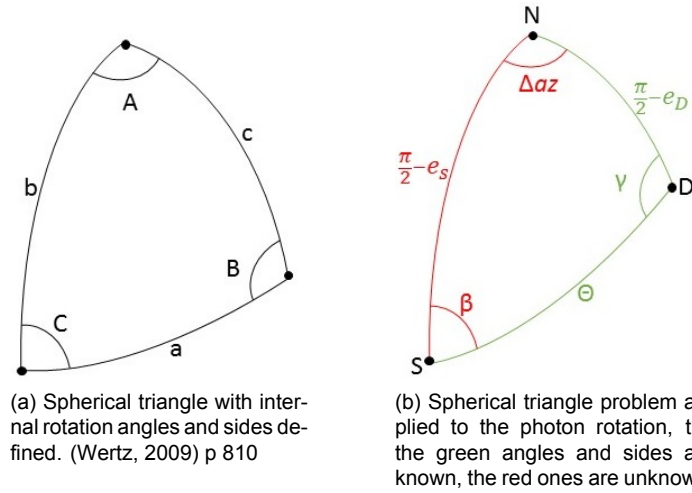


Figure A.2: Illustration of the Side-Angle-Side problem as applied to the scattering geometry of a photon particle

Applying these equations to the problem of the photon scattering leads to a spherical triangle as shown in Fig. A.2b. Hence the following set of equations apply and the transformation angle  $\beta$  can be determined;

$$\begin{aligned}
 \frac{\pi}{2} - e_s &= a \cos 2 \left[ \cos \theta \sin e_D + \sin \theta \cos e_D \cos \gamma, H(\gamma) \right] \\
 \Delta a &= a \cos 2 \left[ \frac{\cos \theta - \sin e_D \cos \gamma}{\cos e_D \sin \gamma}, H(\theta) \right] \\
 \beta &= a \cos 2 \left[ \frac{\sin e_D - \cos \theta \cos \gamma}{\sin \theta \sin \gamma}, H\left(\frac{\pi}{2} - e_D\right) \right]
 \end{aligned} \tag{A.4}$$

It can be seen that from these equations also the difference in azimuthal direction  $\Delta a$  can be found.

# B

## Moving the photon: governing equations

In this appendix the governing equations are given that are used to move the photons through the grid cell. In other words: to calculate the location of where they exit the grid cells based on their input location and information on the scattering event.

### B.1. Spherical to Cartesian coordinates

To convert spherical coordinates to cartesian coordinates the following set of equations is used;

$$\begin{aligned}x_0 &= R_0 \cos el_0 \cos az_0 \\y_0 &= R_0 \cos el_0 \sin az_0 \\x_0 &= R_0 \sin el_0\end{aligned}\tag{B.1}$$

### B.2. Cartesian to Spherical coordinates

To convert cartesian coordinates to spherical coordinates the following equations are used;

$$\begin{aligned}r &= \sqrt{x^2 + y^2 + z^2} \\r_{xy} &= \sqrt{x^2 + y^2} \\az &= \text{atan2}\left(\frac{y}{r_{xy}}, \frac{x}{r_{xy}}\right) \\el &= \text{asin}\left(\frac{z}{r}\right)\end{aligned}\tag{B.2}$$

### B.3. Single scattering - scattering location coordinates

For each of the photons in the grid cell a random number is generated which yields  $\Delta X < \Delta R$ . Now the photon grid cell exit coordinates  $[az_2, el_2, R_2]$  are calculated using the photon entry coordinates  $[az_0, el_0, R_0]$ , the direction of movement of the photon  $(a, e)$  and the number  $\Delta X$  and  $\Delta R$ . Then the coordinates of the scattering location  $[x_s, y_s, z_s]$  are calculated with Eq. B.3 using the direction of movement of the photon expressed in azimuthal angle  $a$  and elevational angle  $e$ ;

$$\begin{aligned}x_s &= x_0 + (x_1 - x_0) \frac{\Delta x}{\Delta R} = \Delta R \cos e \cos a \frac{\Delta X}{\Delta R} & \rightarrow x_s &= x_0 + \Delta X \cos e \cos a \\y_s &= y_0 + (y_1 - y_0) \frac{\Delta x}{\Delta R} = \Delta R \cos e \sin a \frac{\Delta X}{\Delta R} & \rightarrow y_s &= y_0 + \Delta X \cos e \sin a \\z_s &= z_0 + (z_1 - z_0) \frac{\Delta x}{\Delta R} = \Delta R \sin e \frac{\Delta X}{\Delta R} & \rightarrow z_s &= z_0 + \Delta X \sin e\end{aligned}\tag{B.3}$$

### B.4. Grid cell boundary- leaving planes

In order to keep track of the direction of propagation of the photons, one column in the photon property matrix is dedicated to the planes through which the photons leave their grid cell. The numbers that are

found in these matrix are based on the boundary conditions of the grid cell, which can be explained in the following way. In order to determine where the photon leaves a grid cell, the photon path is propagated such that it is certain the photon has left the grid cell. This path is discretized in a certain amount of steps and for all the location points the coordinates are stored in spherical coordinates. Hence, these points are described by three vectors: one with azimuth locations, one with elevational locations and one with radial locations. The location where one of the grid cell boundaries is exceeded the first determines the leaving plane of the photon. For example if for the three vectors that describe the propagated photon path it is found that the azimuth angle exceeds the grid cell boundary of  $az + \Delta az$  the first, the photon leaves the grid cell via the left plane. This plane is stored as a number 4 in the photon property matrix. This number is used in the simulator in order to determine the amount of photons that travel to the surrounding grid cells and to determine at what sides the photons enter these grid cells. See Fig. B.1 for an overview of the possible boundary conditions and the corresponding numbers dedicated to the exit planes.

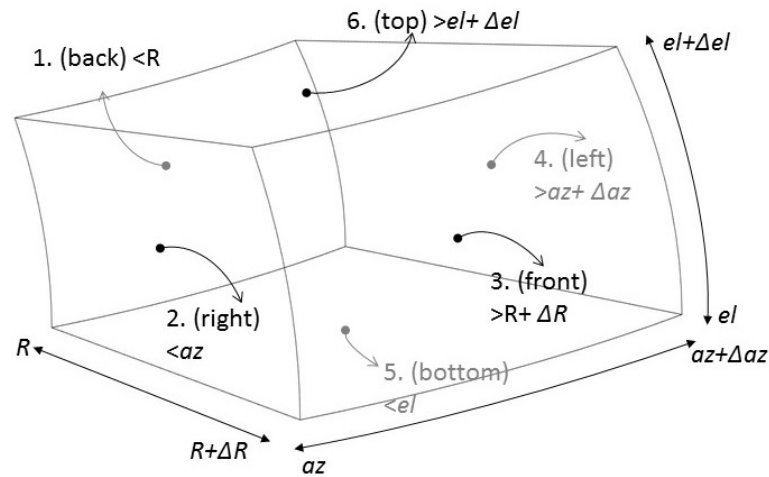
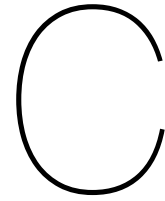


Figure B.1: Illustration of the procedure to calculate the coordinates of scattering for a disturbed photon



# Including planetary signals

## C.1. Figures

Figure C.1 illustrates that the Earth as seen from the moon travels along the night sky in comparison with the vector pointing to the Sun. It also shows the starting position of the simulated Earth position at the sky and that for the same apparent position of the moon with respect to the Earth, the Earth has shifted to the right.

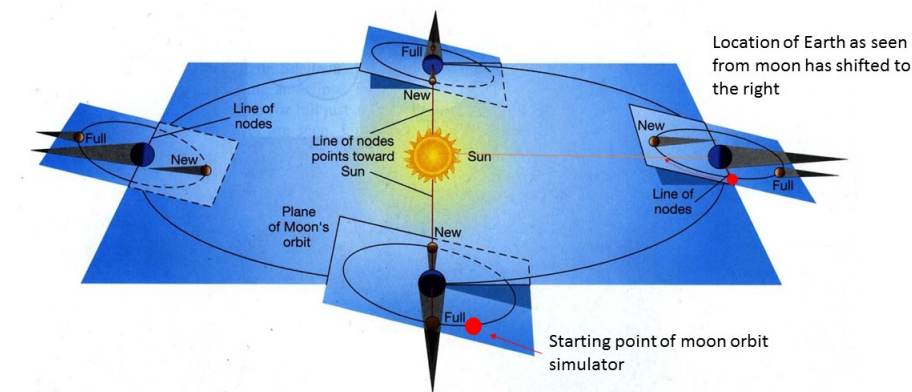


Figure C.1: geometry of the moon orbit. Original image retrieved from G. H. Rieke, University of Arizona <sup>1</sup>.

## C.2. Equations

The Kepler orbital equations are used to calculate the orbital radius over time;

$$r = \frac{a(1-e^2)}{1+e \cos \theta}; \quad n = \sqrt{\frac{\mu}{a^3}}; \quad \theta = n(t - t_p) \quad (C.1)$$

In these equations  $r$  is the orbital radius,  $a$  is the orbital semi-major axis,  $e$  is the orbital eccentricity,  $\theta$  is the true anomaly,  $n$  is the mean motion,  $\mu$  is the gravitational parameter of the celestial body that is orbited,  $t$  represents time and  $t_p$  the last time of pericenter passage.

<sup>1</sup><http://ircamera.as.arizona.edu/NatSci102/NatSci102/lectures/skyappearance.htm>

The following equations adopted from (Wertz, 2009) are used to calculate the cartesian coordinates along the orbit using the orbital elements;

$$\begin{aligned}
 l_1 &= \cos \Omega \cos \omega - \sin \Omega \sin \omega \cos i \\
 l_2 &= -\cos \Omega \sin \omega - \sin \Omega \cos \omega \cos i \\
 m_1 &= \sin \Omega \cos \omega + \cos \Omega \sin \omega \cos i \\
 m_2 &= -\sin \Omega \sin \omega + \cos \Omega \cos \omega \cos i \\
 n_1 &= \sin \omega \sin i \\
 n_2 &= \cos \omega \sin i
 \end{aligned} \tag{C.2}$$

In these equations  $\Omega$  is the right ascension of ascending node and  $\omega$  is the argument of periapsis.

$$\begin{bmatrix} \epsilon \\ \eta \end{bmatrix} = \begin{bmatrix} r \cos \theta \\ r \sin \theta \end{bmatrix}; \quad \begin{bmatrix} x \\ y \\ z \end{bmatrix} = \begin{bmatrix} l_1 & l_2 \\ m_1 & m_2 \\ n_1 & n_2 \end{bmatrix} \begin{bmatrix} \epsilon \\ \eta \end{bmatrix} \tag{C.3}$$

These calculations are performed for the Earth-Sun system, which yield the coordinates of the Earth (subscript) with respect to the Sun (superscript). The calculations are also performed for the Moon-Earth system that yield the coordinates of the Moon (subscript) with respect to the Earth. Both coordinates are given as a function of time and can be converted to spherical coordinates;

$$\begin{aligned}
 \begin{bmatrix} x(t) \\ y(t) \\ z(t) \end{bmatrix}_M^E &\Rightarrow \begin{bmatrix} az(t) \\ el(t) \\ R(t) \end{bmatrix}_M^E \\
 \begin{bmatrix} x(t) \\ y(t) \\ z(t) \end{bmatrix}_E^S &\Rightarrow \begin{bmatrix} az(t) \\ el(t) \\ E(t) \end{bmatrix}_E^S
 \end{aligned} \tag{C.4}$$

The azimuth and elevation of the Earth as seen from the Moon can be calculated as follows, where the point  $(0^\circ, 0^\circ)$  corresponds with the direction to the Sun.

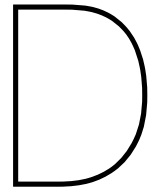
$$AZ(t) = -az|_M^E(t) + az|_E^S(t) \quad EL(t) = -el|_M^E(t); \tag{C.5}$$

### C.3. Orbital properties

The properties of the Earth orbit around the Sun and the Moon orbit around the Earth can be found in Table. C.1.

Table C.1: Orbital parameters for Moon-Earth and Earth-Sun systems, taken from (Lissauer & Pater 2013), p8 (if other it is indicated)

Symbol	Units		Moon	Earth
a	km	semimajor axis	384 400	149 597 995
e	-	eccentricity	0.0549	1.0167
$\mu$	$km^3/s^2$	gravitational parameter	3.986e5	1.327e11
$t_p$	s	pericenter passage	0(assumed)	0 (assumed)
$\Omega$	rad	right ascension of ascending node	0 (assumed)	0
$\omega$	deg	argument of periapsis	10 (assumed)	336.60
i	deg	inclination	18	0



## Loupe views of Earth and background dust

LOUPE views of the Earth and the background zodiacal dust have been simulated for a simulation time of three months. The results for the first simulation month can be found in Section 5.1.4, the views for the remainder of the simulation period can be found on the next pages.

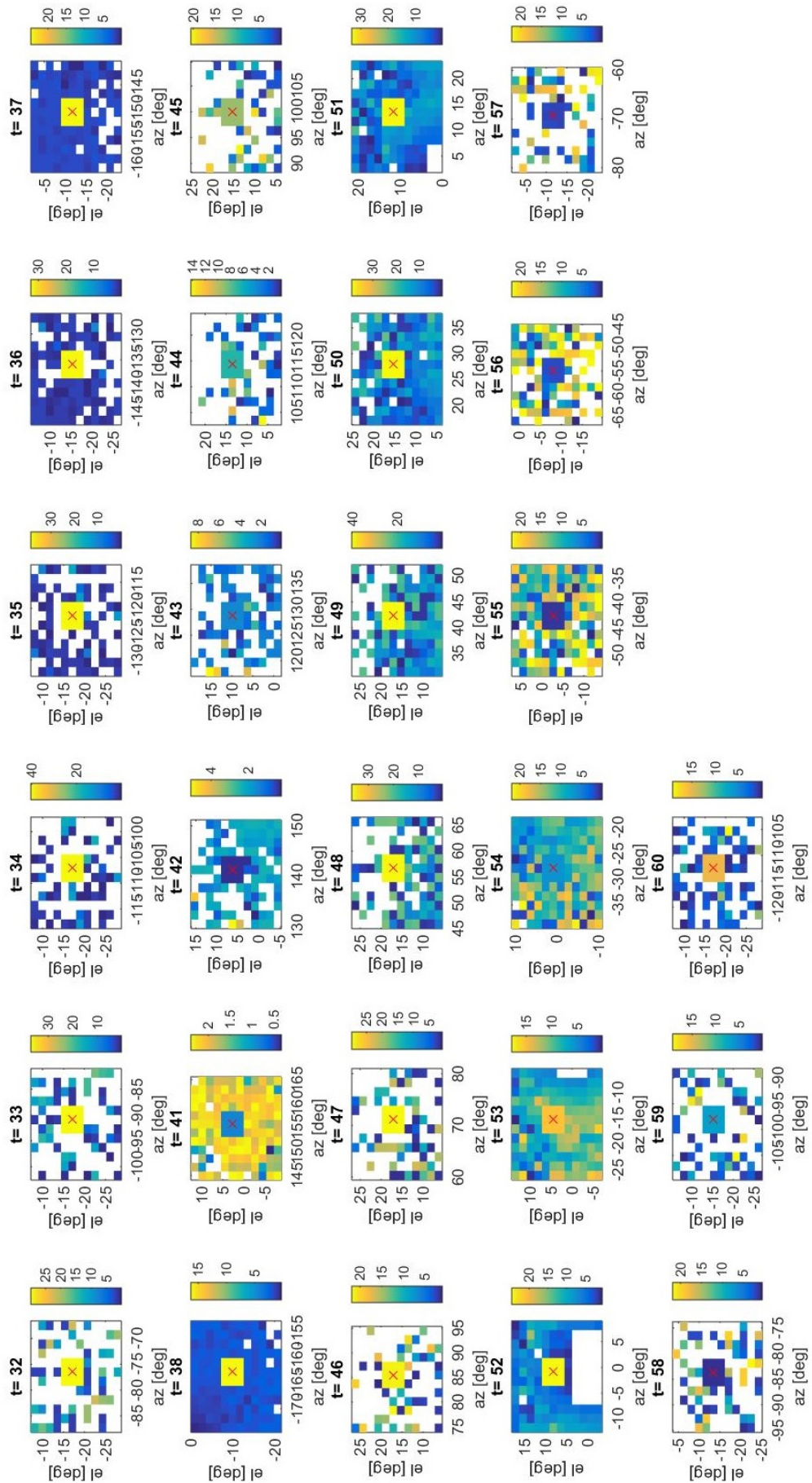


Figure D.1: Linear polarization degree [%] of the LOUPE view of the Earth with the zodiacal cloud at 800nm shown at the background, simulation time from  $t=32$  to  $t=60$  days. The center of the Earth is indicated with a red cross. The extended datasets were used to generate these views.

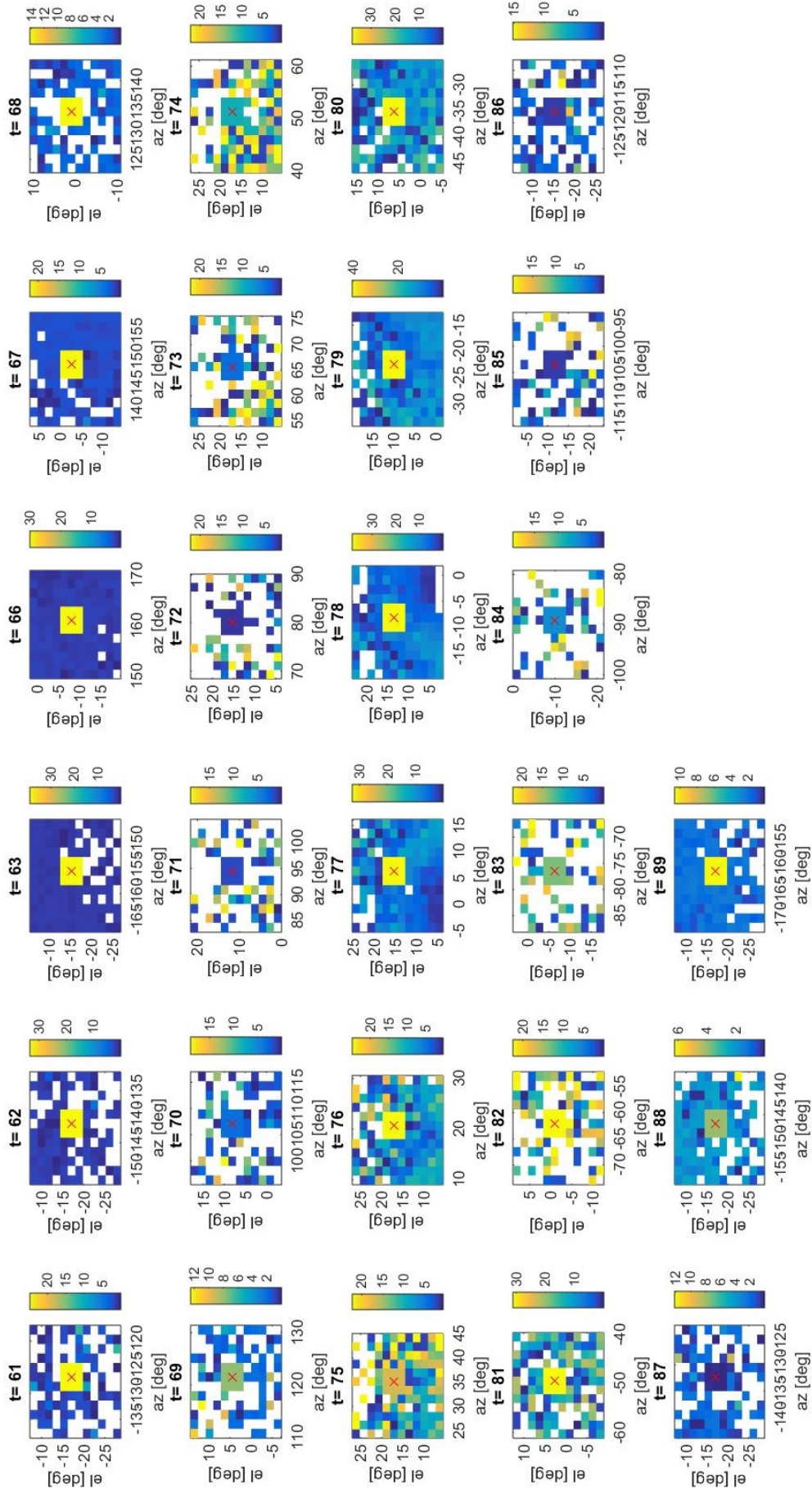


Figure D.2: Linear polarization degree [%] of the LOUPE view of the Earth with the zodiacal cloud at 800nm shown at the background, simulation time from  $t=61$  to  $t=89$  days. The center of the Earth is indicated with a red cross. The extended datasets were used to generate these views.

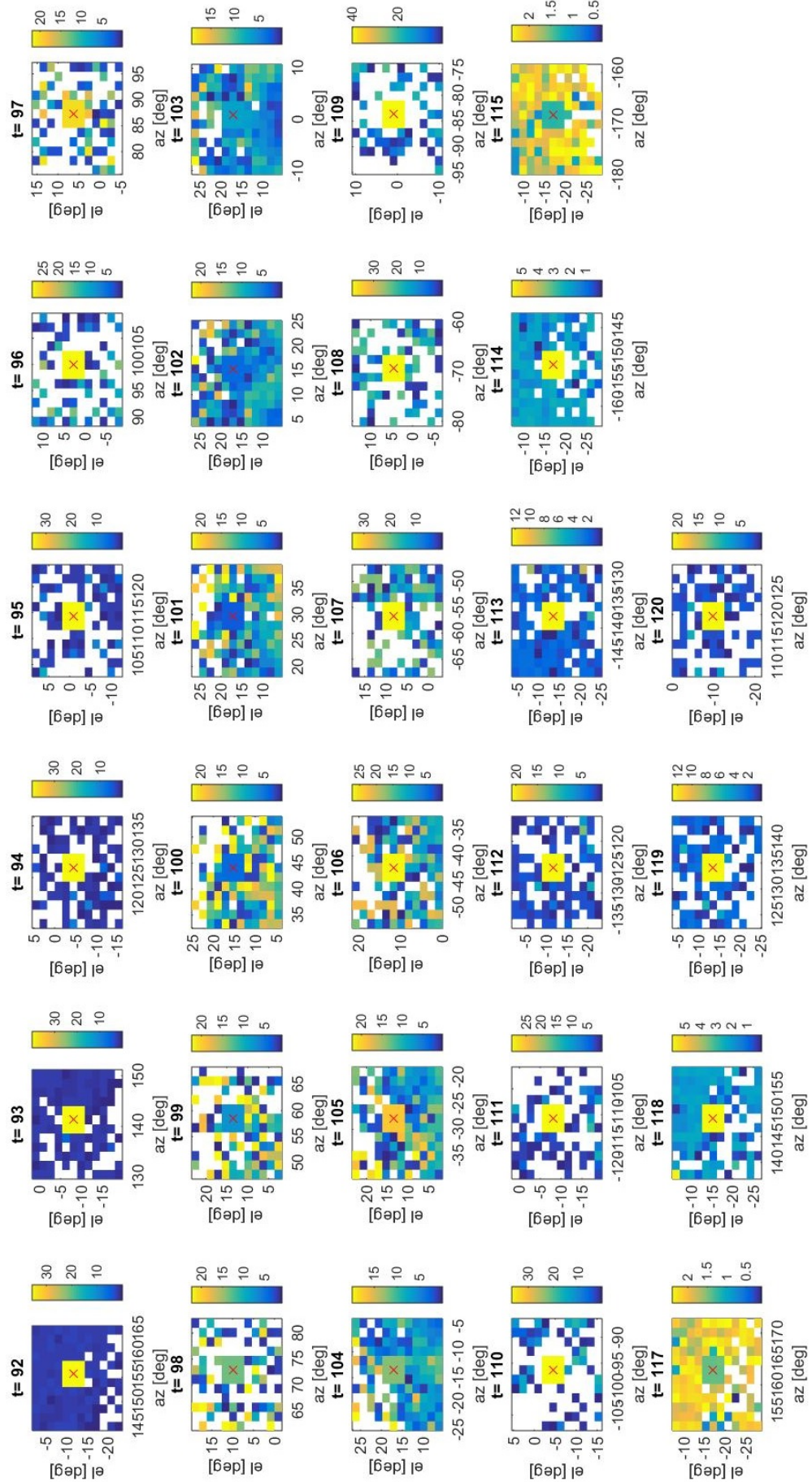


Figure D.3: Linear polarization degree [%] of the LOUPE view of the Earth with the zodiacal cloud at 800nm shown at the background, simulation time from  $t=92$  to  $t=120$  days. The center of the Earth is indicated with a red cross. The extended datasets were used to generate these views.

# References

- Ahmic, M., Croll, B., Artymowicz, P. (2009). *Dust distribution in the  $\beta$  Pictoris circumstellar disks*. *Astrophysical Journal*, 705: 529-542.
- Artymowicz, P. (1997). *Beta Pictoris: an early solar system?* *Annual Reviews of Earth Planetary Science*, 25: 175-219.
- Backman, D. E., Gillett, F. C., Witteborn, F. C. (1992). *Infrared observations and thermal models of the  $\beta$  Pictoris dust disk*. *Astrophysical Journal*, 385: 670-679.
- Delsemme, A. H. (1976). *Lecture notes in Physics* 48. Pp 314-318 and 481-484.
- Dermott, S.F., Jayaraman, S., Gustafson B.A.S., Liou, J.C. (1994). *A circumsolar ring of asteroidal dust in resonant lock with the Earth*. *Nature*, 369: 719-723.
- Dermott, S. F., Nicholson, P.D., Burns, J. A., Houck, J.R. (1984). *Origin of the solar system dust bands discovered by IRAS*. *Nature*, 312: 505, 509)
- Dominik, C., Tielens, A.G.G.M., (1997) *The physics of dust coagulation and the structure of dust aggregates in space*, *Astrophysical Journal* 480: 647-673
- Dumont, R., Sanchez, F. (1975). *Zodiacal light polarimetry. I. Observations, reductions, disturbing phenomena, accuracy*, *Astronomy & Astrophysics*, 38: 397-403.
- Fixsen, D.J., Dwek, E. (2002). *The zodiacal emission spectrum as determined by COBE and its implications*. *The Astrophysical Journal*, 578: 1009-1014.
- Giese, R.H., Kneissel, B.(1989). *Three-dimensional models of the zodiacal dust cloud. II: compatibility of proposed infrared models*. *Icarus*, 81: 369-378.
- Giese, R.H., Kneissel, B., Rittich, U. (1986). *Three-dimensional Models of the Zodiacal Dust Cloud: A comparative study*. *Icarus*, 68: 395-411.
- Greenberg, J.M. (1982). *What are comets made of? A model based on interstellar dust*. In: Wilkening, L.L. (Ed.), *Comets*. University of Arizona Press, pp. 131–163.
- Haan, de, J. F., Bosma, P. B., Hovenier, J.W. (1987). *The adding method for multiple scattering calculations of polarized light*. *Astronomy & Astrophysics*, 183: 371-391.
- Hahn, J. M., Zook, H.A., Cooper, B., Sunkara, B. (2002). *Clementine Observations of the Zodiacal Light and the Dust Content of the Inner Solar System*. *Icarus*, 158: 360-378.
- Hansen, J.E., Hovenier, J.W. (1974). *Interpretation of the polarization of Venus*. *Journal of Atmospheric Sciences*, 31: 1137-1160.
- Henyey, L.G., Greenstein, J. L (1941). *Diffuse radiation in the Galaxy*. *Astrophysical Journal*, 93: 70-83.
- Hovenier, J. W., Mee, van der, C.V.M. (1983). *Fundamental relationships relevant to the transfer of polarized light in a scattering atmosphere*. *Astronomy & Astrophysics*, 128: 1-16.
- Hovenier, J. W. Muñoz, O. (2009). *Light scattering in the solar system: an introductory review*, *Journal of Quantitative spectroscopy & Radiative Transfer*, 110: 1280-1292.
- Jackson, A. A., Zook, H. A. (1989). *A Solar System dust ring with the Earth as its shepherd*. *Nature*, 337: 629-631
- Jessberger, E.K., Stephan, T., Rost, D., Arndt, P., Maetz, M., Stadermann, F.J., Brownlee, D.E., Bradley, .P., Kurat, G. (2001). *Properties of interplanetary dust: information from collected samples*. In: Grün, E., Gustafson, B., Dermott, S., Fechtig, H. (Eds.), *Interplanetary Dust*. Springer, Berlin, pp. 253–294.

- Karaldi, T. Stam, D.M., Hovenier, J.W. (2012). *Looking for the rainbow on exoplanets covered by liquid and icy water clouds*. *Astronomy & Astrophysics*, 548: A90
- Karaldi, T., Stam, D.M., Snik, F., Bugnulo, S., Sparks, W.B., Keller, C.U. (2012). *Observing the Earth as an exoplanet with LOUPE, the Lunar Observatory for Unresolved Polarimetry of Earth*. *Planetary and Space Science*, 74(1): 202-207.
- Katyal, N., Banerjee, V., Puri, S. (2014). *Fractal signatures in analogs of interplanetary dust particles*. *Journal of Quantitative Spectroscopy & radiative transfer*, 146: 290-294.
- Keller, L. P., Messenger, S., Bradley, J. P. (2000). *Analysis of a deuterium-rich interplanetary dust particle (IDP) and implications for presolar material in IDPs*. *Journal of Geophysical Research*, 105: 397-402.
- Keller, C. U., Schmid, H. M., Venema, L. B., Hanenburg, H., Jager, R., Kasper, M., Martinez, P., Rigal, F., Rodenhuis, M., Roelfsema, R., Snik, F., Verinaud, C., Yaitskova, N. (2010) *EPOL: the exoplanet polarimeter for EPICS at the E-ELT*. In: Society of Photo-Optical Instrumentation Engineers (SPIE) Conference Series 7735
- Kelsall, T., Weiland, J.L., Franz, B.A., Reach, W.T. Arendt, R.G., Dwek, E., Freudenreich, H.T., Hauser, M.G., Moseley, S. H., Odegard, N.P., Silverberg, R.F., Wright, E.L. (1998). *The COBE Diffuse Infrared background experiment search for the cosmic infrared background. II: Model of the interplanetary dust cloud*. *Astrophysical Journal*, 508: 44-73.
- Kolokova, L., Jockers, K., Gustafson, B. A.S., Lichtenberg, G. (2001), *Color and polarization as indicators of comet properties and evolution in the near-nucleus coma*. *Geophysical Journal*, 106: 10113-10127.
- Kolokova, L., Hough, J., Levasseur-Regourd, A.C. (2015). *Polarimetry of Stars and planetary Systems*. Cambridge University press, Cambridge, first edition
- Kresák, L. (1980). *Sources of interplanetary dust*. Solid particles in the Solar System (Proceedings of the Symposium, Ottawa, August 27-30, 1979). pp 211-222
- Leinert, C., Bowyer, S., Haikala, L. K., Hanner, M. S., Hauser, M. G., Levasseur-Regourd, A.-C., Mann, I., Mattila, K., Reach, W. T., Schlosser, W., Staude, H. J., Toller, G. N., Weiland, J. L., Weinberg, J. L., Witt, A. N. (1998). *The 1997 reference of diffuse night sky brightness*, *Astronomy & Astrophysics Supplement*, 127: 1-99.
- Leinert, C., Hanner, M., Richter, I., Pitz, E. (1980). *The plane of symmetry of interplanetary dust in the inner solar system*. *Astronomy & Astrophysics*, 82: 328-336.
- Levasseur-Regourd, A. C. (1998). *Zodiacal Light, certitudes and questions*. *Earth Planets Space*, 50: 607-610
- Levasseur-Regourd, A. C., Cabane, M., Worms, J. C., Haudebourg, V. (1997). *Physical properties of dust in the solar system: relevance of a computational approach and of measurements under micro-gravity conditions*. *Advanced Space Research*, 20: 1585-1594.
- Levasseur-Regourd, A. C., Hadamcik, E. (2003). *Light scattering by irregular dust particles in the Solar System: observations and interpretation by laboratory measurements*. *Journal of Quantitative Spectroscopy & Radiative Transfer* 79-80: 903-910,
- Levasseur-Regourd, A. C., Mukai, T., Lasue, J., Okada, Y. (2007). *Physical properties of cometary and interplanetary dust*. *Planetary and Space sciences*, 55: 1010-1020.
- Lissauer, J.J., Pater de, I. (2013). *Fundamental Planetary Science: physics, chemistry and habitability*. Cambridge University Press, New York. First version.
- Lumme, K., Bowell, E. (1985). *Photometric properties of zodiacal light particles*. *Icarus*, 62: 54-71
- Millan-Gabet, R., Serabyn, E., Mennesson, B., Traub, W.A., Barry, R. K. Danchi, W.C., Kuchner, M., Ragland, S., Hrynevych, M., Woillez, J., Stapelfeldt, K., Bryden, G., Colavita, M.M., Booth, A.J., (2011), *Exo-zodiacal dust levels for nearby main-sequence stars: a survey with the keck interferometer nuller*. *Astrophysical Journal*, 734: 67-83.

- Millar-Blanchaer, M.A., et al., (2015).  *$\beta$  Pictoris' inner disk in polarized light and new orbital parameters for  $\beta$  pictoris b*. Submitted to Astrophysical Journal (juli 1)
- Moreno, F., Vilaplana, R., Muñoz, O., Molina, A., Guirado, D. (2006). *The scattering matrix for size distributions of irregular particles: an application to an olivine sample*. Journal of Quantitative Spectroscopy & Radiative Transfer, 100: 277-287.
- Muñoz, O., Moreno, F., Guirado, D., Dabrowska, D.D., Volten, H., Hovenier, J.W. (2012). *The Amsterdam-Gramada Light Scattering Database*. Journal of Quantitative Spectroscopy & Radiative Transfer, 113: 565-574.
- Muñoz, O., Volten, H., Hovenier, J.W., Veihelmann, B., van der Zande, W. J. (2004). *Scattering matrices of volcanic ash particles of Mount St Helens, Redoubt and Mount Spurr Volcanoes*, Journal of Geophysical Research, 109: D16201.
- Nakamura, R. (1998). *Optical properties of dust aggregates in the disk of Beta Pictoris*, Earth Planets Space, 50: 587-593.
- Nesvold, E.R., Kuchner, M.J.(2015). *A SMACK model of colliding planetesimals in the  $\beta$  Pictoris debris disk*, Astrophysical Journal, 815: A90.
- Ramella-Roman, J. C., Prahl, S. A., Jacques, S. L. (2005). *Three Monte Carlo programs of polarized light transport into scattering media: part I*. Optics Express, 13(12): 420-4438
- Reach, W.T. (1992). *Zodiacal Emission III: Dust Near the asteroid belt*. Astrophysical Journal, 392: 289-299.
- Reach, W. T., Franz, B. A., Weiland, J. L. (1997). *The three-dimensional structure of the zodiacal dust bands*. Icarus, 127: 461-484.
- Roberge, A., Chen, Ch.H., Millan-Gabet, R., Weinberger, A.J., Hinz, Ph.M., Stapelfeldt, K.R., Absil, O., Kuchner, M. J. Bryden, G. (2012). *The exozodiacal dust problem for direct observations of exo-Earths*, Publications of the Astronomical Society of the Pacific, 124: 799-808.
- Rooij, de, W. A., Stap, van der, C.C.A.H., (1984). *Expansion of Mie scattering matrices in generalized spherical functions*, Astronomy & Astrophysics, 131: 237-284.
- Rosenbush, V., Kiselev, N., Avramchuck, V. (2006). *Similarity and diversity in photometric and polarimetric opposition effects of small Solar System bodies*. Journal of Quantitative Spectroscopy & Radiative Transfer, 100: 325-339.
- Seager, S., Whitney, B. A., Sasselov, D. D. (2000). *Photometric Light Curves and Polarization of Close-in Extrasolar Giant Planets*. Astrophysical Journal, 540: 504–520.
- Stam, D.M. (2008). *Spectropolarimetric signatures of Earth-like extrasolar planets*. Astronomy & Astrophys, 482: 989-1007.
- Stam, D.M., De Rooij, W.A., Cornet, G., Hovenier, J.W. (2006). *Integrating polarized light over a planetary disk applied to starlight reflected by extrasolar planets*. Astronomy & Astrophysics, 452: 663-672.
- Sykes, M. V., Greenberg, R., (1986). *The formation and origin of the IRAS zodiacal dust bands as a consequence of single collisions between asteroids*. Icarus, 65: 51-69.
- Telesco, C. M., Knacke, R. F. (1991). *Detection of silicates in the  $\beta$  Pictoris disk*. Astrophysical Journal Letters, 372: L29-31
- Weiland, J. L., Arendt, R. G., Berriman, G. B., Dwek, E. , Freudenreich, H. T., Hauser, M. G., Kelsall, T., Lisse, C. M. , Mitra, M., Moseley, S. H. , Odegard, N. P. , Silverberg, R. F., Sodroski, T. J., Spiesman, W. J., Stemwedel, S. W. (1994). *COBE diffuse infrared background experiment observations of the galactic buldge*. Astrophysical Journal, 435: L81-L84.
- Wertz, J.R. (2009). *Orbit & Constellation Design & Management Spacecraft Orbit and Attitude Systems*. Space Technology Library & Microcosm Press and Springer, New York.